This is to certify that the
dissertation entitled

INTERROGATING MOLECULAR SCALE ORGANIZATION IN PLANAR LIPID BILAYERS AND LIPOSOMES

presented by

MONIKA J DOMINSKA

has been accepted towards fulfillment
of the requirements for the

Ph.D. degree in Chemistry

Major Professor's Signature

7/27/09

Date

INTERROGATING MOLECULAR SCALE ORGANIZATION IN PLANAR LIPID BILAYERS AND LIPOSOMES

By

Monika J. Dominska

A DISSERTATION

Submitted to
Michigan State University
in partial fulfillment of the requirements
for the degree of

DOCTOR OF PHILOSOPHY

Chemistry

2009

ABSTRACT

INTERROGATING MOLECULAR SCALE ORGANIZATION IN PLANAR LIPID BILAYERS AND LIPOSOMES

By

Monika J. Domińska

Biomolecules such as membrane proteins and enzymes are attractive candidates for use in biosensing devices because of their high selectivity, but to maintain the biological activity of these biomolecules, the interface in which they reside must mimic their natural environment. The activities of biomolecules associated with biological membranes are best maintained in lipid bilayers. However, to make a sensing device, artificial lipid bilayers must be attached to a transducer surface. Because the organization of lipids and biomolecules in a biological membrane is a complex mosaic that is characterized by its fluidity, the biomimetic lipid bilayer structures on transducer surfaces must have fluid properties similar to those of biological membranes.

We have imbedded selected molecular probes into our biomimetic interfaces to study their properties as candidates for supported lipid membranes capable of maintaining the activity of biomolecules such as transmembrane proteins. This research focuses on the organization of biomimetic interfaces absent protein incorporation. Our model systems were monolayers and bilayers doped with a reporter molecules. We have used self-assembly, Langmuir-Blodgett (LB), and Langmuir-Schaefer (LS) methods to construct planar lipid membranes on hydrophilic substrates (gold and indium-doped tin oxide (ITO) for electrochemistry, silica for spectroscopy).

Pyrene tethered to the interface acted as our reporter molecule. This probe has shown to experience significant molecular freedom as the only constituent of the interface. The addition of aliphatic coadsorbates to the interface improves the organization of the molecules by making the interface more rigid. Capping the monolayer with top lipid leaflet helps the organization of the molecules in the bottom leaflet even further.

We attempted liposome fusion on gold surfaces where the liposomes were composed of mixed lipids including thio-lipids modified with polyethylene glycol (PEG) in the headgroup. The failure to produce surface-attached lipid bilayer structures led to the need to understand the solution phase lipid assemblies that were presented to the interface. The addition of the thio-PEG lipid to the lipid assembly produces changes in organization that are most pronounced in the lipid headgroup region whereas the acyl chain region is minimally affected. To probe the dynamics of the acyl chain region we have used a free chromophore (perylene).

ACKNOWLEDGEMENTS

I would like to express my gratitude for the help in completion of this dissertation to Professor Gary Blanchard. He has been a great advisor to me and he has offered me all the possibilities that every young researcher needs at the beginning of their career. He taught me a lot of things and he always had his confidence in me. I truly appreciate it. I have been very fortunate to join his group.

I would like to thank second advisor Professor Paweł Krysiński from University of Warsaw for introducing me to Professor Blanchard as well as for maintaining the collaboration with me. I am grateful to him for hosting me in Warsaw and allowing me to perform some of my experiments in his lab.

As every researcher at the beginning of their career I came across many challenges while working on my research project. Every time desperate looking for help I could always count on my Guidance Committee. I would like to thank them all: Professor Daniel Jones, Professor Greg Swain and Professor Merlin Bruening for always being approachable and helpful.

I owe special thanks to my parents Krystyna and Henryk Domiński for their encouragement, constant support, love and prayers. I want to dedicate this dissertation to them.

I am also very thankful to my great friends and family for all the confidence in me. I very much appreciate their help in my preparations for the seminars and all the great discussions that we always have.

TABLE OF CONTENTS

LIST OF TABLES

LIST OF FIGURES

CHAPTER 1

INTRODUCTION

The combination of biological recognition with physical transduction to produce a functional biosensing device holds great appeal because of the potential application of these devices in fields such as medical diagnostics, environmental monitoring, and drug or toxin detection. Depending on the design, the transducer surface can serve either to monitor the biological reaction or to activate the biomolecules to function in the desired manner. Biomolecules such as enzymes, antibodies, protein receptors, channels, pumps, and nucleic acids constitute a broad palette of biologically selective components that can be attached to a transducer surface.[1-4] In developing a biosensor, it is important to enable communication between the biologically selective component and the transducer surface. Several methods were developed to immobilize biomolecules on the transducer surface while maintaining their biological activity.[3-6] Very sophisticated methods of structurally aligning and orienting biomolecules on solid supports were investigated.[7-10] Because the native environment for the biomolecules in a living cell is the cytoplasm and an interfacial region of the cell membrane, changes caused by direct immobilization of these molecules onto a solid support may affect their function. For example, membrane proteins functioning as ion channels, pumps, and receptors lose their biological activity when removed from their natural plasma membrane environment. To better accommodate and maintain the biological activity of these molecules, the transducer interface has to be modified in some manner.

Lipid bilayers provide a suitable environment for membrane proteins. However, to maintain the protein native activity in the supported lipid bilayer, several requirements must be met. One of the requirements is that the lipid bilayer must be in a fluid state to allow diffusion of the incorporated proteins. Another is that both sides of the lipid membrane must be in contact with aqueous environments in order to accommodate hydrophilic portions of the inserted proteins. Numerous artificial lipid bilayer systems on solid supports have been designed in the last few decades and different bilayer deposition procedures have been developed depending on the solid substrate properties.[5,11-27] One of the ways to deposit a lipid bilayer on a planar substrate is to add one lipid leaflet after another. The first leaflet can be prepared using Langmuir-Blodgett (LB) or self-assembling techniques. To complete the lipid bilayer, the second lipid leaflet can be added by Langmuir-Schafer (LS) deposition, self-assembly from organic solvents, or vesicle fusion. Another elegant method to generate a complete lipid bilayer is liposome fusion on a hydrophilic solid substrate. The advantage of this method is that the lipid bilayers can be prepared easily in a fast one-step procedure. The disadvantage of using physical adsorption methods is poor stability and the possibility of forming defects in a created interface, which can affect the quantitative analytical information. Covalent attachment of the lipid bilayer to the solid support, with a controlled density of covalent attachment points, seems to be an attractive approach to membrane immobilization.

Electrochemical methods of analysis require the use of conductive substrates as transducers. Metals such as gold, mercury, and silver have been used as substrates for bilayer lipid membranes.[11-14,16,17] Gold has been shown to be useful in the development of well organized and stable self-assembled monolayers (SAMs).[28-30] A metal surface modified with an alkanethiol monolayer can serve as a platform for the construction of supported membranes. Supported lipid membranes on gold electrodes generally exhibit good stability which can be estimated by measurement of the membrane capacitance. Typical capacitance for a stable and isolating lipid membrane is on the order of 0.5-1 μF/cm^2.[11,13,15,16] Many techniques for constructing lipid bilayers on gold have been described.[11-13,15-19] Most methods take advantage of thiol-gold chemistry to self-assemble molecules on the gold surface. These monolayers are usually well organized and relatively defect free, making them suitable for electrochemical analysis. SAMs of alkanethiols or thiolipids have been commonly used as a hydrophobic base for the deposition of a second lipid leaflet. The second leaflet can be deposited using methods such as Langmuir-Schaefer, physisorption of lipids from organic solvents, or vesicle fusion. Such interfaces have been shown to be useful for the immobilization of protein receptors.[12] However, for transmembrane proteins such as ion channels or pumps, the interface lacks the lateral fluidity as well as a hydrophilic cushion between the bilayer and the supporting substrate, and these factors preclude protein incorporation.[13] To provide a hydrophilic spacer between the lipid bilayer and the gold surface, the latter can be functionalized with charged SAMs to allow the adsorption of a counter-charged lipid membrane.[15] One disadvantage of this method is the decoupling of the membrane from the SAM support when high ionic strength solutions are used as electrolytes. To maximize the hydrophilicity of the bilayer support, and simultaneously minimize the interaction of the support with the membrane, self-assembled hydrophilic polymers were employed.[21,22] The disadvantage of using physisorption on a polymer surface is that it typically leads to incomplete vesicle fusion and low surface coverage, precluding electrochemical examination of surface-attached proteins.[21] Better surface coverage has been achieved with SAMs of lipids modified at their headgroup with a thiol-terminated hydrophilic polymer.[11,17,23,24] SAMs formed from these modified lipids can serve as a platform for the deposition of a second lipid leaflet. The second lipid leaflet can then be attached to the modified surface by self-assembly from organic solvents, detergent dilution or vesicle fusion. The membrane capacitance for this type of interface has been reported to be on the order of 0.35-1 $\mu F/cm^2$.[11,17,23,24] Supported lipid bilayers constructed this way have been shown to successfully form fluid membranes with an aqueous region between a lipid membrane and a gold electrode, which allows transmembrane protein incorporation and proper function.[11,17,24]

To monitor biological events at an interface using fluorescence spectroscopy, the lipid bilayers have to be prepared on transparent substrates such as indium-doped tin oxide (ITO) or silica. Because of the hydrophilicity of the substrates, vesicle fusion can be used to deposit a planar lipid bilayer.[25-27,31] Another approach to constructing a lipid bilayer with a hydrophilic region between the bilayer and the surface is to transfer lipids modified with hydrophilic polymers in the headgroup and terminated with a silane group, using the LB method.[27] To complete the bilayer formation, the second lipid leaflet is then added using vesicle fusion. Cellulose modified ITO substrates onto which positively charged lipid vesicles were fused provided insulating lipid membranes.[32] The impedance analysis showed the capacitance of this kind of membranes was ca. 0.5 $\mu F/cm^2$.

In this project we used various methods to build interfaces on solid substrates and investigated the organization of these films at the molecular level. Our long term goal is to construct and examine the properties of supported lipid bilayers that are capable of accommodating transmembrane proteins and maintaining the protein biological activity. We have started with simple model systems to get a better understanding of the complexity of the supported bilayer lipid membrane as a whole. The work accomplished to date focused on the formation and characterization of mono- and bilayer films that are components of the supported lipid bilayer on transducer surfaces.[33-35]

Information about the bilayer structure and dynamics can be obtained by controlled "doping" of the bilayer with probe molecules. These reporter molecules are capable of interrogating the bilayer local organization. However, for information from these probes to be useful, they must be localized at predetermined locations within the interface and this can be accomplished by binding the reporter molecule to the transducer surface. Using reporter molecules tethered at various distances from the transducer surface, we have investigated the structure and dynamics of monomolecular films as well as the lipid bilayers. Localization of the probe at various points of the lipid bilayer provides direct information about the organization and dynamics of molecules at certain planes of the interface.

A molecular probe used in both spectroscopic and electrochemical studies of planar lipid bilayers was a family of pyrene derivatives. The electrochemical response of pyrene derivatives attached covalently to the solid substrates has been described in the literature (Figure 1.1).[33,35,36] In the first anodic scan pyrene is oxidized to form radical cation at potentials higher than 0.8 V vs. Ag | AgCl reference electrode. In the

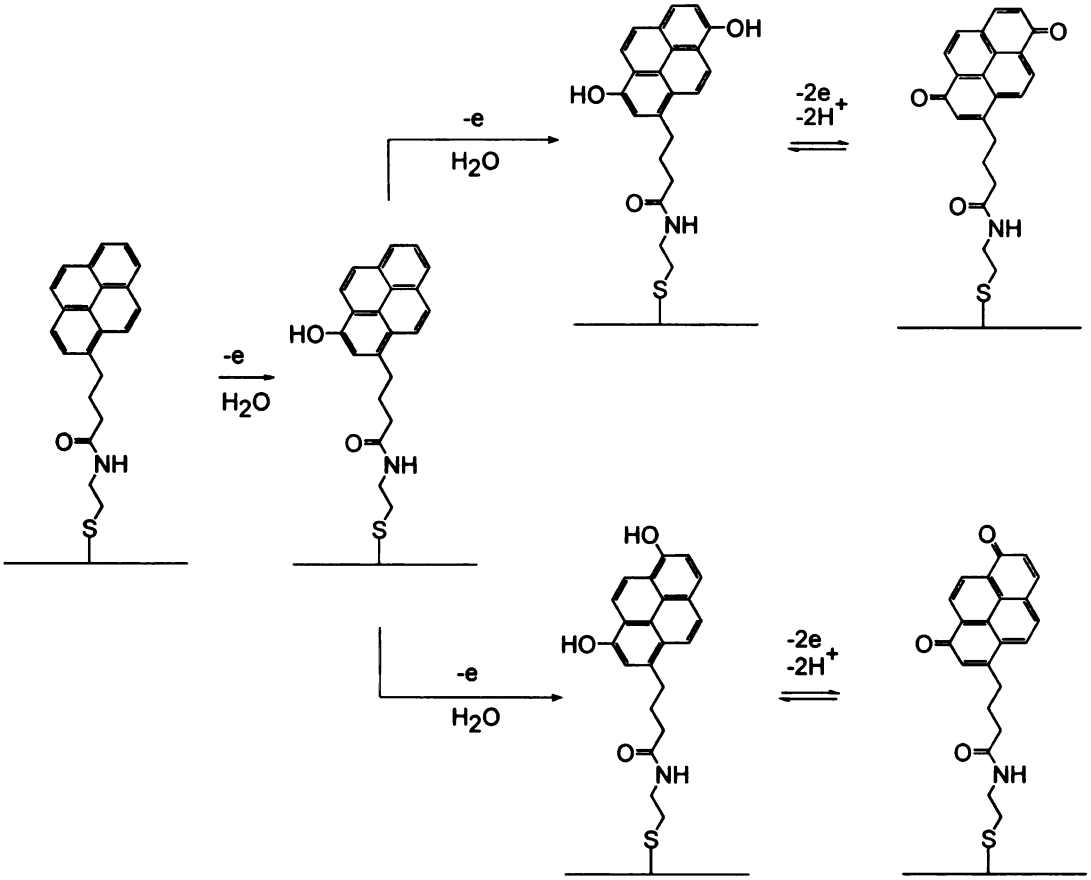

Figure 1.1 Schematic of the redox reactions characteristic of the pyrene moiety.

subsequent cathodic scan, the radical cation reacts rapidly with water to form a monohydroxypyrene. The monohydroxypyrene can also react with water to form one of several isomeric forms of dihydroxypyrene. Because the redox peaks associated with the formation of monohydroxypyrene (0.6 V vs. Ag | AgCl) disappear in subsequent scans,[36] the pyrenedione form must be the most stable product. The two dominant isomeric forms are 1,6- dihydroxypyrene/1,6-pyrenedione and 1,8-dihydroxypyrene/1,8-pyrenedione couples. The redox potential of the 1,8 isomeric form is shifted toward negative potentials by about 0.1 V relative to the 1,6 isomer.[36,37] In the cyclic voltammogram of pyrene derivatives covalently attached to the electrode surface the redox peaks from these two couples overlap to form one broad peak at ca. 0.2-0.3 V vs. Ag | AgCl.[33,35,36]

To interrogate the organization of the interfacial structures doped with tethered pyrene, we use electrochemical methods such as cyclic voltammetry and AC voltammetry. Cyclic voltammetry provides information regarding the surface coverage with redox active probes attached to the monolayer. Knowing the number of electrons involved in the redox reaction (n) and the electrode surface area (A), the amount of the redox-active probe tethered to the electrode surface (Γ) can be estimated from cyclic voltammograms based on the charge under the peak (Q):

$$\Gamma = \frac{Q}{nFA} \tag{1.1}$$

where F is the Faraday constant. In the absence of the Faradaic current, cyclic voltammograms also allow the estimation of the interfacial film thickness by measuring the charging current and relating it to the capacitance of the interface:

$$C = \frac{\varepsilon \varepsilon_0}{d} \tag{1.2}$$

where C is the specific capacitance, d is the distance between the capacitor plates, which is the measure of the insulating film thickness, ε is the dielectric constant, and ε_0 is the permittivity of free space.

We use AC voltammetry to study redox reaction kinetics. Changes in the peak current with the frequency of AC voltage provide information about the rate of the electron transfer between the immobilized redox species and the electrode surface. To estimate the electron transfer rate constant from AC voltammograms, we use a model developed by Creager and Wooster.[38] In this model the interfacial redox-active system on the electrode surface is represented by the impedance of a Randles equivalent circuit (Figure 1.2a) where C_{DL} is the double layer capacitance, C_{AD} is the adsorption pseudocapacitance, R_{CT} is the charge transfer resistance, and R_{SOL} is the solution resistance. The relationship between the circuit elements and the parameters characterizing the electrode coated with the redox-active monolayer when the average potential applied to the electrode is the peak potential is as follows:

$$\begin{aligned} C_{DL} &= \left(\frac{C}{A}\right)(A) \\ C_{AD} &= \left(F^2 A\Gamma\right)\Big/(4RT) \\ R_{CT} &= (2RT)\Big/\left(F^2 A\Gamma k_{et}\right) \end{aligned} \tag{1.3}$$

where C/A is the double layer capacitance per unit area, A is the electrode area, Γ is the

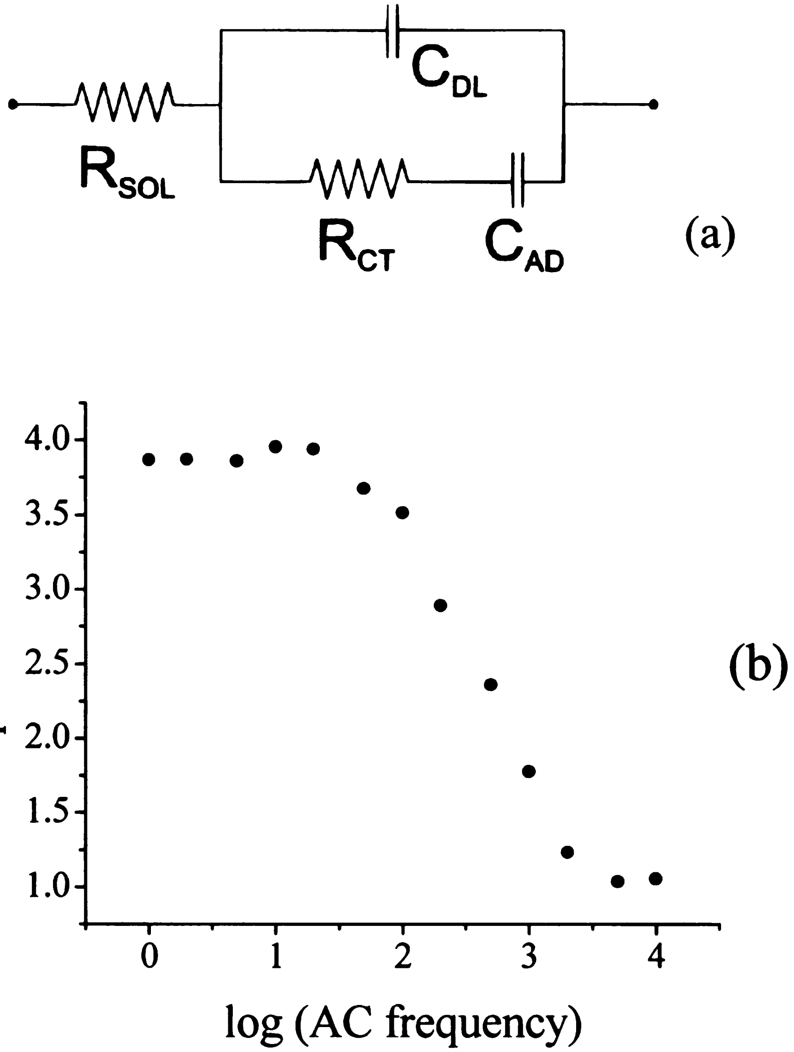

Figure 1.2 (a) Equivalent circuit used to model the AC impedance data. R_{SOL} = solution resistance, R_{CT} = charge transfer resistance, C_{AD} = adsorption pseudocapacitance and C_{DL} = double layer capacitance. (b) Plot of peak current/background current ratio vs. log (AC frequency)

electrode coverage with redox-active species per unit area. Based on these expressions the electron transfer rate constant is obtained by:

$$k_{et} = \frac{1}{2R_{CT}C_{AD}} \tag{1.4}$$

The analysis of the AC voltammetry data involves plotting the AC peak current (i_p) to background current (i_b) ratio versus the logarithm of AC frequency (f) for a series of voltammograms recorded over a broad AC frequency range:

$$\frac{i_p}{i_b} = 1 + \frac{1}{R_{CT}C_{DL}f + \frac{C_{DL}}{C_{AD}}} \tag{1.5}$$

These plots exhibit three distinct regions (Figure 1.2b). At low frequencies, the current ratio attains a plateau at the value that is indicative of the amount of the redox-active species on the electrode surface. There is very little kinetic information in this region because the AC frequency is slower than the relevant redox process. At high frequencies, the peak to background current ratio approaches unity because these AC frequencies are much faster than the reaction kinetics. At intermediate frequencies, the peak to background current ratio depends sensitively on the AC frequency and is related to the standard electron transfer rate constant for the electrode attached redox-active species.[38-40]

To interrogate the rotational diffusion dynamics of the chromophore in our model systems, we have used time-resolved fluorescence spectroscopy and measured fluorescence anisotropy decay. With this measurement, the randomly oriented chromophore molecules in the sample are excited with a short, vertically polarized pulse of light, producing a polarized emission transient from the sample. The molecules with their absorption transition dipole moments oriented parallel to the excitation light are excited preferentially, resulting in an oriented population of excited molecules. The emission from the sample is polarized according to the orientational distribution of the chromophore emission transition dipole moments, and this distribution reramdomizes as a function of time. The polarized emission transient is collected at polarizations parallel and perpendicular to the excitation pulse (Figure 1.3a). The polarized emission intensities ($I_{\|}$(t) and $I_{\perp}$(t)) are then combined (Equation 1.6) to yield the induced orientational anisotropy function, r(t) (Figure 1.3b):

$$r(t) = \frac{I_{\|}(t) - I_{\perp}(t)}{I_{\|}(t) + 2I_{\perp}(t)} \tag{1.6}$$

$$r(t) = r(0)\exp\left(-t/\tau_{OR}\right) \tag{1.7}$$

For chromophores in an unrestricted environment such as solution, the initial anisotropic orientational distribution, r(0), can relax to a random orientational distribution following excitation (Equation 1.7). As the molecules re-randomize, the anisotropy decays with time to zero, at which point the ensemble of excited molecules are again oriented randomly. The reorientation time constant (τ_{OR}) describes the motion of the chromophore in its local environment. According to the modified Debye-Stokes-Einstein equation, the reorientation time constant for spherical molecules is related to the rotational diffusion constant, D, and to the viscosity of the local environment:[41-43]

$$\tau_{OR} = \frac{1}{6D} = \frac{\eta V f}{k_B T S} \tag{1.8}$$

where η is the viscosity of the medium surrounding the chromophore, V is the hydrodynamic volume of the chromophore, f is the frictional term to account for solvent-solute interactions, k_B is the Boltzmann constant, T is the absolute temperature, and S is a factor related to the shape of the chromophore.[41-43]

Because the volume swept out by the probe molecule is typically nonspherical, it must be described in the context of an ellipsoidal shape, and the anisotropy decay functionality is related to the shape of the volume swept out by the rotating molecule.[44] Depending on the orientation of the absorption and emission transition dipole moments relative to the ellipsoidal axes, and the shape of the ellipsoidal rotor, it is possible for the anisotropy decay function, *r*(t), to exhibit more than one exponential decay. This situation requires a description of molecular motion that is more rigorous than the Debye-Stokes-Einstein treatment. Chuang and Eisenthal have provided the theoretical treatment for an ellipsoidal rotor, and their formulation accounts for the range of functional forms that can be observed in experimental *r*(t) data.[44] The ellipsoidal volume can be described as either prolate ellipsoid or oblate ellipsoid. Assuming the absorption and emission transition moments are parallel and lie in the chromophore π-plane, along the long molecular axis, a prolate ellipsoid is characterized by rotation primarily about the chromophore long in plane axis ($D_x > D_y = D_z$) (Equation 1.9)while oblate ellipsoid is characterized by rotation about the axis perpendicular to the chromophore π-system ($D_z >$

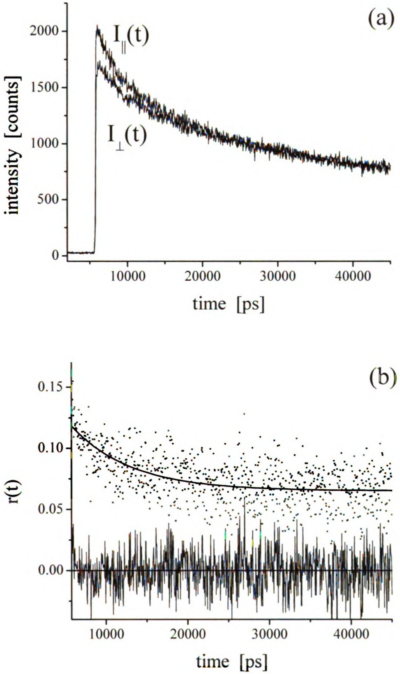

Figure 1.3 (a) Time-resolved emission intensities for polarization parallel ($I_{||}(t)$) and perpendicular ($I_{\perp}(t)$) to the excitation polarization (b) Orientational anisotropy function obtained from data shown in (a). The fit to the data is shown as a solid line and residuals are distributed around zero.

$D_x = D_y$) (Equation 1.10).

$$r(t) = 0.4\exp\left(-6D_z t\right) \tag{1.9}$$

$$r(t) = 0.3\exp\left(-\left(2D_x + 4D_z\right)t\right) + 0.1\exp\left(-6D_x t\right) \tag{1.10}$$

When the motion of the chromophore is restricted in some manner (*e.g.* confined by attachment to a lipid membrane), the photo-selected anisotropic distribution cannot orientationally re-randomize completely. For chromophores in a restricted environment, the anisotropy at times long after excitation does not decay to zero. The motion of the chromophore in a constrained environment can be expressed using a hindered rotor model developed by Lipari and Szabo.[45] In this model the orientational anisotropy decays with time as the chromophore orientational distribution re-randomizes to the extent possible:

$$r(t) = r(\infty) + \left(r(0) - r(\infty)\right)\exp\left(-t/\tau_{HR}\right) \tag{1.11}$$

where $r(0)$ and $r(\infty)$ are initial and infinite time anisotropies, respectively. The zero-time anisotropy depends on the angle between the excited and emitting transition dipole moments of the chromophore. The infinite time anisotropy is associated with the degree of motional restriction imposed on the chromophore by its immediate environment:

$$\sqrt{\frac{r(\infty)}{r(0)}} = 0.5 + \left(\cos\theta_0\left(1 + \cos\theta_0\right)\right) \tag{1.12}$$

The decay time constant τ_{HR} is related to semi-angle of the cone θ_0 within which the chromophore is constrained, and is related to the "wobbling" diffusion coefficient D_{W}, which describes the motion of the chromophore about its tethering bond

$$\tau_{HR} = \frac{7\theta_0^2}{24D_W} \tag{1.13}$$

The cone angle value provides information about the organization of the molecules in the studied system. Large cone values are consistent with large volumes being swept out by the chromophore and represent significant motional freedom of the molecule within the probed environment. Small cone values are indicative of a motion of the chromophore in a more constrained environment.

We have used various types of pyrene chromophores as tethered probes, with the specific choice of tethered pyrene derivative depending on the system under examination. The fluorescence and electrochemical behavior of this probe is well established and understood. In Chapters 2 and 3 we investigated both electrochemical and spectroscopic behavior, respectively, of covalently bound pyrene on solid substrates to probe the interfacial organization of the molecules in monomolecular films. Pyrene in form of fatty acid analogues was then used to probe the environment of Langmuir-Blodgett bilayers and these experiments are presented in Chapter 4. The experiments directed toward construction of a supported lipid bilayer system with a hydrophilic cushion between the bilayer and the solid support, led us to study the macroscopic structure of the liposomes and micelles. Attempting the fusion of vesicles modified with polyethylene glycol on solid substrates, we observed polymer concentration dependent changes in the liposome structure. In Chapter 5 we examine the organization of the molecules in these liposomes using pyrene tethered to phospholipid acyl chain. In this study we also used a "free" chromophore which we chose to be perylene. The reorientation dynamics of this probe are well understood in a range of environments.[46-48] Final conclusions are provided in Chapter 6.

Literature Cited

(1) Teles, F. R. R.; Fonseca, L. P. *Talanta* **2008**, *77*, 606-623.

(2) Dauphas, S.; Corlu, A.; Guguen-Guillouzo, C.; Ababou-Girard, S.; Lavastre, O.; Geneste, F. *New Journal of Chemistry* **2008**, *32*, 1228-1234.

(3) Pyun, J. C.; Kim, S. D.; Chung, J. W. *Analytical Biochemistry* **2005**, *347*, 227-233.

(4) Cosnier, S. *Biosensors & Bioelectronics* **1999**, *14*, 443-456.

(5) Guidelli, R.; Aloisi, G.; Becucci, L.; Dolfi, A.; Moncelli, M. R.; Tadini Buoninsegni, F. *Journal of Electroanalytical Chemistry* **2001**, *504*, 1-28.

(6) Willner, I.; Katz, E. *Angewandte Chemie, International Edition* **2000**, *39*, 1181-1218.

(7) Zhang, J.; Chi, Q.; Kuznetsov, A. M.; Hansen, A. G.; Wackerbarth, H.; Christensen, H. E. M.; Andersen, J. E. T.; Ulstrup, J. *Journal of Physical Chemistry B* **2002**, *106*, 1131-1152.

(8) Kamin, R. A.; Wilson, G. S. *Analytical Chemistry* **1980**, *52*, 1198-205.

(9) Leggett, G. J.; Roberts, C. J.; Williams, P. M.; Davies, M. C.; Jackson, D. E.; Tendler, S. J. B. *Langmuir* **1993**, *9*, 2356-62.

(10) Edmiston, P. L.; Saavedra, S. S. *Journal of the American Chemical Society* **1998**, *120*, 1665-1671.

(11) Naumann, R.; Schmidt, E. K.; Jonczyk, A.; Fendler, K.; Kadenbach, B.; Liebermann, T.; Offenhausser, A.; Knoll, W. *Biosensors & Bioelectronics* **1999**, *14*, 651-662.

(12) Plant, A. L.; Brigham-Burke, M.; Petrella, E. C.; Oshannessy, D. J. *Analytical Biochemistry* **1995**, *226*, 342-8.

(13) Krysinski, P.; Zebrowska, A.; Michota, A.; Bukowska, J.; Becucci, L.; Moncelli, M. R. *Langmuir* **2001**, *17*, 3852-3857.

(14) Becucci, L.; Guidelli, R.; Peggion, C.; Toniolo, C.; Moncelli, M. R. *Journal of Electroanalytical Chemistry* **2005**, *576*, 121-128.

(15) Steinem, C.; Janshoff, A.; Ulrich, W.-P.; Sieber, M.; Galla, H.-J. *Biochimica et Biophysica Acta, Biomembranes* **1996**, *1279*, 169-80.

(16) Becucci, L.; Innocenti, M.; Salvietti, E.; Rindi, A.; Pasquini, I.; Vassalli, M.; Foresti, M. L.; Guidelli, R. *Electrochimica Acta* **2008**, *53*, 6372-6379.

(17) Steinem, C.; Janshoff, A.; von dem Bruch, K.; Reihs, K.; Goossens, J.; Galla, H.-J. *Bioelectrochemistry and Bioenergetics* **1998**, *45*, 17-26.

(18) Twardowski, M.; Nuzzo, R. G. *Langmuir* **2003**, *19*, 9781-9791.

(19) Ha, J.; Henry, C. S.; Fritsch, I. *Langmuir* **1998**, *14*, 5850-5857.

(20) Plant, A. L. *Langmuir* **1993**, *9*, 2764-7.

(21) Majewski, J.; Wong, J. Y.; Park, C. K.; Seitz, M.; Israelachvili, J. N.; Smith, G. S. *Biophysical Journal* **1998**, *75*, 2363-2367.

(22) Cassier, T.; Sinner, A.; Offenhauser, A.; Mohwald, H. *Colloids and Surfaces, B: Biointerfaces* **1999**, *15*, 215-225.

(23) Naumann, R.; Schiller, S. M.; Giess, F.; Grohe, B.; Hartman, K. B.; Kaercher, I.; Koeper, I.; Luebben, J.; Vasilev, K.; Knoll, W. *Langmuir* **2003**, *19*, 5435-5443.

(24) Naumann, R.; Walz, D.; Schiller, S. M.; Knoll, W. *Journal of Electroanalytical Chemistry* **2003**, *550-551*, 241-252.

(25) Merzlyakov, M.; Li, E.; Casas, R.; Hristova, K. *Langmuir* **2006**, *22*, 6986-6992.

(26) Wagner, M. L.; Tamm, L. K. *Biophysical Journal* **2000**, *79*, 1400-1414.

(27) Merzlyakov, M.; Li, E.; Gitsov, I.; Hristova, K. *Langmuir* **2006**, *22*, 10145-10151.

(28) Porter, M. D.; Bright, T. B.; Allara, D. L.; Chidsey, C. E. D. *Journal of the American Chemical Society* **1987**, *109*, 3559-68.

(29) Karpovich, D. S.; Blanchard, G. J. *Langmuir* **1994**, *10*, 3315-22.

(30) Schessler, H. M.; Karpovich, D. S.; Blanchard, G. J. *Journal of the American Chemical Society* **1996**, *118*, 9645-9651.

(31) Brian, A. A.; McConnell, H. M. *Proceedings of the National Academy of Sciences of the United States of America* **1984**, *81*, 6159-63.

(32) Hillebrandt, H.; Wiegand, G.; Tanaka, M.; Sackmann, E. *Langmuir* **1999**, *15*, 8451-8459.

(33) Dominska, M.; Jackowska, K.; Krysinski, P.; Blanchard, G. J. *Journal of Physical Chemistry B* **2005**, *109*, 15812-15821.

(34) Dominska, M.; Krysinski, P.; Blanchard, G. J. *Journal of Physical Chemistry B* **2005**, *109*, 15822-15827.

(35) Dominska, M.; Krysinski, P.; Blanchard, G. J. *Langmuir* **2008**, *24*, 8785-8793.

(36) Mazur, M.; Blanchard, G. J. *Journal of Physical Chemistry B* **2004**, *108*, 1038-1045.

(37) Moriconi, E. J.; Rakoczy, B.; O'Connor, W. F. *Journal of Organic Chemistry* **1962**, *27*, 2772-6.

(38) Creager, S. E.; Wooster, T. T. *Analytical Chemistry* **1998**, *70*, 4257-4263.

(39) Creager, S.; Yu, C. J.; Bamdad, C.; O'Connor, S.; MacLean, T.; Lam, E.; Chong, Y.; Olsen, G. T.; Luo, J.; Gozin, M.; Kayyem, J. F. *Journal of the American Chemical Society* **1999**, *121*, 1059-1064.

(40) Weber, K.; Hockett, L.; Creager, S. *Journal of Physical Chemistry B* **1997**, *101*, 8286-8291.

(41) Debye, P. *Polar Molecules*, 1957.

(42) Hu, C.-M.; Zwanzig, R. *Journal of Chemical Physics* **1974**, *60*, 4354-7.

(43) Perrin, F. *Journal de Physique et le Radium* **1936**, *7*, 1-11.

(44) Chuang, T. J.; Eisenthal, K. B. *Journal of Chemical Physics* **1972**, *57*, 5094-7.

(45) Lipari, G.; Szabo, A. *Biophysical Journal* **1980**, *30*, 489-506.

(46) Stevenson, S. A.; Blanchard, G. J. *Journal of Physical Chemistry B* **2006**, *110*, 13005-13010.

(47) Koan, M. M.; Blanchard, G. J. *Journal of Physical Chemistry B* **2006**, *110*, 16584-16590.

(48) Lapinski, M. M.; Blanchard, G. J. *Chemistry and Physics of Lipids* **2008**, *153*, 130-137.

CHAPTER 2

PROBING INTERFACIAL ORGANIZATION IN SURFACE MONOLAYERS USING TETHERED PYRENE. 1. STRUCTURAL MEDIATION OF ELECTRON AND PROTON ACCESS TO ADSORBATES

Introduction

The development of self-assembling monolayer chemistry, pioneered by Nuzzo and Allara for disulfides and thiols on gold,[1] and subsequently expanded to a range of different surfaces and bonding chemistries, has served as a versatile and powerful means for controlling interfacial properties. Self-assembled monolayers (SAMs) provide ready access to experimental systems where the physical properties of interfaces can be modified, and the chemical identities of the interfacial species can be examined by spectroscopic and electrochemical techniques. Because of the structural versatility of SAMs and the relative ease with which they can be synthesized, there is a great deal of practical interest in these materials as potential chemical and biological sensing systems.

Since the original work on thiol/gold chemistry and carboxylic acid/alumina bonding strategies,[2,3] there has been a significant effort aimed at making SAM structures more robust. The gold-sulfur bond responsible for alkanethiol/gold monolayer formation is modest in strength, and this fact is ultimately responsible for the labile nature of this family of interfaces.[4,5] Indeed, there is interest not only in the formation of enthalpically more robust mono- and multilayers, but there has also been a sustained effort to create interfacial layers on oxide surfaces, for a variety of fundamental and practical reasons. The growth of interfacial mono- and multilayer structures using metal bisphosphonate and related ionic interlayer linking chemistry was developed by the Mallouk, Thompson and Katz groups,[6-11] and is in wide use today. Similarly, there have been several reports of covalent interlayer linking chemistry to form robust, simple mono- and multilayer interfaces on oxide surfaces such as indium-doped tin oxide (ITO) and SiO_X.[12,13] Until recently, the chemical methodologies appropriate for layer formation on relatively well organized metal surfaces have not been accessible to the chemical approaches used on oxide surfaces. Recent work by Krysiński and Blanchard has shown that the electrochemical formation of an oxide layer on a gold surface can be reacted with acid chlorides, which serve to stabilize the gold oxide layer by forming a gold-ester.[14] This advance has brought the chemistry previously restricted to layer growth on oxide surfaces to more organized metallic substrates.

Given the broad range of means available for the creation of interfacial structures, it is important to consider the ways in which these interfaces can be characterized. The "standard" techniques such as optical ellipsometry, contact angle measurement and infrared (IR) spectroscopy are not well suited to providing direct information on the molecular scale organization of these interfacial structures. This spatially averaged information is very useful, but recently it has been shown that such data can be misleading.[15] If these interfacial structures are to be used for chemical sensing, the intrinsic selectivity of the interface, which is determined at the molecular level, must be probed directly. It is this purpose which we address here. We have designed a series of SAMs that contain pyrene derivatives bound covalently to either gold or oxide (ITO, SiO_X) surfaces. Pyrene is a well known chromophore used to characterize local "polarity", and both its time- and frequency-domain spectral properties can be used to measure short range organization within mono- and multilayer structures. The electrochemistry of pyrene is also well understood, particularly with respect to its oxidative instability. Interrogating both the spectroscopic and electrochemical behavior of covalently bound pyrene on metallic and oxide substrates allows us to gain access to local organization in these systems as a function of the interface chemical identity. In this first of two chapters, we report on the electrochemical response of tethered pyrene derivatives on Au and ITO substrates. We have found that the organization of several of these monolayers depends sensitively on both interface composition and on the existence and polarity of any liquid overlayers on the interface.

Experimental

Chemicals. 1-Pyrenebutyric acid (97%), 1-pyrenemethylamine hydrochloride (95%), octadecylamine (97%), 2-mercaptoethylamine (95%), 11-mercaptoundecanoic acid (95%), 10-hydroxydecanoic acid, octadecylmercaptan (98%), 1-hexadecylamine (98%), N,N'-dicyclohexylcarbodiimide (DCC) (99%), adipoyl chloride (≥99%), 4-methylmorpholine (≥99.5%), triethylamine (≥99%), perchloric acid (70%), hexaammineruthenium (III) chloride (98%), potassium ferrocyanide (99%), lithium perchlorate (99.99%), cyclohexane (99%), 1-pentanol (≥99%), acetonitrile (anhydrous) were obtained from Sigma-Aldrich. Dichloromethane and chloroform were obtained from POCH and Mallinckrodt Chemicals. Aqueous solutions were prepared from Milli-Q water.

Preparation of pyrene on short tether for gold substrate. Pyrene bound to gold using a "short tether" (cysteamide of pyrenebutyric acid, designated P7, where the number 7 indicates the number of atoms between the attaching head group and the pyrene moiety) was synthesized according to a standard procedure for peptide synthesis in solution.[16] Pyrenebutyric acid and cysteamine were dissolved in dichloromethane and cooled to 0°C. After 1 h of stirring, DCC in dichloromethane was added and the reaction proceeded at room temperature for 12 hours. The final product was purified by silica-gel column chromatography (Silica gel 60 from Merck, particle size 0.040 – 0.063 mm) and analyzed by IR spectroscopy.

Gold substrate preparation. Gold ball electrodes were cleaned in piranha solution (3:1 concentrated H_2SO_4: 30% H_2O_2). *Caution! Piranha solution reacts violently with* *organic matter and should be handled with extreme care!* The cleaned electrodes were rinsed with water and polarized cyclically (scan rate 100 mV/s) in the -250 to +1650 mV potential range in 1 M $HClO_4$ until reproducible voltammograms were obtained. Next, electrodes were removed from the cell, washed with distilled water, and dried with a stream of nitrogen. The area of the gold ball electrode was 0.135 cm^2, which was determined from the cyclic voltammetry (CV) of a $K_4[Fe(CN)_6]$ solution.[17]

Silica substrate preparation. Silica slides were cleaned by immersion in piranha solution for ca. 20 min, then rinsed with water and dried in a stream of nitrogen.

ITO substrate preparation. Indium-doped tin oxide (ITO) films deposited on silica substrates were cleaned by rinsing with water, ethanol, and acetone, consecutively.

Monolayer preparation. To create a monolayer of P7 on gold, the substrate was exposed to a solution of P7 in dichloromethane for 12 h. The SAM-covered gold electrode was then rinsed with dichloromethane and dried in a stream of nitrogen, then washed with distilled water and dried in a stream of nitrogen. The monolayer of the nominally buried P7 was obtained by immersing a gold electrode into a solution of P7 and octadecyl mercaptan (ODM) (1:1) in dichloromethane for 12 h. For deposition of a monolayer of pyrene tethered a longer distance from the gold substrate, the substrate was first exposed to solution of 11-mercaptoundecanoic acid (MUA) in dichloromethane for 12 h. The resulting SAM-covered gold substrate was rinsed with dichloromethane, dried in a stream of nitrogen and immersed in a solution of pyrenemethylamine and DCC (1:1) in dichloromethane for 12 h, to form a monolayer of mercaptoundecanoic acid pyrenemethylamide (P13). To synthesize a monolayer of "buried" P13, a substrate covered with a monolayer of MUA was immersed in a dichloromethane solution containing pyrenemethylamine, hexadecylamine and DCC (1:1:1) for 12 h.

Monolayers on ITO substrates were synthesized by reaction of the substrate with adipoyl chloride (0.3 mL) in dry acetonitrile (10 mL), using 4-methylmorpholine (0.3 mL) as a Lewis base, under reduced pressure for 1 h. The reacted substrates were removed from solution, rinsed with dry acetonitrile and ethyl acetate, and dried under a stream of dry nitrogen. We synthesized monolayers of tethered pyrene either as the only constituent or as a co-constituent with a long-chain aliphatic moiety. These monolayers were obtained by exposing the adipoyl chloride covered substrate either to a 2 mM solution of pyrenemethylamine in dichloromethane, producing a single-component monolayer of the pyrenemethylamide of adipic acid, P8. For the corresponding monolayer where P8 is "buried", a dichloromethane solution of pyrenemethylamine and hexadecylamine (1:1) is reacted under reduced pressure for 0.5 h. Following this reaction, the substrate was removed from solution, rinsed with dichloromethane and ethyl acetate, and dried under a stream of dry nitrogen. For pyrene tethered further from the substrate, the adipoyl chloride covered substrate was first reacted with a 2 mM solution of 10-hydroxydecanoic acid in dichloromethane. Following the addition of this C_{10} chain, the substrate was removed from the reaction vessel, rinsed with dichloromethane and ethyl acetate, and dried under a stream of dry nitrogen. The substrate thus covered with adipic acid mono-(10-carboxy)-decyl ester was then exposed either to pyrenemethylamine and DCC (1:1) (to form pyrenemethylamide-10-decyl ester, P19) in dichloromethane or to pyrenemethylamine, hexadecylamine, and DCC (1:1:1) in dichloromethane under reduced pressure for 0.5 h. The reacted substrate was removed from solution, rinsed with dichloromethane and ethyl acetate, and dried under a stream of dry nitrogen.

Electrochemistry. Electrochemical measurements were made with a computer-controlled electrochemical workstation (CH Instruments Model 604B and Model 650), using a three-electrode cell with a Pt wire counter electrode. All potentials are quoted versus a Ag | AgCl | 3 M KCl (-52 mV vs. SCE) reference electrode. Experiments were carried out in aqueous 0.01 M, 0.05 M, 0.1 M, 0.5 M and 1 M $HClO_4$ (keeping the ionic strength of 1 M constant by the addition of the appropriate amount of $LiClO_4$), in aqueous 1 mM $K_4[Fe(CN)_6]$ in 0.5 M $LiClO_4$, and in aqueous 1 mM $[Ru(NH_3)_6]Cl_3$ in 0.1 M $LiClO_4$.

Langmuir trough experiments. Langmuir measurements were made with a commercial trough (Nima Technology). Pyrenebutyric acid and octadecylamine solutions (2 mg/mL) were used as surfactants. Several solutions with varying pyrenebutyric acid to octadecylamine molar ratios were spread on the water surface.

Results and Discussion

Pyrene derivatives exposed to electrolyte solution. The purpose of this work is to demonstrate and characterize a group of SAMs modified with pyrene derivatives, with an eye toward the application of these monolayer species as spectroscopic and electrochemical probes of their immediate environment. We have investigated pyrene derivatives bound covalently to gold and ITO substrates by CV. We show in Figure 2.1 the cyclic voltammograms of our pyrene derivatives bound covalently to gold and ITO. In the first scan for each voltammogram we observe an irreversible peak with a maximum above 900 mV. A pair of new, broad redox peaks appears in subsequent scans between 200 and 300 mV. We assign these features to two pairs of poorly resolved redox peaks, centered near 210 mV and 320 mV. Previous work has shown that these peaks are associated with the several possible diol/dione species that are the stable oxidation products of the pyrene ring system.[18]

On the basis of the analysis of electrochemical reactions of surface-bound pyrene on gold and ITO surfaces reported in the literature,[19] the voltammograms presented in Figure 2.2 and Figure 2.3 can be assigned to 1,6-pyrenedione/1,6-dihydroxypyrene (a pair of CV peaks centered around 320 mV), and 1,8-pyrenedione/1,8-dihydroxypyrene, which is shifted to more negative values by ca. 100 mV.[18]

The electrode coverage with various pyrene derivatives was evaluated with use of CV. The amount of pyrene derivatives on the electrode surface was calculated from the charge under the anodic peak from the voltammograms recorded in aqueous 1 M $HClO_4$

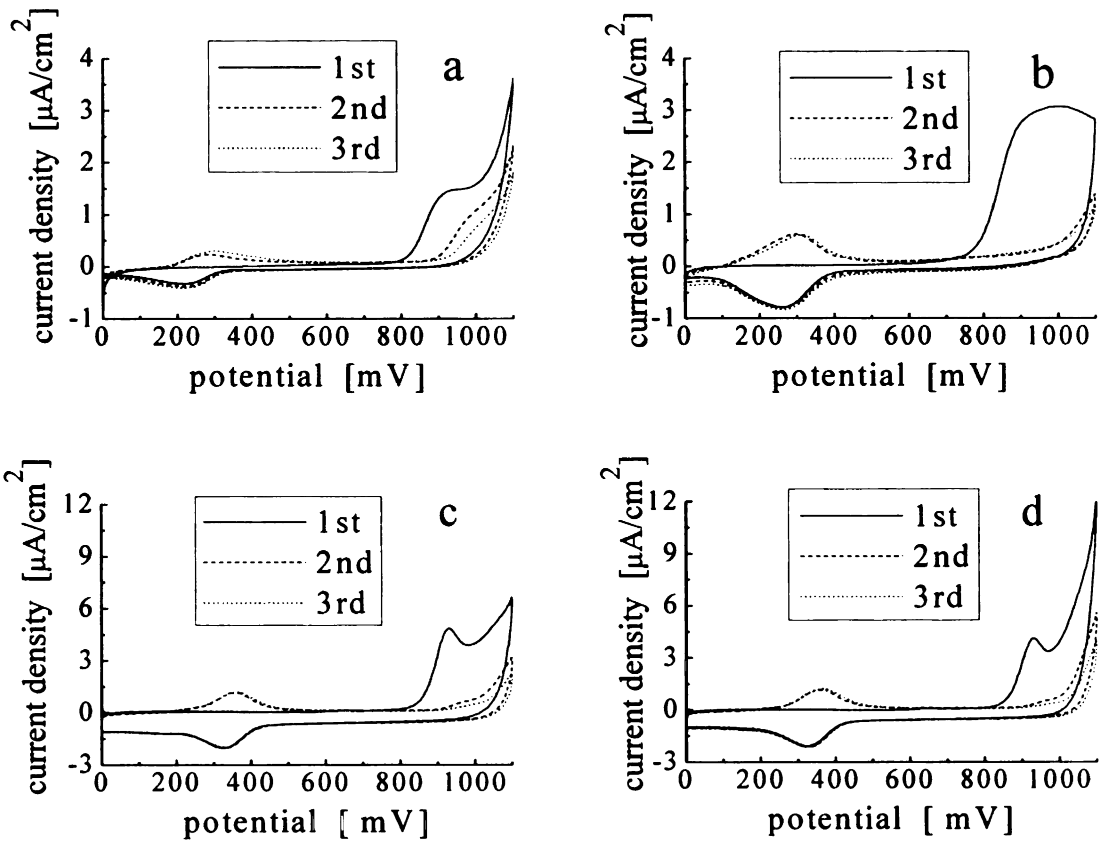

Figure 2.1 Cyclic voltammograms of: (a) P7 on gold in 0.1 M $HClO_4$, sweep rate 2mV/s; (b) P13 on gold in 0.1 M $HClO_4$, sweep rate 5 mV/s; (c) P8 on ITO in 1 M $HClO_4$, sweep rate 20 mV/s; (d) P19 on ITO in 1 M $HClO_4$, sweep rate 20 mV/s.

electrolyte solution (Figure 2.2 and Figure 2.3) at low sweep rate (as specified in figure captions). Integration of this peak yielded a surface coverage (assuming a 2 electron/2 proton process[18]) of ca. 4.4 x 10^{-11} mol/cm^2 for P7 and 1.7 x 10^{-11} mol/cm^2 for P13. These same measurements on an ITO substrate yield a surface coverage of 1.2 x 10^{-11} mol/cm^2 for P8 and 8.4 x 10^{-12} mol/cm^2 for P19. To assess the maximum theoretical coverage for our pyrene derivatives on a given substrate, one has to evaluate the minimum area that can be occupied by a single pyrene ring system with its hydrocarbon tail outstretched from the surface in an all-*trans* configuration. For this purpose we have used the Langmuir technique. Unfortunately, because of the finite solubility of pyrenebutyric acid in water, we could not produce a pressure/area isotherm over the required phase transition range for this compound. Therefore, we have investigated the mixed pyrenebutyric acid/ octadecylamine system with various pyrenebutyric acid mole fractions on a water subphase (Figure 2.4a). It was possible to obtain the pressure-area isotherms of this binary system for up to a 1:1 ratio of the two constituents. By assumption of additive behavior for such a binary mixture on the interface, a plot of the area per molecule as a function of the mole fraction of pyrenebutyric acid in octadecylamine allows us to estimate the area occupied by a single pyrenebutyric acid molecule to be 31.2 $Å^2$ (Figure 2.4b). This value is comparable to that of sterols in a monolayer: 37 $Å^2$/molecule for cholesterol.[20] The value of 31.2 $Å^2$/molecule is entirely reasonable on geometric grounds. For a rigid molecule, one can estimate an area of ca. 26 $Å^2$/molecule based on a molecular mechanics calculation, not taking into account any

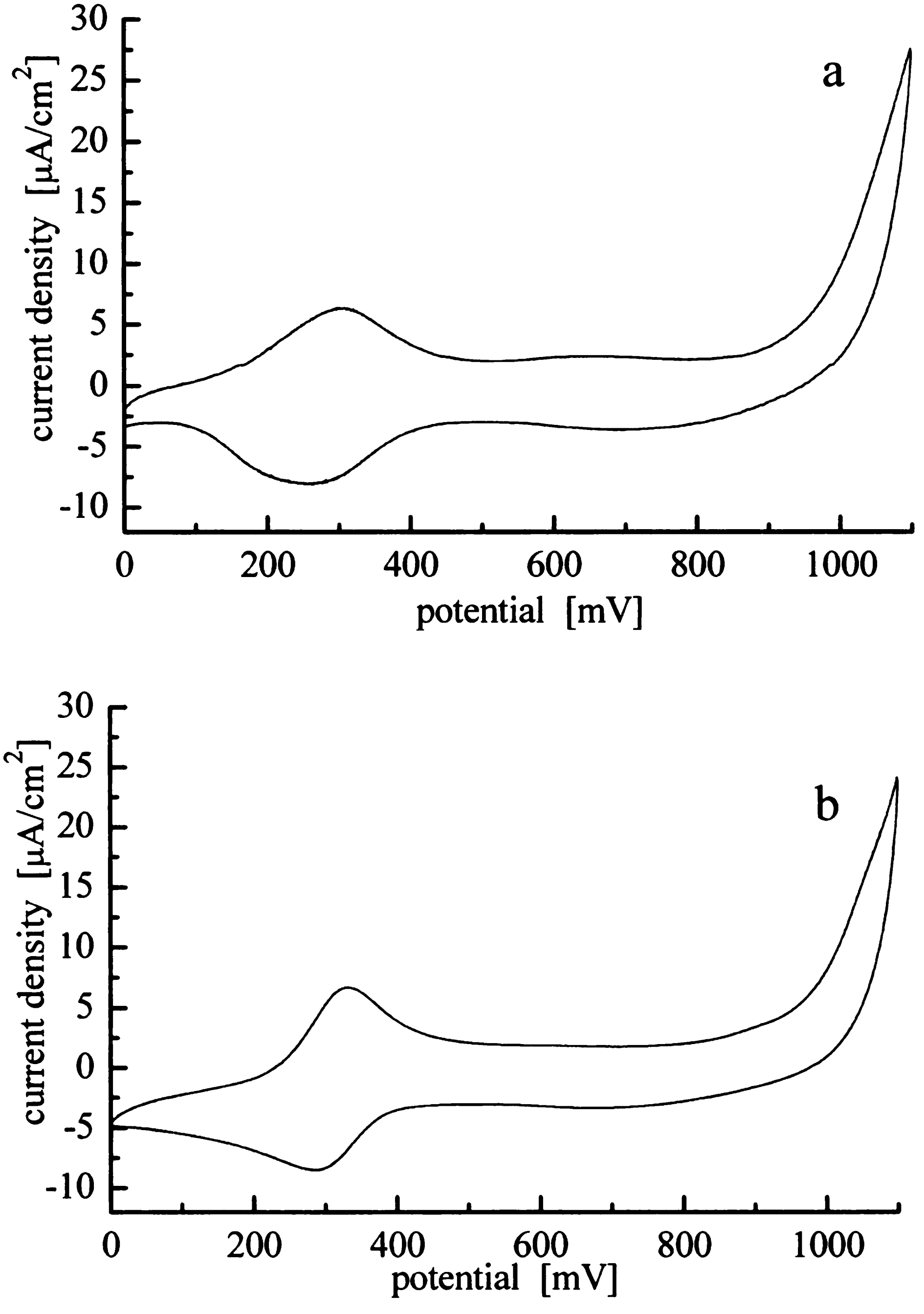

Figure 2.2 Cyclic voltammograms of: (a) P7 and (b) P13 on gold in 1M $HClO_4$. Sweep rate 20 mV/s. Charge under the anodic peak is 2.105 μC for (a) and 3.106 μC for (b).

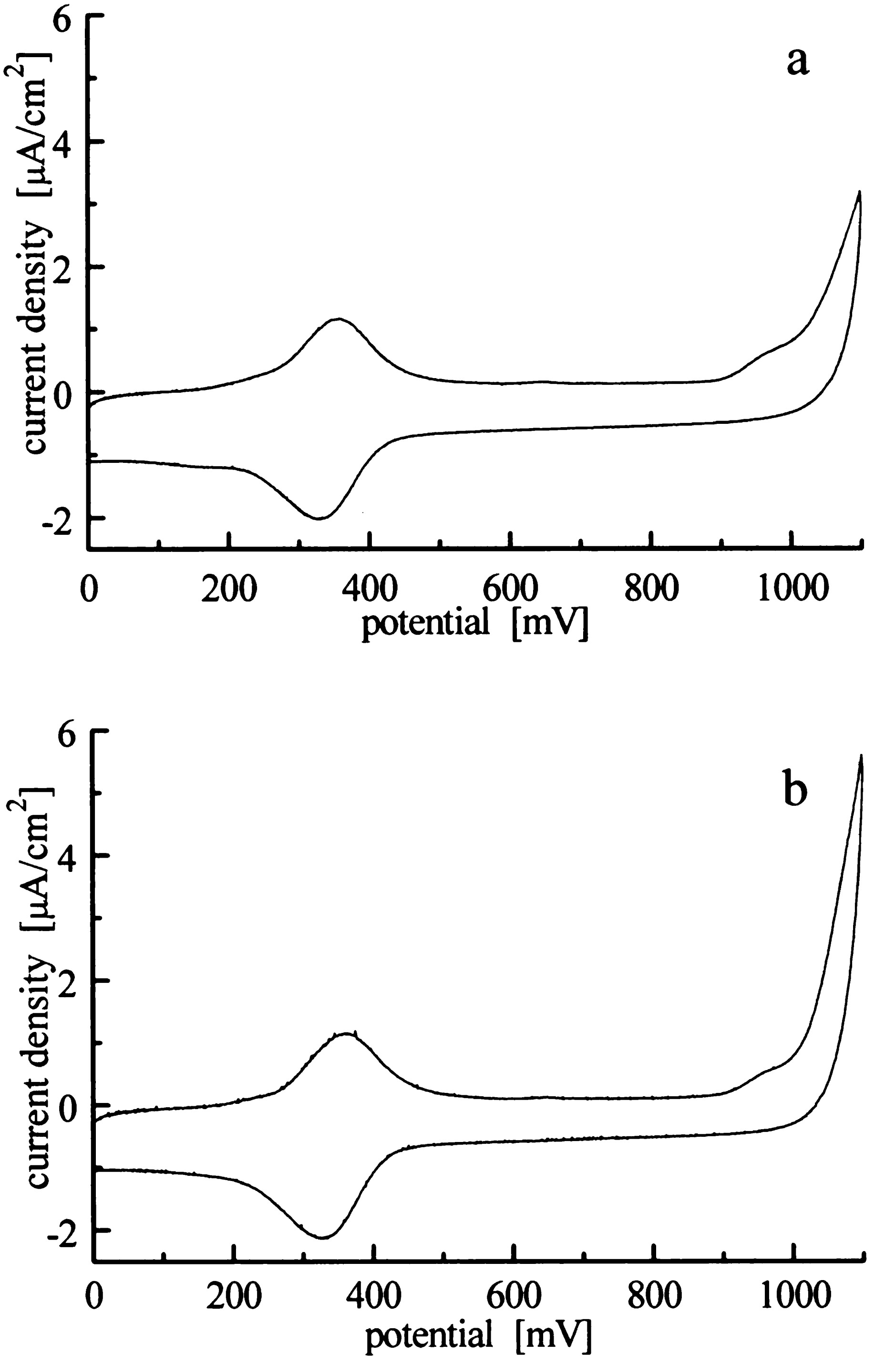

Figure 2.3 Cyclic voltammograms of: (a) P8 and (b) P19 on ITO in 1M $HClO_4$. Sweep rate 20 mV/s. Charge under the anodic peak is 1.048 μC for (a) and 1.345 μC for (b).

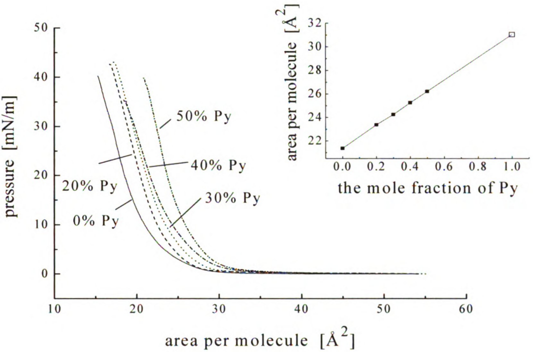

Figure 2.4 Pressure-area isoterms for pyrenebutyric acid and octadecylamine system. Inset: Area per molecule as a function of mole fraction of pyrenebutyric acid in mixture of octadecylamine with different concentrations of pyrenebutyric acid.

motional freedom or alternative conformers of the pyrenebutyric acid molecule. Taking the value of 31.2 Å^2/molecule for our pyrene derivatives, we estimate the maximum surface coverage of pyrene on the electrode surface to be 5.3×10^{-10} mol/cm^2, indicating that the surface coverage we obtain is well below that of a full monolayer.

We used cyclic voltammetry to assess the organization of pyrene-containing monolayers on Au and ITO substrates. Typically, well organized, hydrophobic layers block electron transfer from hydrophilic redox probes present in the supporting electrolyte solution to the conductive substrate. For these interfaces, we have used hexaammineruthenium (III) chloride (1 mM) as the redox-active probe, which produces a quasi-reversible CV curve (not shown). Our data point to poorly organized monolayers, consistent with previous literature reports showing that when cysteamine molecules are used as anchoring moieties to gold (P7), the resulting monolayer adopts a predominantly gauche conformation.[21-23] For such a conformation, one would expect a monolayer with numerous access points to the substrate. For P13, where mercaptoundecanoic acid is the anchoring species, the amide group, formed by reaction of MUA with pyrenemethylamine to form P13, should be solvated, also resulting in a poorly organized monolayer. Thus, the hydrophilic hexaammineruthenium (III) chloride redox probe, regardless of the length of a tether anchoring the pyrene ring system to the substrate, can gain access to the electrode surface, resulting in quasi-reversible voltammetric behavior.

By consideration of the sub-monolayer coverage and relative ease of diffusion for the hexaammineruthenium (III) cation through these layers, as well as the fact that protons participate in the redox reactions (Figure 2.5), we should observe a pH

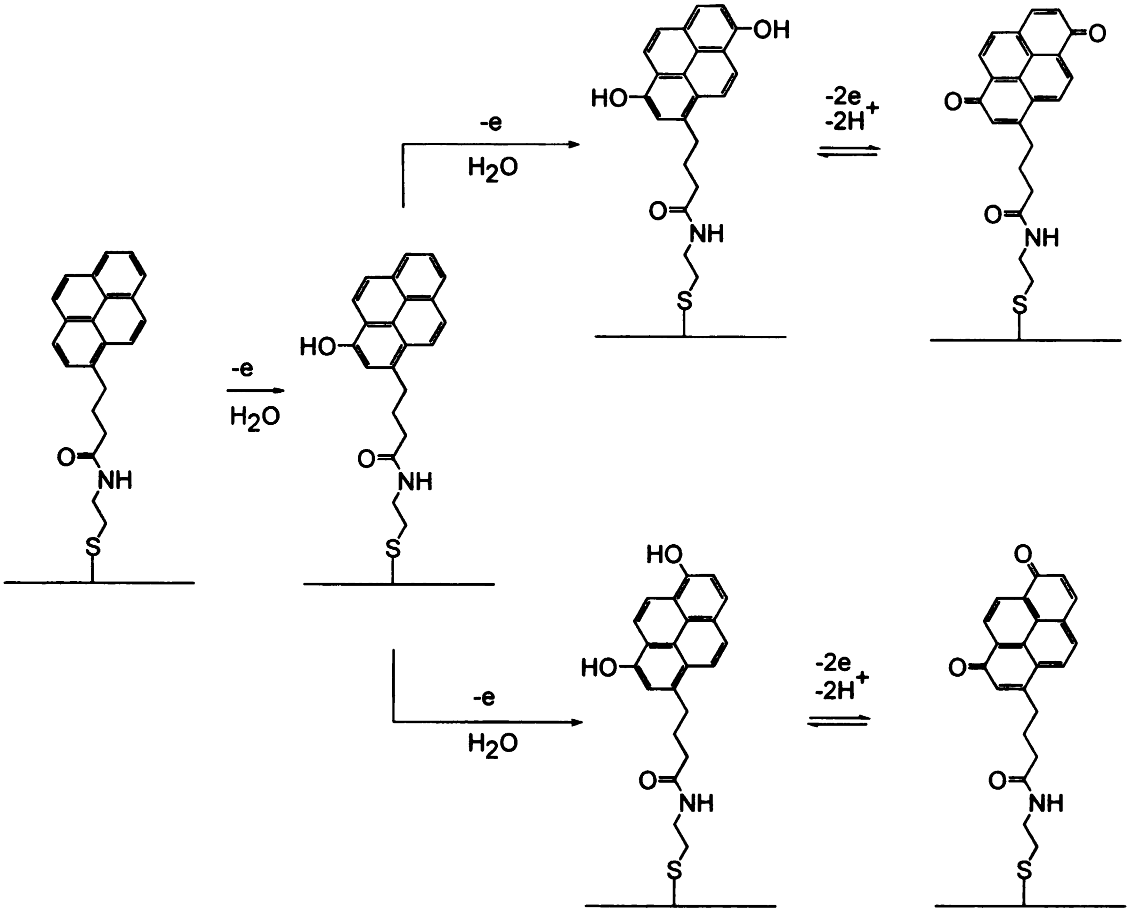

Figure 2.5 Schematic of the redox reactions characteristic of the pyrene moiety (for clarity this drawing shows only the P7 molecule). The structures shown are not an exhaustive list of the reaction products, but are representative of the dominant species.

dependence in the plots of the potential of the midpoint, E_m. Between the maximum of the oxidation peak, E_{pA}, and the potential of the maximum of the reduction peak, E_{pC}, a gradual decrease in pH should lead to a positive shift of the midpoint potential by about 60 mV per unit pH if the ratio of protons to electrons is close to one ($2H^+$, $2e^-$) in the reaction scheme (Figure 2.5) that leads to either 1,6-pyrenedione/1,6-dihydroxypyrene or 1,8-pyrenedione/1,8-dihydroxypyrene.

Figure 2.6 shows the shifts in peak potentials to more positive values with decreasing solution pH. On the basis of CVs for pyrene derivatives obtained in different perchloric acid concentrations we can determine the dependence of the midpoint potential between the anodic and cathodic peaks, E_m, as a function of pH (Figure 2.7). The experimental data show that the slope of plots of the midpoint potential, E_m, is ca. -45 mV/pH unit for both adlayers on gold, and for the ITO substrate, the slope of E_m vs. pH is ca. -53 mV/pH unit. There are several interesting features contained in these data. The first is that the pyrene derivatives anchored to either Au or ITO appear not to undergo a full $2H^+/2e^-$ redox reaction. Rather, the calculated ratio of protons to electrons involved in the unit redox reaction is close to 0.8. Even though this finding is similar to data reported for the ubiquinone/ubiquinol (UQ/UQH_2) redox couple confined to the mercury surface by a phospholipid monolayer,[24-26] where deviations from the expected 60 mV/pH unit were observed for UQ, we believe that the observed deviation from a 1:1

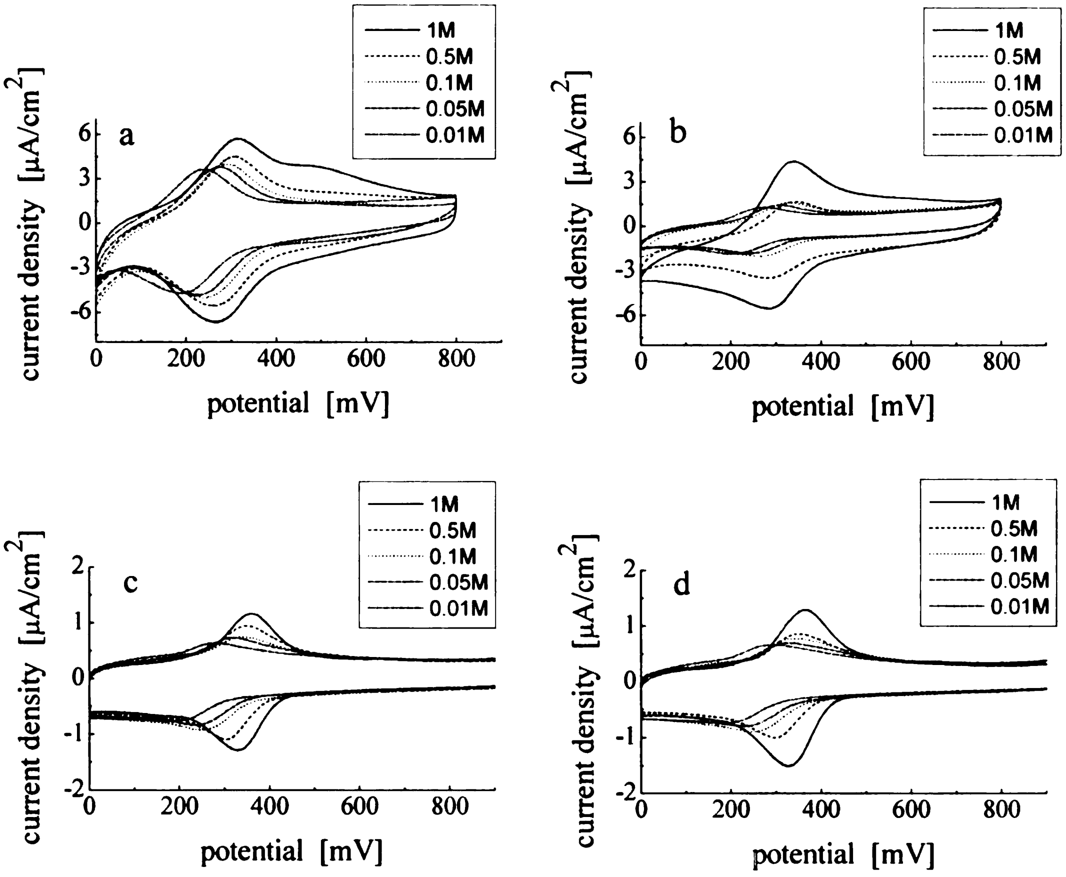

Figure 2.6 Cyclic voltammograms for the pyrene-containing adlayers: (a) P7 on gold; (b) P13 on gold; (c) P8 on ITO; (d) P19 on ITO, all in 1M, 0.5M, 0.1M, 0.05M and 0.01M aqueous $HClO_4$. The ionic strength is maintained at 1 M for all solutions by aqueous $LiClO_4$. The sweep rate was 20 mV/s for all CVs.

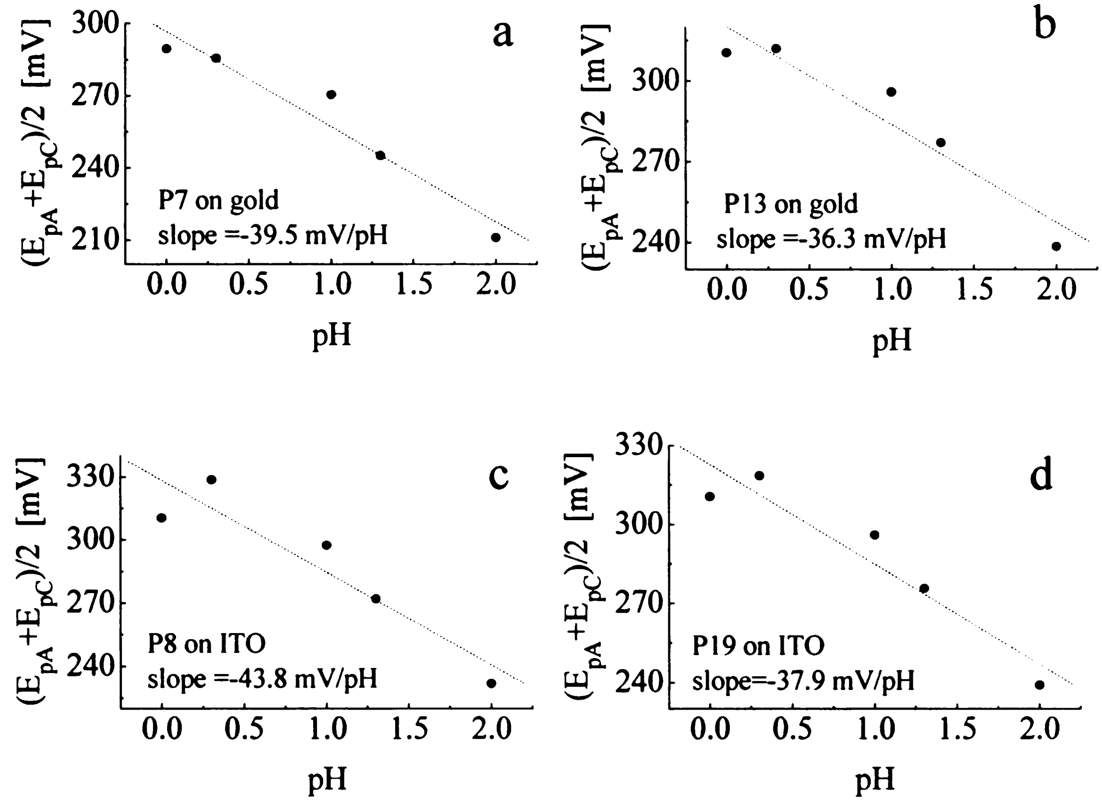

Figure 2.7 Dependence of the midpoint potential, E_m, on the pH of perchloric acid aqueous solutions for: (a) P7 on gold, slope = -39.5 mV/pH, (b) P13 on gold, slope = -36.3 mV/pH, (c) P8 on ITO, slope = -43.8 mV/pH, and (d) P19 on ITO, slope = -37.9 mV/pH. For all scans the sweep rate was 20 mV/s.

$H^+:e^-$ ratio is mainly due to uncertainty in the experimental data (the 1M $HClO_4$ solution, in particular, is of concern).

In the following section, we consider the rate constants for the redox processes that are responsible for the observed behavior. Our previous work has shown that pyrene redox chemistry is explained well in the context of a $2H^+/2e^-$ reaction,[18] and we evaluate the rate constants based on this knowledge. We caution, however, that there are other possible explanations for our data. It is also possible for a $1H^+/1e^-$ reaction to account for our findings, particularly for reactants in a confined space, or for more complex schemes involving disproportionation and/or further reduction to be operative (Figure 2.7) These possibilities have been pointed out previously for the UQ/UQH_2 redox pair.[25] One should also consider that the chemical reaction, involving a protonation step during $Py(O)_2$ reduction and a deprotonation in $Py(OH)_2$ oxidation, is usually the rate determining step, with electron transfer being in quasi-equilibrium.

We have used AC voltammetry to study the redox kinetics of several pyrene derivatives bound as monolayers to Au and ITO. This technique has proven to be particularly useful for the investigation of redox reactions in layered assemblies on electrodes,[27-30] because a variety of information can be obtained from such data. First, for a given reversible reaction, the peak position on the voltammogram gives information on the formal potential of the surface redox reaction. As shown in Figure 2.8, the peak potential values are lower by ca. 58 mV than the formal potential values obtained during the CV experiments by extrapolating the slope of the midpoint potential, E_m vs. pH to pH=0. Since the alternating current (AC) experiments were carried out in 0.1 M $HClO_4$ (pH=1), this smaller value is due to the dependency of the overall process on proton concentration. It is also important to note that the difference in peak position between P13 and P7 is slightly higher than that obtained from direct current CV, yielding the $\Delta(\Delta G^0)$ value of ca. 7 kJ/mol.

In these AC voltammograms (Figure 2.8) we observe a decrease in the peak-to-background current ratio with increase in frequency. Such changes in the magnitude of the AC peak current with the changing frequency of the AC voltage provide information about the rate constant of the reaction. These data are a series of AC voltammograms taken at three selected frequencies to illustrate the behavior of the pyrene redox reaction as a function of tether length and whether the tether length influences the redox kinetics. Creager's group has shown that it is possible to assess the charge-transfer rate constants from such voltammograms by using a relatively simple Randles equivalent circuit for the impedance of an electrode coated with a redox-active film.[27-29] We note that, for the systems we consider here, it can be the chemical step (e.g., protonation/deprotonation) that is rate determining, so the quantitative evaluation of the charge-transfer rate constant, k_{ct}, should be viewed with some caution.

With these caveats in mind, we have used Creager's methodology[27-29] and present the AC data from Figure 2.8 in form of the peak current to background current ratio, $i_{peak} / i_{background}$ vs. log(AC frequency) for a series of voltammograms recorded over a range of frequencies (Figure 2.9). Plotting the AC voltammetry data in the manner

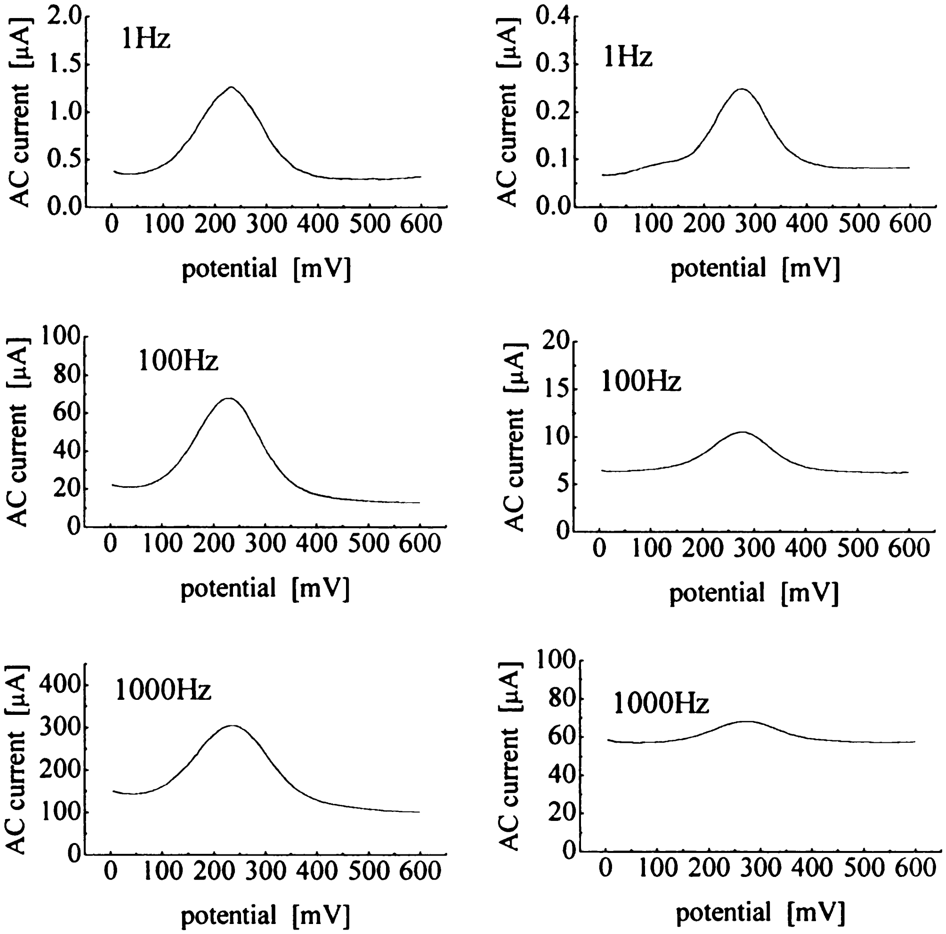

Figure 2.8 AC voltammograms for P7 (left column) and P13 (right column) on gold in 0.1M $HClO_4$. AC frequencies are indicated in each pane.

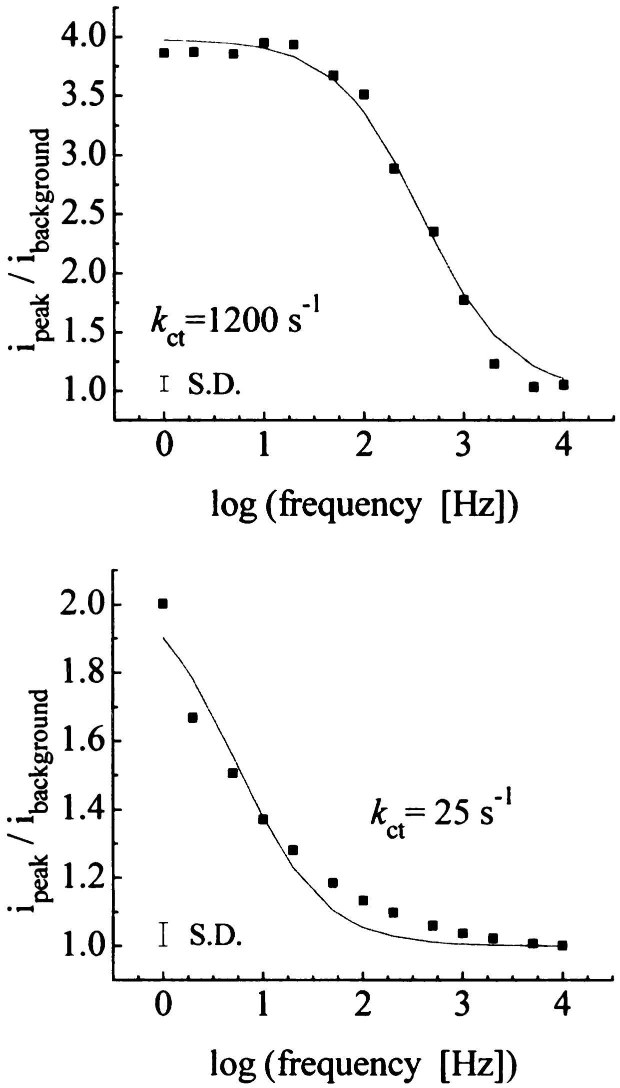

Figure 2.9 i_{peak} / $i_{background}$ vs. log(AC frequency) plots of monolayers of P7 (top graph) and P13 (bottom graph) on gold. The solid lines represent fits to the data (black squares) using a Randles equivalent circuit.[27,28]

shown in Figure 2.9 reveals three distinct regions of the reaction frequency dependence. At low frequencies, the current ratio attains a plateau value that is indicative of the amount of pyrene on the electrode surface; at high frequencies this ratio becomes unity (the AC peak disappears), because the AC sweep rate becomes significantly faster than the reaction kinetics. The intermediate region, where the current ratio is strongly frequency dependent and exhibits a breakpoint frequency, is related to the standard charge transfer rate constant for the redox-active species. By fitting the experimental data (black squares in Figure 2.9) to the Randles model, we extract the rate constants for the monolayers comprised of P7 and P13. For the Au electrodes the recovered rate constants depend strongly on the length of the alkane chain anchoring the pyrene moiety to the electrode surface (k_{ct} = 1200 s^{-1} for P7 and 25 s^{-1} for P13).

It is instructive to consider qualitatively the differences in rate constant values for P7 and P13 in terms of through-bond tunneling that should depend exponentially on the distance and/or the number of C-C bonds in the anchoring chain. By assumption of typical bond lengths (1.79 Å for the C-S bond, 1.27 Å for each C-C bond and 2.6 Å for the amide group),[28,31] we obtain the tunneling constant, β from the experimental k_{ct} values:

$$\ln\left(\frac{k_{ct}'}{k_{ct}''}\right) = \beta\left(d''-d''\right) \qquad (2.1)$$

where k'_{ct} and d' are rate constant and chain length of P7 and k''_{ct} and d'' are the rate constant and chain length of P13. The use of a single tunneling constant, β, for different length anchoring chains warrants some explanation. The tether molecules, aside from their length, vary in the position of the amide group and the pyrene ring system relative to the substrate, but as was suggested in the literature, the contribution of an amide group to the electronic coupling is substantially similar to that of two methylene groups.[32,33] Because of the structural similarities of P7 and P13, we assumed the same tunneling constant for both molecules bound to the electrode surface. The structure dependent tunneling constant is reflective of the decay of electronic coupling between the redox center and the electrode. Therefore, it should also reflect the nature of interactions between the tethered pyrene moieties and their immediate environment, which will include neighboring molecules within the monolayer and solvent molecules that have penetrated the interface. For P7 and P13 bound to gold, Equation 2.1 yields a value of β = 0.44/Å, approximately half the literature value of 0.85/Å for a polymethylene chain.[34] A broad range of β values have been reported in the literature, ranging from the lowest values of 0.4-0.5 for conjugated bridges forming the tether molecules[28,35] and several proteins,[36] to 0.8-1.0 for saturated alkanethiols and hydrocarbons.[30,35-37] However, it is important to note here that, for a monolayer such as P13 on gold, the chemical system is much more complex than the simple Randles approximation and it is not appropriate to fit the experimental data using a single rate constant (cf. Figure 2.9 bottom, R^2=0.95). In our opinion, our results suggest some disorder and dynamical motions in these monolayers, leading to the presence of multiple populations of redox sites with a corresponding distribution of rate constants (and therefore the β values), likely due to a non-uniform orientational and spatial distribution of pyrene moieties within the monolayer. On that basis, the above discussion should be considered qualitative, with the central point being the structural complexity of the interface(s) we have reported here.

We have acquired the analogous AC voltammetry data and performed the same analysis for P8 and P19 on ITO. The data in Figure 2.10 show that the AC peak current diminishes more rapidly with increasing frequency and the fitting procedure yields much smaller k_{ct} values that are barely dependent on the anchoring chain length (k_{ct}=0.2 s^{-1} for P8 and 0.1 s^{-1} for P19, Figure 2.11). This result appears to be counterintuituve, in light of the data for gold substrates. We assume that the ester groups present on the tether chains reduce the rate of electron transfer in a manner analogous to that seen for ether groups,[38] making through-chain electron transfer inefficient. If this is in fact the case, the contribution of intermolecular interactions to the electron transfer process may become significant. Such a contribution could be the result of a highly disorganized interfacial structure, where the tethers of the pyrene derivatives as well as the pyrene rings form disorganized, aggregated structures, thereby maintaining the pyrene ring system at roughly the same average distance from the electrode surface for both P8 and P19.

As was the case for the data taken on a gold substrate, the AC peak position (in 1 M $HClO_4$) denotes the formal potential of these derivatives attached to ITO. We extract from the data a value of +328 mV, in very good agreement with the value of +324 mV obtained for a similar pyrenemethylamine derivative tethered to a gold substrate. This finding implies that the bond between the adlayer and the substrate plays a negligible role

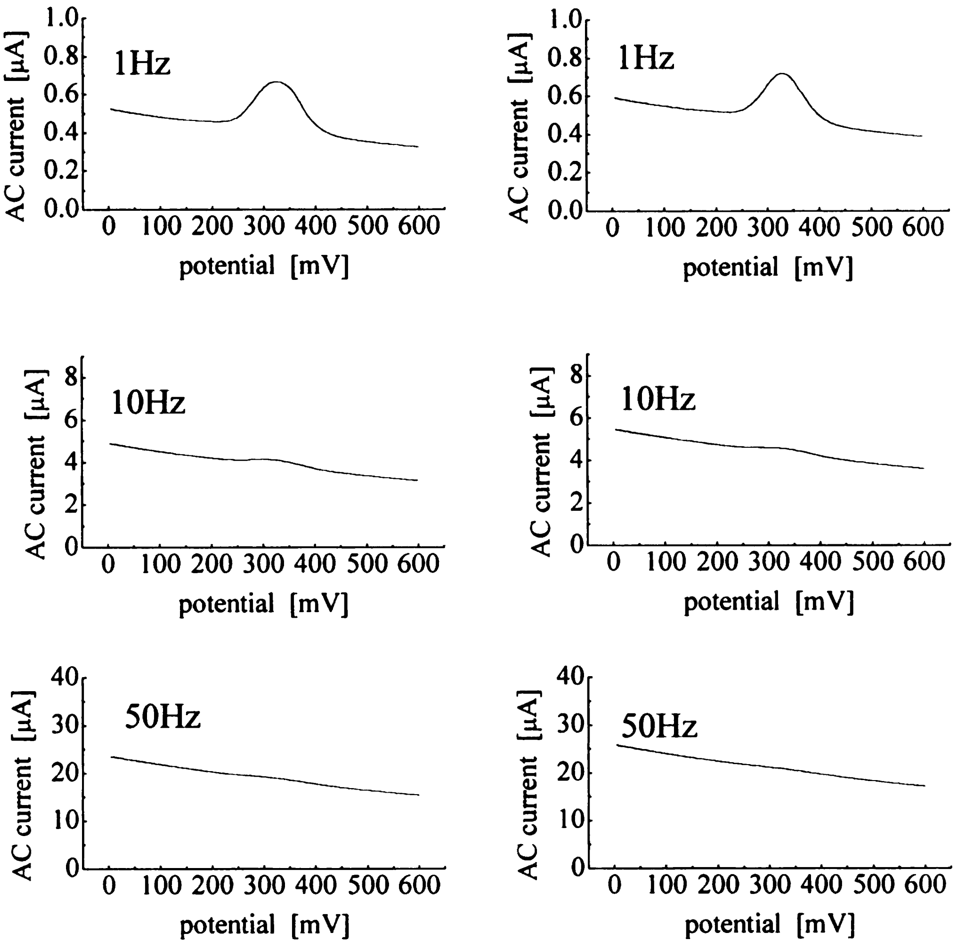

Figure 2.10 AC voltammograms for P8 (left column) and P19 (right column) on ITO in 1 M $HClO_4$.

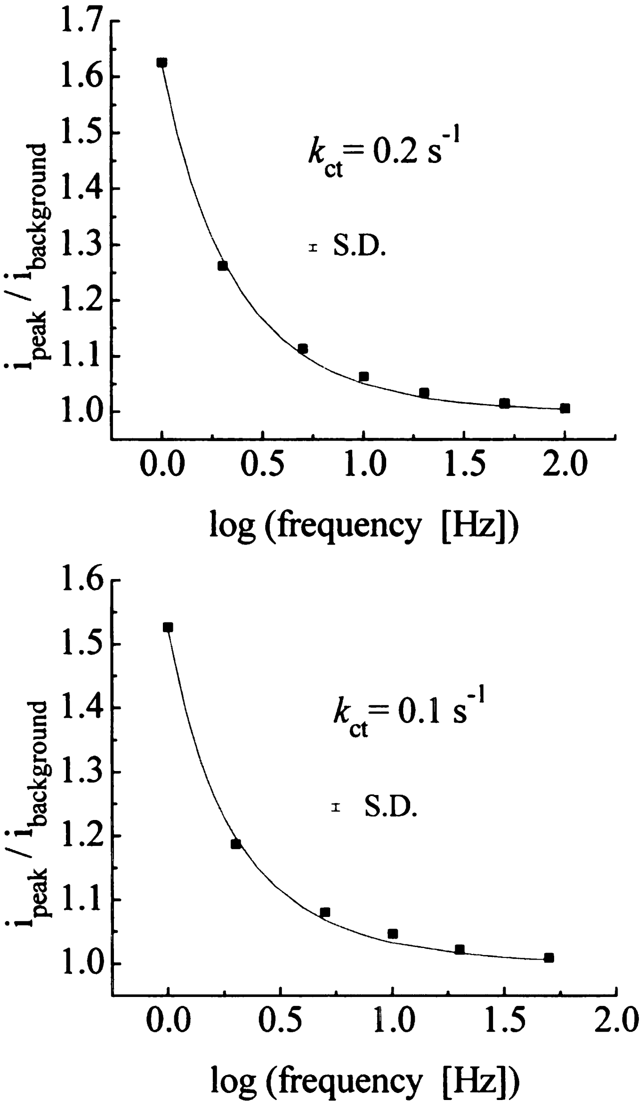

Figure 2.11 i_{peak} / $i_{background}$ vs. log(AC frequency) plots of monolayers of P8 (top graph, $k_{ct} = 0.2\ s^{-1}$) and P19 (bottom graph, $k_{ct} = 0.1\ s^{-1}$) on ITO. The lines represent fits to the data (black squares) using a Randles equivalent circuit.

in the electrochemical responses of these interfaces. Apparently it is only the substituents in closest proximity to the ring system that can influence the redox properties of the pyrene moiety. The aliphatic chain, which mediates the spacing between the pyrene and the substrate, does not affect the redox properties of the ring system.

Pyrene derivatives nominally buried within the monolayer. The results we have considered to this point were obtained for pyrene derivatives, both on gold and ITO, which formed a sub-monolayer of molecules that face the aqueous solution. This system was characterized by substantial motional and structural freedom, as is seen in their electrochemical responses. We consider next our results for a family of interfaces where the pyrene ring system is buried within a mixed monolayer comprised of pyrene-containing species and aliphatic species. For all of the systems we consider, the mixed monolayers contained the same pyrene derivatives as were studied above, but they are coadsorbed with "diluent" molecules of longer hydrocarbon chains. For such systems we expect to observe changes in the electrochemical response of the pyrene moiety, related to the low dielectric environment provided by the diluent molecules, even though the cyclic voltammetry in the presence of the hydrophilic hexaammineruthenium (III) chloride redox probe yielded quasi-reversible voltammograms (not shown), similar to those seen for the corresponding one-component monolayers. Octadecanethiol was the diluent for monolayers containing P7 and the hexadecylamide of mercaptoundecanoic acid was the diluent for monolayers containing P13 on gold substrates. Adipoylhexadecylamide was used as the diluent for monolayers containing P8, and the mono-(9-carboxy)-nonyl ester of adipic acid hexadecylamide was the diluent for monolayers containing P19 on ITO. Apparently, the coadsorbed diluent molecules do not improve the organization and passivation properties of the mixed monolayers compared to the one-component interfaces, and the electrochemical probe can diffuse to the electrode surface.

Figure 2.12 shows the CVs for P7 and P13 with coadsorbed diluents on gold and P8 and P19 with coadsorbed diluents on ITO. Two features of these voltammograms deserve closer inspection. The first is that the charge under the CV peaks is smaller than that for the corresponding one-component monolayers, a finding that we attribute to the coadsorption of two species that are competing for the same surface sites. For gold electrodes we recover a surface coverage of 3×10^{-11} mol/cm^2 for P7 diluted with octadecanethiol and 4×10^{-12} mol/cm^2 for P13 diluted with mercaptoundecanoic acid hexadecylamide. For the ITO substrates, we obtain a coverage of 8.4×10^{-12} mol/cm^2 for P8 diluted with adipoylhexadecylamide and 5.5×10^{-12} mol/cm^2 for P19 diluted with the mono-(9-carboxy)-nonyl ester of adipic acid hexadecylamide.

The other significant feature contained in these data is the splitting of the reduction peak and a "hump" on the oxidation wave of the CV curve for P13 confined within the two-component monolayer. As noted above, these two peaks can be assigned to 1,6-pyrenedione/1,6-dihydroxypyrene (a pair of CV peaks centered around 320 mV), and a contribution from the 1,8-pyrenedione/1,8-dihydroxypyrene redox couple at ca. 210mV. This behavior is better resolved by AC voltammetry (Figure 2.13, right column, 1 Hz) and can be related to the coexistence of two derivatives in energetically well defined populations with relatively little interaction between the redox centers. These features were not seen for the corresponding one-component monolayers, suggesting that

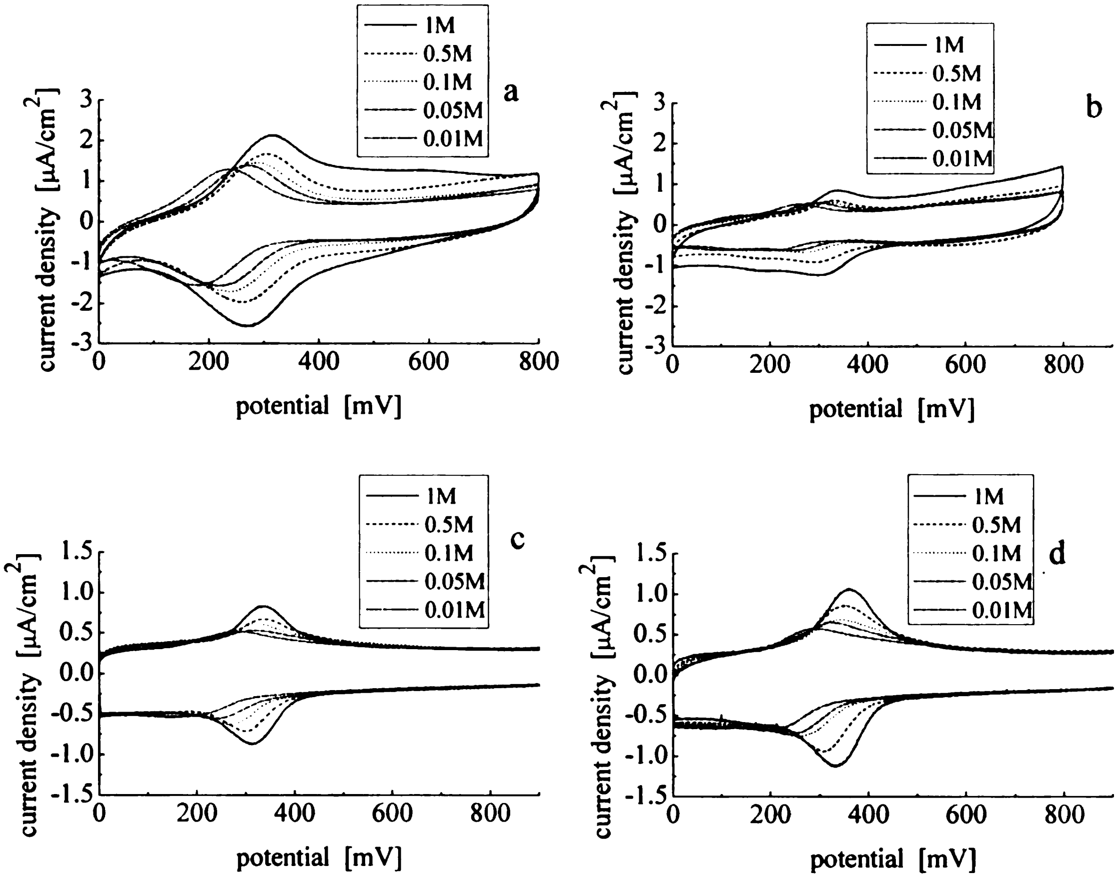

Figure 2.12 CVs for mixed monolayers: (a) P7 + diluent on gold; (b) P13 + diluent on gold; (c) P8 + diluent on ITO; (d) P19 + diluent on ITO in 1, 0.5, 0.1, 0.05 and 0.01 M aqueous $HClO_4$. The ionic strength for all measurements was maintained at 1 M by aqueous $LiClO_4$. Sweep rate 20 mV/s.

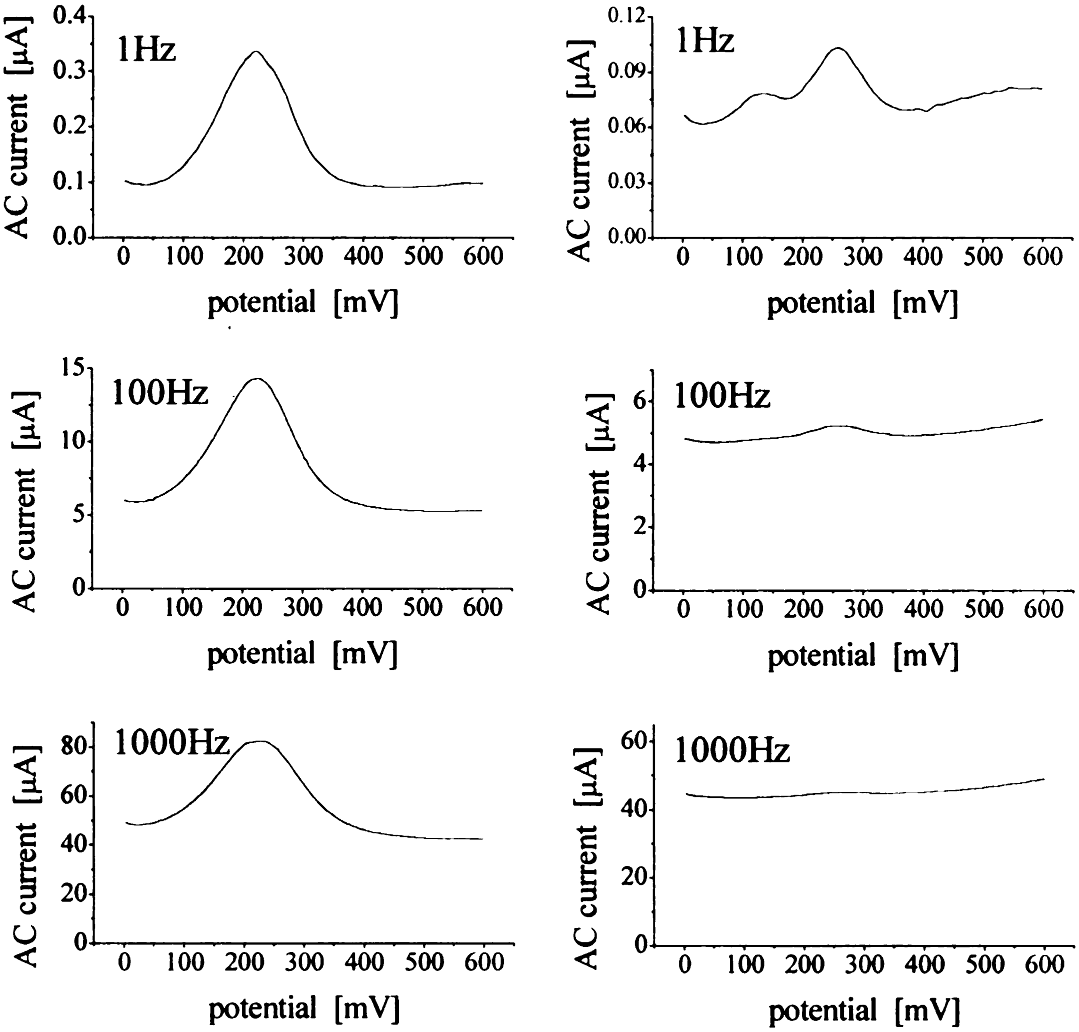

Figure 2.13 AC voltammograms for P7 + diluent (left column) and for P13 + diluent (right column) on gold in 0.1M $HClO_4$.

for the two-component monolayer the different pyrenedione/diol isomers are stabilized by the presence of diluent molecules that separate the redox centers. For the two-component monolayer, the surface concentration of the pyrene derivative is almost 10 times smaller than that of the single-component monolayer, reducing the probability of interactions between different redox centers.

The results presented below are dominated by the 1,6-pyrenedione/1,6-dihydroxypyrene redox couple, which is seen as a pair of CV peaks centered around 320 mV. The 1,8-pyrenedione/1,8-dihydroxypyrene redox couple is seen only on gold for P13, with peaks centered around 130 mV. Figure 2.14 shows the midpoint potential, E_m, vs. pH for the two-component monolayers on gold and ITO substrates. Similar to the data for the one-component monolayers, the slope of E_m vs. pH is ca -46 mV/pH unit for gold, regardless of the anchoring chain length and ca. -49 mV/pH unit for ITO. We consider that these data also indicate a 1:1 proton-to-electron ratio to within the experimental uncertainty in the data, as discussed above for the case of single-component monolayers. These results show that, for our mixed two-component monolayers, the presence of diluent molecules has a negligible influence on the ratio of protons to electrons involved in the pyrene ring system redox reaction. The extrapolation of the slope in Figure 2.14 to pH=0 gives the values of the formal potentials for the different pyrene derivatives in the mixed two-component monolayers. The values of +301 mV for the pyrenebutyric acid derivatives and +339 mV for the pyrenemethylamine derivatives are identical to those obtained for the corresponding one-component monolayers, underscoring the point that the presence of diluent molecules in the monolayer has no

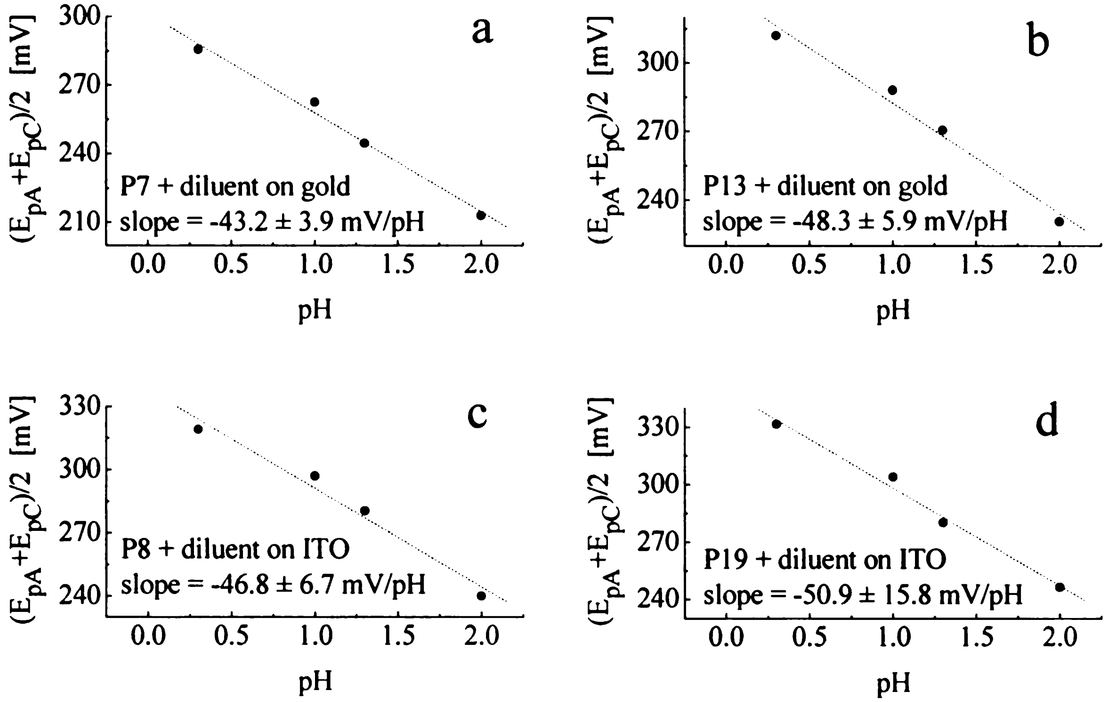

Figure 2.14 Dependence of the midpoint potential, E_m, on pH in 1 M $HClO_4$ aqueous solutions for (a) P7, slope = -43.2 ± 3.9 mV/pH, and (b) P13, slope = -48.3 ± 5.9 mV/pH, in two-component monolayer structures, on gold and for (c) P8, slope = -46.8 ± 6.7 mV/pH and (d) P19, slope = -50.9 ± 15.8 mV/pH, on ITO. Sweep rate 20 mV/s for all scans.

effect on the energetics of redox process. These two-component monolayers are not sufficiently compact to mediate the energetics of the pyrene redox chemistry.

To follow the kinetics of charge transfer in our mixed monolayer systems, we have performed AC voltammetry experiments analogous to those described above for one-component systems (Figure 2.13). The AC voltammograms for these two-component monolayers illustrate that, when the pyrene ring system is confined within a mixed monolayer interior, the AC peak current disappears at much lower frequencies than for the corresponding one-component monolayer. This finding suggests that the kinetics of charge transfer are slower for the two-component system, and we evaluate k_{ct} from plots of $i_{peak} / i_{background}$ vs. log (frequency) (Figure 2.15). These fits yield $k_{ct} = 1100\ s^{-1}$ for P7 + diluent and $21\ s^{-1}$ for P13 + diluent on gold. These results show that the presence of diluent molecules slightly improves the spatial disorder of pyrene moieties within the monolayer.

The data in Figure 2.15 also show that P7 in a two-component monolayer yields a much more complex signal than the Randles approximation can account for, and the experimental data are not fit well using a single rate constant (Figure 2.15 top). Similar behavior has been reported for ferrocene confined within a two-component monolayer and such results have been explained in terms of multiple populations of redox sites, each with a different rate constant.[29,39] The data in Figure 2.15 point to the mixed monolayer structure containing multiple microenvironments for the pyrene rings, resulting in a distribution of charge-transfer rate constants. Our report of a single rate constant should thus be viewed as an average of the several rate constants that contribute to the

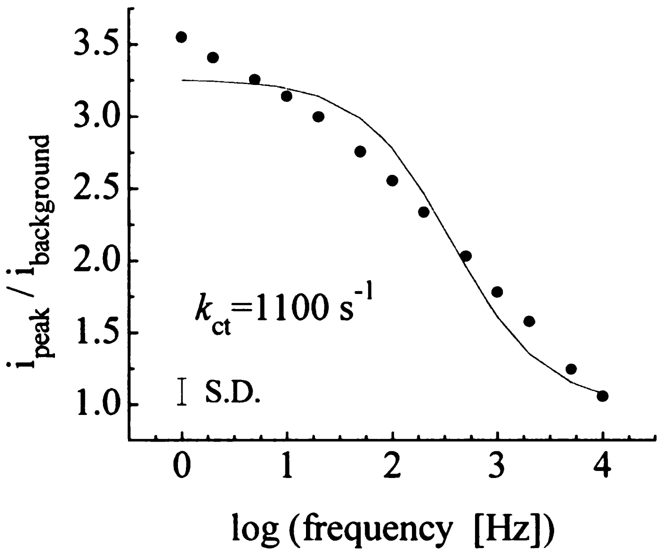

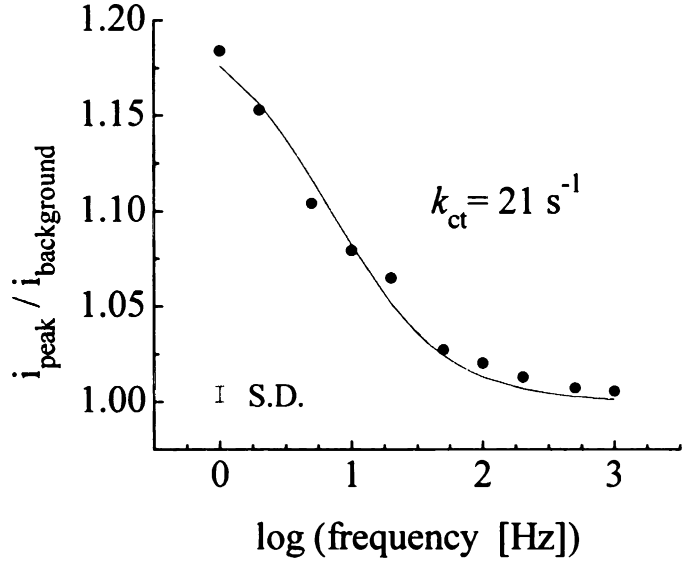

Figure 2.15 $i_{peak} / i_{background}$ vs. log(AC frequency) plots of monolayers of P7 + diluent (top graph) P13 + diluent (bottom graph) on gold. The solid lines represent fits to the data (black squares) using a Randles equivalent circuit.

experimental data.

Analogous experiments for the case of ITO electrodes covered with mixed adlayers containing P8 + diluent or P19 + diluent molecules (Figure 2.16, left and right columns, respectively) show that for these cases the charge-transfer kinetics of pyrene derivatives follow the same pattern as for P7 + diluent and P13 + diluent on gold. The presence of diluent molecules causes the AC voltammetry peak to disappear at lower frequencies as compared to a single-component layer with no diluent. Again, similar to the data for the gold surface, the pyrene ring system attached via a short tether (P8), seems to be less affected than P19 by the presence of diluent molecules. The AC voltammetry data obtained for a range of frequencies are fitted to the Randles model (Figure 2.17 top for P8 + diluent and Figure 2.17 bottom for P19 + diluent). It appears from these plots that, due to the available frequency range of the electrochemical instrumentation, we could get only a threshold of the $i_{peak} / i_{background}$ plot, as the charge-transfer kinetics on ITO are very slow. The resulting larger decrease in the charge-transfer rate constant for the case of P19 + diluent (from 0.1 s^{-1} without diluent to 0.008 s^{-1} with diluent), compared to the k_{ct} decrease for P8 (from 0.2 s^{-1} without diluent to 0.08 s^{-1} with diluent), is indicative of structural confinement and improved organization imposed on the electroactive chromophore by the presence of the diluent molecules. Relatively small differences in the rate constants, compared to the differences in chain lengths of the P8 and P19 molecules (18.8 Å for P8, 32.3 Å for P19), are not consistent with a tunneling mechanism for these data. An implication of these results, as for the single-component monolayers on ITO discussed above, is that these

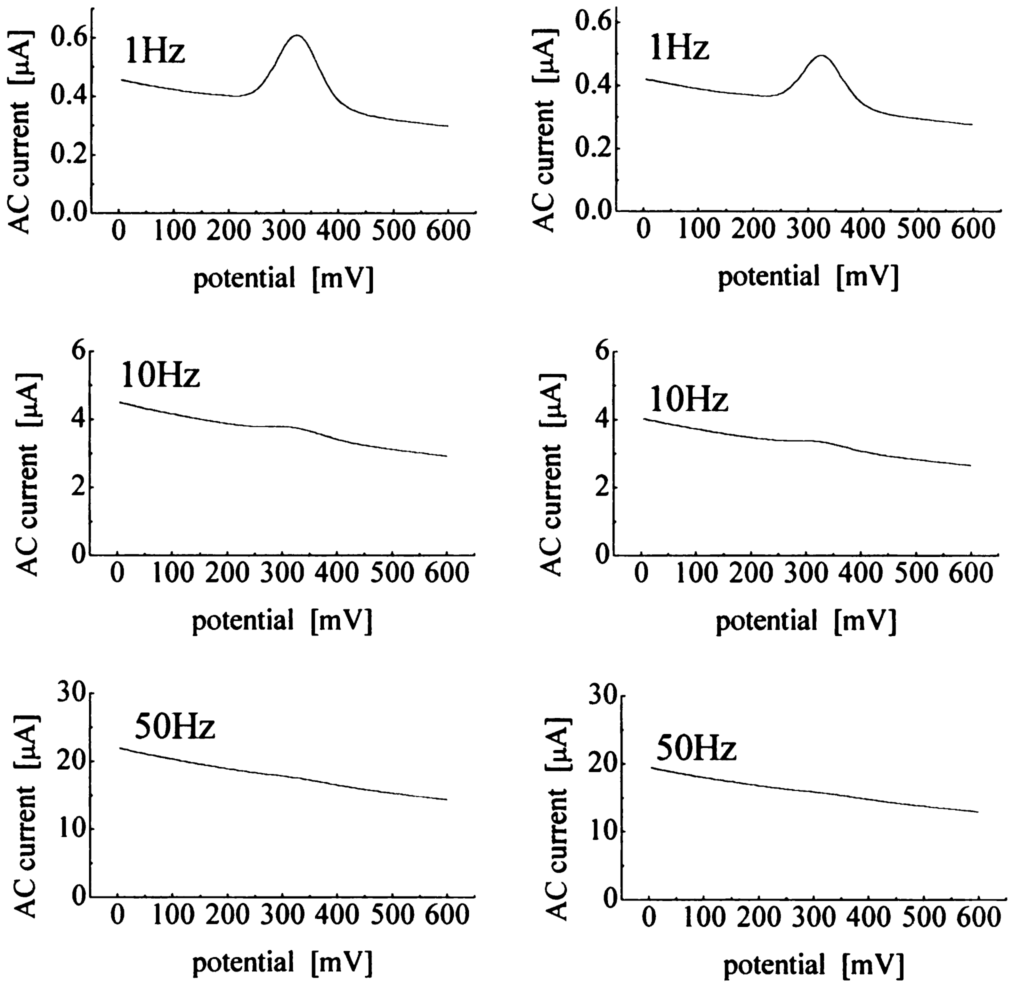

Figure 2.16 AC voltammograms for P8 (left column) and P19 (right column) on ITO in 1 M $HClO_4$.

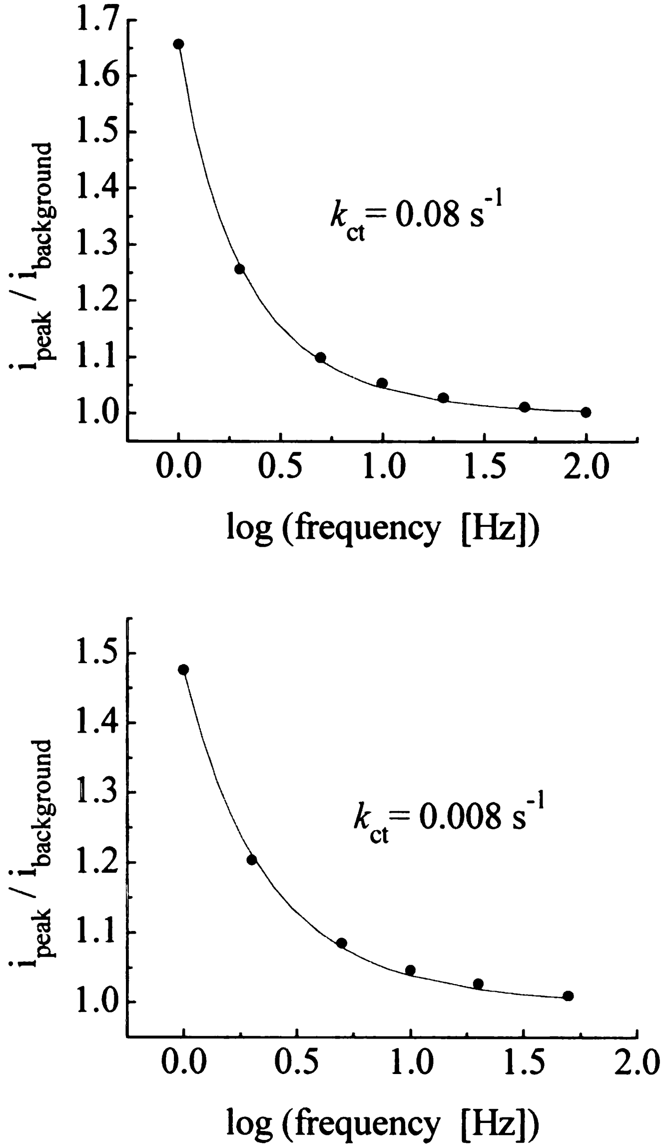

Figure 2.17 i_{peak} / $i_{background}$ vs. log(AC frequency) plots of monolayers of P8 (top graph) and P19 (bottom graph) on ITO. The solid lines represent fits to the data (squares) using a Randles equivalent circuit. The size of symbol used for experimental data is larger then S.D..

monomolecular layers are substantially disordered, with the pyrene moiety position within the layer not being dictated primarily by its tethering chain length. We note, however, that the presence of diluent molecules increases by a factor of 10 the difference in k_{ct} between the short (P8, k_{ct}=0.08 s^{-1}) and long (P19, k_{ct}=0.008 s^{-1}) molecules, in contrast to the data for the corresponding single-component layers (P8, k_{ct}=0.2 s^{-1}; P19, k_{ct}=0.1 s^{-1}).

Conclusions

We have synthesized and characterized a family of SAMs containing pyrene derivatives on gold and ITO substrates. When the covalently bound pyrene ring systems are the only constituents bound to the interfaces, their sub-monolayer coverage ranges from 4.4 x 10^{-11} mol/cm^2 for P7 to 1.7 x 10^{-11} mol/cm^2 for P13 on gold. Similar electrochemical evaluation for the modified ITO substrates yields values of 1.2 x 10^{-11} mol/cm^2 for P8 and 8.4 x 10^{-12} mol/cm^2 for P19. Electrochemical investigations show that these molecules do not form well-ordered, densely packed monolayers, but enjoy significant structural freedom. The use of the Randles model for the evaluation of charge transfer kinetics, followed by the application of the tunneling model to qualitatively evaluate the film thickness dependence of the rate constant, reveal that the monolayers on gold are better organized than those formed on ITO. When the covalently bound pyrene ring systems are codeposited at the interfaces with longer diluent molecules, the presence of these diluent molecules imposes some structural confinement on the tethered pyrene moieties and improved organization can be seen from the charge-transfer kinetics, particularly on gold substrates. Yet these two-component monolayers are not sufficiently compact to mediate the energetics of pyrene redox chemistry. The issues of structural confinement, organization and motional freedom within the monolayer are addressed in details by means of steady-state and time-resolved emission spectroscopy in Chapter 2.

Literature Cited

(1) Nuzzo, R. G.; Allara, D. L. *Journal of the American Chemical Society* **1983**, *105*, 4481-3.

(2) Allara, D. L.; Nuzzo, R. G. *Langmuir* **1985**, *1*, 45-52.

(3) Allara, D. L.; Nuzzo, R. G. *Langmuir* **1985**, *1*, 52-66.

(4) Karpovich, D. S.; Blanchard, G. J. *Langmuir* **1994**, *10*, 3315-22.

(5) Schessler, H. M.; Karpovich, D. S.; Blanchard, G. J. *Journal of the American Chemical Society* **1996**, *118*, 9645-9651.

(6) Lee, H.; Kepley, L. J.; Hong, H. G.; Akhter, S.; Mallouk, T. E. *Journal of Physical Chemistry* **1988**, *92*, 2597-601.

(7) Lee, H.; Kepley, L. J.; Hong, H. G.; Mallouk, T. E. *Journal of the American Chemical Society* **1988**, *110*, 618-20.

(8) Burwell, D. A.; Thompson, M. E. *Chemistry of Materials* **1991**, *3*, 730-7.

(9) Vermeulen, L. A.; Snover, J. L.; Sapochak, L. S.; Thompson, M. E. *Journal of the American Chemical Society* **1993**, *115*, 11767-74.

(10) Putvinski, T. M.; Schilling, M. L.; Katz, H. E.; Chidsey, C. E. D.; Mujsce, A. M.; Emerson, A. B. *Langmuir* **1990**, *6*, 1567-71.

(11) Katz, H. E.; Schilling, M. L.; Chidsey, C. E. D.; Putvinski, T. M.; Hutton, R. S. *Chemistry of Materials* **1991**, *3*, 699-703.

(12) Kohli, P.; Blanchard, G. J. *Langmuir* **2000**, *16*, 4655-4661.

(13) Major, J. S.; Blanchard, G. J. *Chemistry of Materials* **2002**, *14*, 2574-2581.

(14) Krysinski, P.; Blanchard, G. J. *Bioelectrochemistry* **2005**, *66*, 71-77.

(15) Gupta, P.; Ulman, A.; Fanfan, S.; Korniakov, A.; Loos, K. *Journal of the American Chemical Society* **2005**, *127*, 4-5.

(16) Wróbel, J. T.; Kabzinska, K. *Preparatyka i elementy syntezy organicznej*; PWN: Warszawa, 1983.

(17) Krysinski, P.; Brzostowska-Smolska, M. *Journal of Electroanalytical Chemistry* **1997**, *424*, 61-67.

(18) Mazur, M.; Blanchard, G. J. *Journal of Physical Chemistry B* **2004**, *108*, 1038-1045.

(19) Moriconi, E. J.; Rakoczy, B.; O'Connor, W. F. *Journal of Organic Chemistry* **1962**, *27*, 2772-6.

(20) Serfis, A. B.; Brancato, S.; Fliesler, S. J. *Biochimica et Biophysica Acta, Biomembranes* **2001**, *1511*, 341-348.

(21) Kudelski, A. *Journal of Raman Spectroscopy* **2003**, *34*, 853-862.

(22) Wirde, M.; Gelius, U.; Nyholm, L. *Langmuir* **1999**, *15*, 6370-6378.

(23) Michota, A.; Kudelski, A.; Bukowska, J. *Surface Science* **2002**, *502-503*, 214-218.

(24) Gordillo, G. J.; Schiffrin, D. J. *Faraday Discussions* **2000**, *116*, 89-107.

(25) Moncelli, M. R.; Herrero, R.; Becucci, L.; Guidelli, R. *Biochimica et Biophysica Acta, Bioenergetics* **1998**, *1364*, 373-384.

(26) Moncelli, M. R.; Becucci, L.; Nelson, A.; Guidelli, R. *Biophysical Journal* **1996**, *70*, 2716-2726.

(27) Creager, S. E.; Wooster, T. T. *Analytical Chemistry* **1998**, *70*, 4257-4263.

(28) Creager, S.; Yu, C. J.; Bamdad, C.; O'Connor, S.; MacLean, T.; Lam, E.; Chong, Y.; Olsen, G. T.; Luo, J.; Gozin, M.; Kayyem, J. F. *Journal of the American Chemical Society* **1999**, *121*, 1059-1064.

(29) Sumner, J. J.; Creager, S. E. *Journal of Physical Chemistry B* **2001**, *105*, 8739-8745.

(30) Sek, S.; Sepiol, A.; Tolak, A.; Misicka, A.; Bilewicz, R. *Journal of Physical Chemistry B* **2004**, *108*, 8102-8105.

(31) Bain, C. D.; Troughton, E. B.; Tao, Y. T.; Evall, J.; Whitesides, G. M.; Nuzzo, R. G. *Journal of the American Chemical Society* **1989**, *111*, 321-35.

(32) Sumner, J. J.; Weber, K. S.; Hockett, L. A.; Creager, S. E. *Journal of Physical Chemistry B* **2000**, *104*, 7449-7454.

(33) Sek, S.; Palys, B.; Bilewicz, R. *Journal of Physical Chemistry B* **2002**, *106*, 5907-5914.

(34) Weber, K.; Hockett, L.; Creager, S. *Journal of Physical Chemistry B* **1997**, *101*, 8286-8291.

(35) Sachs, S. B.; Dudek, S. P.; Hsung, R. P.; Sita, L. R.; Smalley, J. F.; Newton, M. D.; Feldberg, S. W.; Chidsey, C. E. D. *Journal of the American Chemical Society* **1997**, *119*, 10563-10564.

(36) Kasmi, A. E.; Wallace, J. M.; Bowden, E. F.; Binet, S. M.; Linderman, R. J. *Journal of the American Chemical Society* **1998**, *120*, 225-226.

(37) Slowinski, K.; Chamberlain, R. V.; Miller, C. J.; Majda, M. *Journal of the American Chemical Society* **1997**, *119*, 11910-11919.

(38) Napper, A. M.; Liu, H.; Waldeck, D. H. *Journal of Physical Chemistry B* **2001**, *105*, 7699-7707.

(39) Li, J.; Schuler, K.; Creager, S. E. *Journal of the Electrochemical Society* **2000**, *147*, 4584-4588.

CHAPTER 3

PROBING INTERFACIAL ORGANIZATION IN SURFACE MONOLAYERS USING TETHERED PYRENE. 2. SPECTROSCOPY AND MOTIONAL FREEDOM OF THE ADSORBATES

Introduction

The characterization of interfaces is an area of critical importance to materials science and biology because interfaces mediate processes ranging from chemical sensing to cell wall permeability. Our group has been actively involved in the spectroscopic and electrochemical characterization of metallic and oxide interfaces because of their broad use in chemical sensing. The interfaces that have received the bulk of the attention have been self-assembling monolayer and multilayer structures because of their comparative ease of preparation and their ability to mediate a host of properties, such as electron-transfer kinetics[1] and chemical selectivity.[2,3]

The structure and properties of mono- and multilayer interfaces are determined to a significant extent by the substrate. Metallic interfaces such as gold and other coinage metals produce relatively well organized monolayers using thiols, and such interfaces are amenable to electrochemical characterization. One problem with conductive substrates is the quenching of chromophores located within $\lambda/2$ of the substrate,[4] precluding their use in optical spectroscopic studies. It is thus difficult to make direct comparisons between optical and electrochemical experiments, even for partially transmissive interfaces such as indium-doped tin oxide (ITO) and boron-doped diamond (BDD), owing to their broad background absorption. We have studied the optical and electrochemical responses of several polycyclic aromatic hydrocarbons (PAHs) and we understand the oxidative degradation reactions characteristic for these compounds.[5,6] The kinetics of these reactions depend on the environment of the PAHs, as we have reported in the previous chapter. Electrochemical data indicate that there is only a fraction of a monolayer of pyrene-containing adsorbates on gold and ITO substrates and the monolayers formed using that chemistry exhibit substantial disorder. The purpose of this work is to understand these monolayers from a spectroscopic perspective.

To perform the spectroscopic measurements, we use silica as the substrate material. The surface of silica is different from that of ITO, but our previous work has indicated that the density and distribution of surface –OH groups on these two substrates are similar, and we have found no evidence to date indicating that SiO_X and ITO substrates give rise to different monolayer structures. The data we report here indicate that under all circumstances, the formation of a monolayer structure on silica is accompanied by significant disorder, some of which is related to the solvation of the monolayer and some of which is intrinsic to the monolayer, owing to the spatial distribution of surface silanol sites from which the monolayers are grown.

Experimental

Chemicals. 1-pyrenebutyric acid (97%), 1-pyrenemethylamine hydrochloride (95%), octadecylamine (97%), 10-hydroxydecanoic acid, 1-hexadecylamine (98%), N,N'-dicyclohexylcarbodiimide (DCC, 99%), adipoyl chloride (≥99%), 4-methylmorpholine (≥99.5%), triethylamine (≥99%), cyclohexane (99%), 1-pentanol (≥99%), acetonitrile (anhydrous) were obtained from Sigma-Aldrich. Dichloromethane and chloroform were obtained from POCH and from Mallinckrodt Chemicals.

Surface adlayer constituents. Monolayers on silica substrates were synthesized by reaction of the substrate with adipoyl chloride (0.3 mL) in dry acetonitrile (10 mL), using 4-methylmorpholine (0.3 mL) as a Lewis base, under reduced pressure for 1 h. The reacted substrates were removed from solution, rinsed with dry acetonitrile and ethyl acetate, and dried under a stream of dry nitrogen. We synthesized monolayers of tethered pyrene either as the only constituent or as a coconstituent with a long-chain aliphatic moiety. These monolayers were obtained by exposing the adipoyl chloride covered substrate either to a 2 mM solution of pyrenemethylamine in dichloromethane (producing a layer we designate as P8, where the number refers to the number of atoms in the tether between the pyrene moiety and the substrate) or to a dichloromethane solution of pyrenemethylamine and hexadecylamine (1:1) for 0.5 h. Following this reaction, the substrate was removed from solution, rinsed with dichloromethane and ethyl acetate, and dried under a stream of dry nitrogen. For pyrene tethered further from the substrate, the adipoyl chloride covered substrate was first reacted with a 2 mM solution of 10-hydroxydecanoic acid in dichloromethane. Following the addition of this C_{10} chain, the substrate was removed from the reaction vessel, rinsed with dichloromethane and ethyl acetate, and dried under a stream of dry nitrogen. The substrate covered with adipic acid mono-(10-carboxy)-decyl ester was then exposed either to pyrenemethylamine and DCC (1:1) (to form pyrenemethylamide-10-decyl ester, P19) in dichloromethane or to pyrenemethylamine, hexadecylamine, and DCC (1:1:1) in dichloromethane for 0.5 h. The reacted substrate was removed from solution, rinsed with dichloromethane and ethyl acetate, and dried under a stream of nitrogen. The structures of these probes and diluents are shown in Figure 3.1.

Steady-State Emission Spectroscopy. Excitation and emission spectra were acquired with a Spex Fluorolog 3 spectrometer. The excitation wavelength was 320 nm with both the excitation and emission slits set to a 5 nm band-pass. Experiments were carried out in a nitrogen environment, and with monolayers immersed in cyclohexane, 1-pentanol, and water.

Time-Resolved Emission Measurements. Time-correlated single-photon counting (TCSPC) was used to study the lifetime and motional relaxation properties of the pyrene derivatives tethered to silica substrates. The TCSPC system used to acquire time-domain data has been described elsewhere[7] and is reviewed briefly here. The second harmonic of the output of a mode-locked CW Nd:YAG laser (Coherent Antares 76-S) is used to excite a cavity-dumped dye laser (Coherent 702-2) operated at 640 nm using Kiton Red laser dye (Exciton Chemical Co.). The output of the dye laser was typically 100 mW average power at 4 MHz repetition rate with ~5 ps pulses. The 320 nm light incident on the sample is generated by frequency doubling the dye laser output using a Type I $LiIO_3$

SHG crystal. The average optical power at the sample is less than 1 mW. The detection electronics are characterized by an instrument response function of 35 ps fwhm. The emission collection wavelength and polarization are computer controlled using National Instruments LabVIEW® v. 7.0 software.

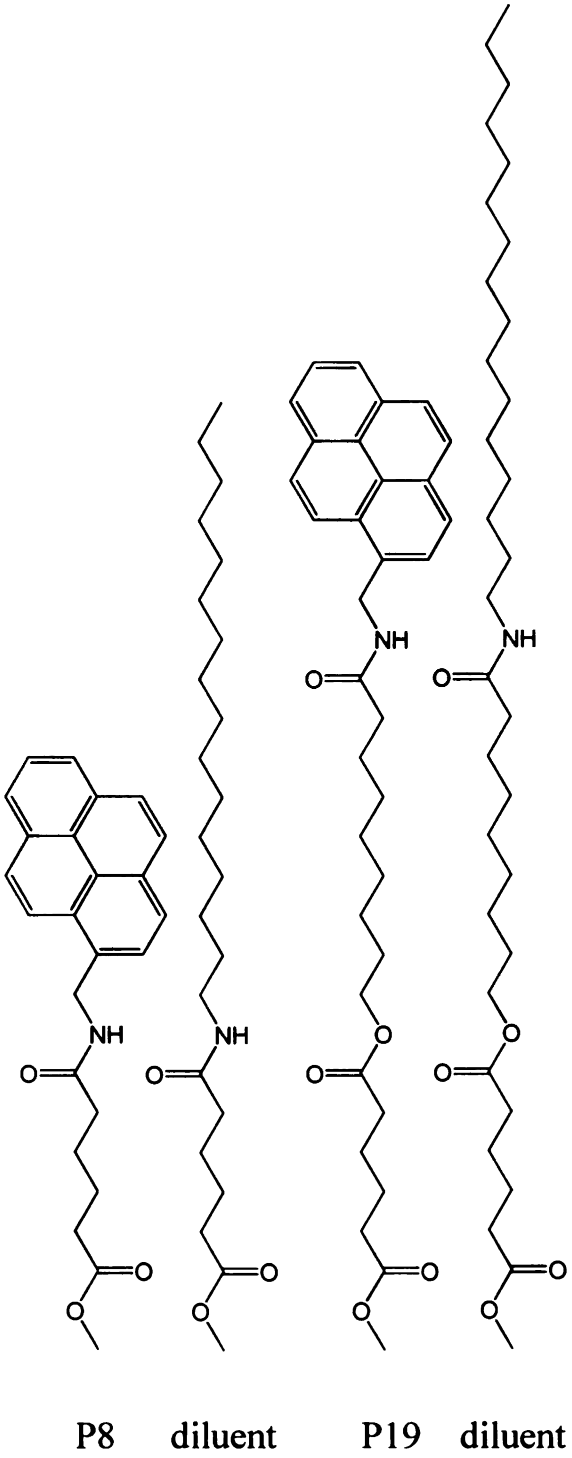

Figure 3.1 Structures of pyrene-terminated probes (P8, P19) and diluents used in the construction of monolayer structures reported in this work.

Results and Discussion

The spectroscopic characterization of monomolecular interfaces can pose a challenge because of the small number of molecules present. One way to interrogate interfaces with high sensitivity is to incorporate fluorescent chromophores into the interface and probe their optical response. We have investigated several tethered PAHs for this purpose and have found that there is a common pathway for oxidative degradation, resulting in the formation of quinones.[5,6] Pyrene is one PAH that we have made use of, not only to understand its photodegradation behavior, but also because the emission spectrum of pyrene is known to be sensitive to the "polarity" of its local environment.[8-17]

In this work, as in previous studies, we have used the same reaction chemistry to modify silica and ITO surfaces. While these surfaces are certainly not identical, their reactivities toward acid chlorides and other compounds such as $POCl_3$ are very similar. It is difficult to make direct comparisons between the resulting interfaces because they are not amenable to being probed by the same means. ITO can be interrogated electrochemically, but is characterized by a broad absorption band in the spectral range where PAHs absorb and emit. Thus the spectroscopic characterization of adlayers bound to ITO yields results that are contaminated by contributions from the conductive layer itself. Silica has ideal optical properties, but it is not addressable electrochemically, making direct comparison of these interfaces difficult. We can estimate from absorbance data that the surface PAH concentrations on these two materials are similar, and neither material exhibits mesoscopic crystallinity. These pieces of information suggest that, whatever the organization of the chromophores on these interfaces, it is likely similar, and it is on this basis that we detail the spectroscopic characterization of a series of pyrene derivatives tethered to silica.

The steady-state absorption and emission spectroscopy of pyrene is well established and understood. While the polarity sensitivity of pyrene is related closely to the symmetry of the chromophore, several previous studies have shown that substituents on the pyrene chromophore do not necessarily eliminate the polarity-sensitivity as long as the substituent is not conjugated to the ring system. We have found that tethered pyrene compounds can be used to gauge the polarity of their local environment when incorporated into monomolecular layers.[6]

The emission data for tethered pyrene derivatives provide information about the organization and polarity of these interfaces. We consider that there are two distinct bodies of information, time domain and frequency domain measurements, and we treat these datasets separately.

One of the more important properties of the pyrene chromophore is its ability to sense the "polarity" of its local environment through the ratio of two vibronic emission bands, designated I and III (Figure 3.2). This sensitivity is due to the relatively close energetic proximity of the pyrene S_1 and S_2 electronic states, and the fact that the $S_1 \leftarrow S_0$ and $S_2 \leftarrow S_0$ transitions are polarized nominally orthogonal to one another. The extent to which these two transitions are coupled is mediated by the dipolar interactions

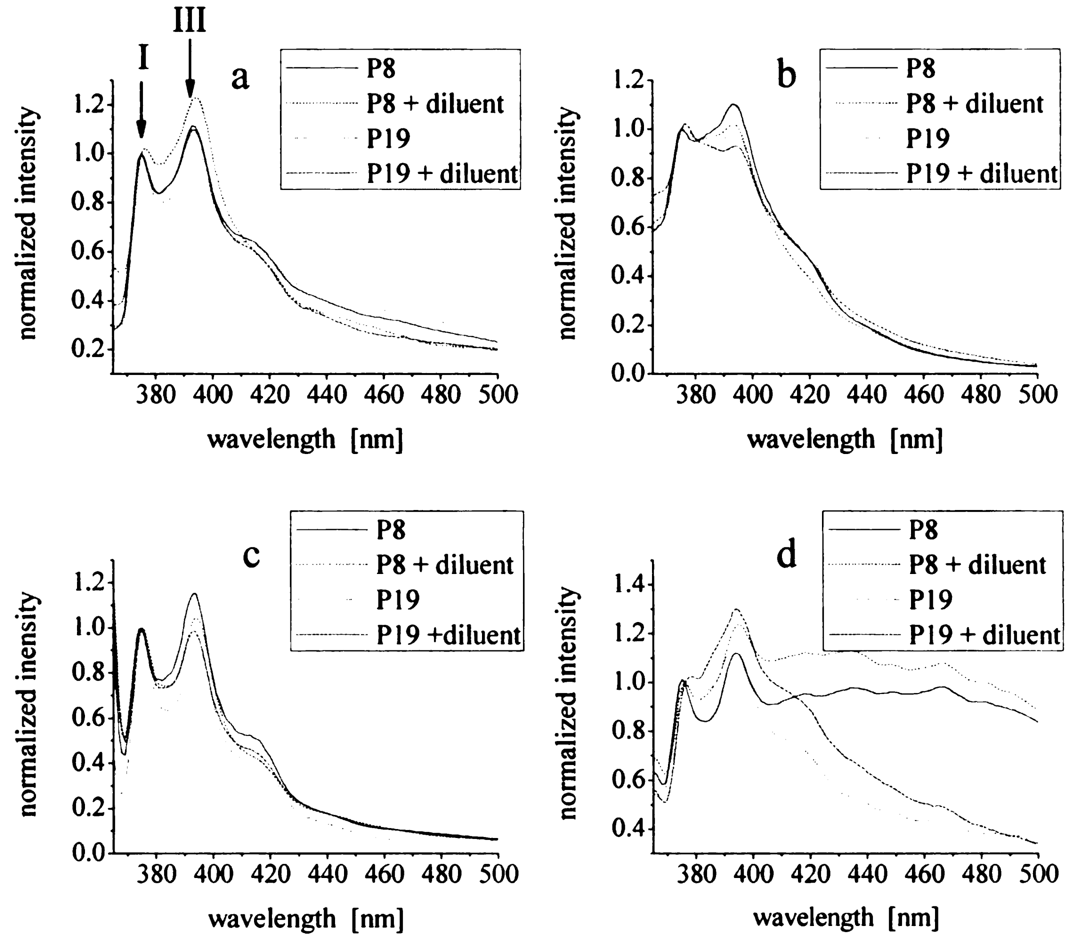

Figure 3.2 Steady state emission spectra of pyrene derivatives P8 and P19, with and without monolayer diluent, bound to silica surfaces. P8 (solid line), P8 with diluent (dashed line), P19 (dotted line), and P19 with diluent (dash and dotted line), on silica. Panel (a) is for interface immersed in cyclohexane, (b) immersed in 1-pentanol, (c) immersed in water, and (d) exposed to nitrogen gas. The I and III emission bands are indicated in (a).

between the chromophore to its immediate environment. For this transition coupling to be optimally sensitive to environmental polarity, the symmetry of the chromophore should be sufficiently high that the $S_2 \leftarrow S_0$ and $S_1 \leftarrow S_0$ electronic transition dipole moments are close to orthogonal. It has been shown in a variety of previous studies that the polarity sensitivity of pyrene is not compromised significantly upon substitution or tethering of the chromophore,[5,6,18] provided the substitution at the chromophore ring structure does not perturb the electronic state wavefunctions substantially. For the substituted pyrene derivatives we report here, we observe experimentally that these tethered chromophores do indeed retain their polarity-sensitivity, and we use this information to interrogate the chromophore local environment.

We show in Table 3.1 the pyrene I/III emission band ratios, a quantity related to environmental polarity, for pyrene in the solvents used here. We also show the I/III emission band ratios for the surface-bound derivatives in a nitrogen atmosphere and immersed in the solvents cyclohexane, 1-pentanol, and water. For solution phase pyrene, we obtain the expected polarity dependence, with the I/III band ratio being largest for water (most polar) and smallest for cyclohexane (least polar). For the tethered derivatives we observe the maximum I/III band ratios for immersion in 1-pentanol, and a decrease in I/III ratio for immersion in water. We note that P19 does not quite follow this trend, although it is apparently in a comparatively nonpolar environment. This outwardly surprising result can be understood in the context of the water overlayer causing the interfacial adlayer to "fold over" and become disorganized, with the pyrene chromophore seeking an environment that is relatively non-polar. For the amphiphilic solvent

Table 3.1 Steady-state band intensity ratios for surface-bound pyrene derivatives as a function of the solvent in which these interfaces are immersed.

medium	dipole moment (D)	dielectric constant ε_0	I/III band intensity ratios				
			pyrene[a]	P8	P8 + diluent	P19	P19 + diluent
nitrogen			-	0.68	0.78	0.74	0.79
cyclohexane	0.00	2.02	0.58	0.71	0.76	0.81	0.75
1-pentanol	1.65	13.9	1.02	1.01	1.27	1.06	1.25
water	1.85	78.5	1.87	0.95	1.03	1.09	0.94

[a] Experimental values for pyrene from Dong and Winnik treatment.[8]

1-pentanol, the interfacial species can be solvated effectively and the pyrene is thus exposed to the solvent to a greater extent than it is for the water overlayer. The cyclohexane data show similar I/III band ratios for the solution phase and surface-bound species, suggesting relatively effective solvation of the interface by this nonpolar solvent. Taken collectively, these data suggest that the presence of water above the interface gives rise to significant disorganization of the adlayer, and this finding is consistent with the time-domain emission data that we consider next.

The time-resolved emission response of pyrene and its derivatives has been studied extensively, and some preparatory discussion of these data is in order before we consider the information they contain in detail. For the native chromophore, the dominant excitation is for the $S_2 \leftarrow S_0$ transition and the primary emission is from the S_1 state. These states are polarized orthogonal to one another, leading to negative anisotropy values. For substituted pyrene derivatives, the addition of some chemical functionality to the pyrene ring structure perturbs the electronic states to an extent that depends on the identity of the substitution. In some cases this perturbation leads to the two electronic states being polarized at an angle less than 54.7° with respect to one another, and it other cases, the polarization difference between the two states remains at a value greater than 54.7°. Accordingly, some tethered pyrene moieties yield positive anisotropy data and other derivatives yield negative anisotropy data.[19-22] The prediction of whether or not a negative anisotropy will be observed for a given pyrene derivative is not feasible at the present time, but computational studies are underway to address this issue. For the substituted pyrene derivatives we use in this work, we observe a positive anisotropy signal.

The second point that needs to be considered is the fluorescence lifetime of pyrene derivatives. Pyrene is quenched efficiently by oxygen, and thus it is not readily possible to infer environmental information from lifetime measurements unless the samples used are rigorously deoxygenated. We have not performed this step in the work we report here and thus we do not try to interpret the lifetime data in terms of specific molecular-scale interactions. Rather, we consider that the number of recovered lifetimes is indicative of a variety of environments in which the pyrene chromophore resides. In most cases, we recover two lifetime components for the tethered pyrene derivatives (Table 3.2), with the characteristic short lifetime being on the order of a nanosecond or less, and the long lifetime being on the order of several nanoseconds, with considerable uncertainty attending the determination of these longer lifetimes. In contrast, for solution phase pyrene, previous work has shown that lifetimes on the order of 300 – 400 ns are obtained under oxygen-free conditions and 6 – 8 ns lifetimes are seen for ambient oxygen concentrations in different solvents. All of our lifetimes are short by comparison and the primary conclusion we can draw from these data is that the chromophore is distributed among at least two local environments in these interfaces. For the systems we report on here, we recover predominantly two-component lifetimes, suggesting the existence of more than one environment for the pyrene chromophores within a given monolayer (Figure 3.3). For the few cases exhibiting apparently single-exponential decays, we believe these results to be due to the limited signal/noise ratio of the data. The primary

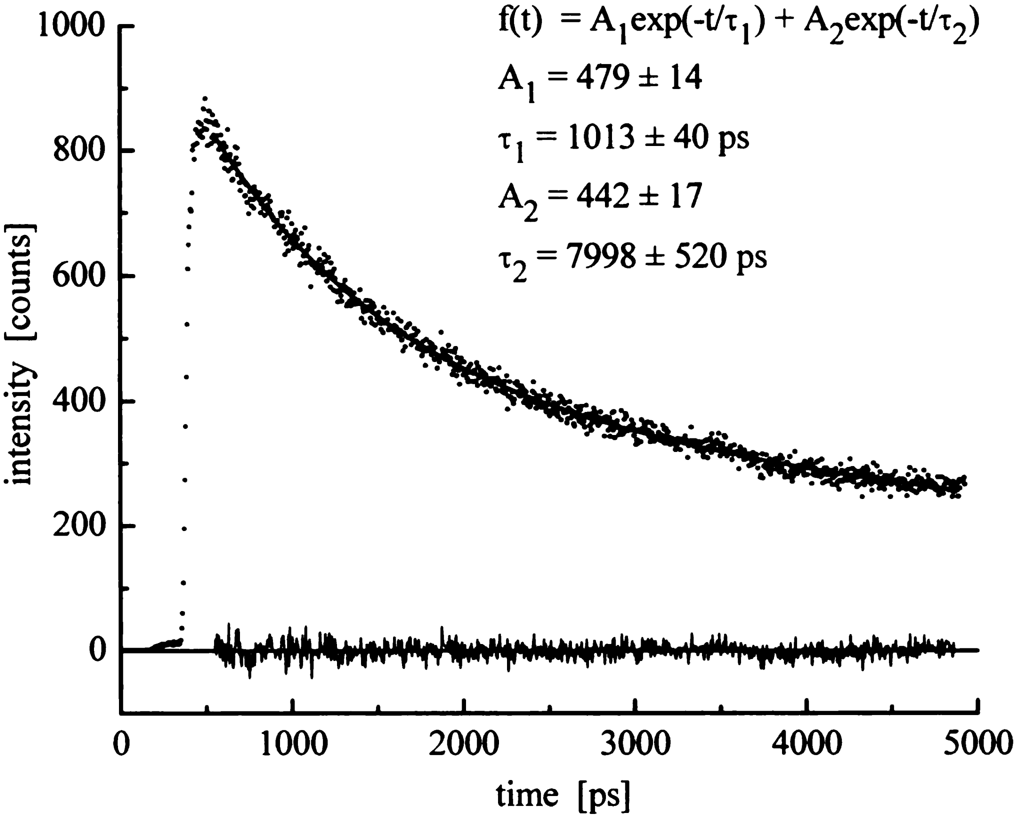

Figure 3.3 Fluorescence lifetime data for P8 bound to silica and immersed in 1-pentanol. These data are representative of the lifetime data for P8 and P19, with results of fits to the data shown in Table 3.2. Residuals show agreement of the fit to a two-component exponential decay.

Table 3.2 Summary of time-resolved data for P8 and P19 on silica.

medium		monolayer composition			
		P8	P8 + diluent	P19	P19 + diluent
air	τ_{fl} [ps]	152±4, 1127±17	1028±13	441±36, 1883±177	338±54, 2022±111
	τ_{HR} [ps]	224±49	174±30	--	--
	$r(0)$	0.12±0.02	0.30±0.04	0.03±0.01	0
	$r(\infty)$	0.02±0.01	0.21±0.01	0.03±0.01	0
water	τ_{fl} [ps]	785±30, 4842±650	882±18, 9028±4043	972±88	786±122, 3401±1370
	τ_{HR} [ps]	81±25	∞ (314±326)	--	--
	$r(0)$	0.11±0.02	0.03±0.02	0	0
	$r(\infty)$	0.08±0.01	0.02±0.01	0	0
pentanol	τ_{fl} [ps]	1013±40, 7998±520	816±60, 5086±359	1244±93, 16500±5000	997±287, 6264±3286
	τ_{HR} [ps]	453±13	537±30	397±24	--
	$r(0)$	0.20±0.01	0.22±0.01	0.24±0.01	0.05±0.01
	$r(\infty)$	0.03±0.01	0.04±0.01	0.04±0.01	0.05±0.01
cyclohexane	τ_{fl} [ps]	449±23, 2611±126	392±28, 2817±130	200±7, 2418±62	786±142, 4834±1605
	τ_{HR} [ps]	71±42	319±67	--	--
	$r(0)$	0.10±0.04	0.21±0.03	0.09±0.01	0.10±0.01
	$r(\infty)$	0.03±0.01	0.11±0.01	0.09±0.01	0.10±0.01

value of the lifetime data lies in its ability to reveal the existence of a structurally heterogeneous environment for the pyrene chromophores.

We turn at this point to a discussion of the anisotropy data for tethered pyrene, because these data contain information on the local environment that is interpretable in a straightforward manner. We show in Table 3.2 the quantities τ, $r(0)$ and $r(\infty)$. These quantities are related to the experimental time-resolved intensity data $I_{\|}(t)$ and $I_{\perp}(t)$ through the following series of equations:

$$\begin{aligned} r(t) &= \frac{I_{\|}(t) - I_{\perp}(t)}{I_{\|}(t) + 2I_{\perp}(t)} \\ r(t) &= r(\infty) + (r(0) - r(\infty))\exp\left(-t/\tau_{HR}\right) \qquad (3.1) \\ \tau_{HR} &= \frac{7\theta_0^2}{24D_W} \end{aligned}$$

The quantities $r(0)$ and $r(\infty)$ are the zero-time and infinite-time anisotropies, D_W is the "wobbling" diffusion coefficient, representing motion of the chromophore about its tether within a cone of semi-angle θ_0.[23] The infinite time anisotropy is related to the average organization or extent of motional restriction experienced by the chromophore within its environment, and $r(0)$ is determined by the angle between the excited and emitting chromophore transition dipole moments. The quantities of most interest to the organization of the interfacial structures are $r(\infty)$ and τ_{HR}. We consider the time-domain dynamical data for P8 and P19 separately.

The $r(\infty)$ results for the interfaces containing P8 show that, in all cases, the interface is substantially disorganized, with $r(\infty)$ values ranging from 0.02 to 0.08. For P8 coadsorbed with longer organic adlayer species, we find that there is a significantly smaller orientational distribution in air and cyclohexane, with $r(\infty)$ values for pentanol and water being consistent with a relatively disorganized interface (Table 3.2). For all of these measurements, save for P8 buried in an aliphatic environment, we see a decay of the induced anisotropy and thus are able to report a value of τ_{HR}. While it may be tempting to evaluate this quantity as we would for free rotor reorientation times, we cannot do so because of the dependence of τ_{HR} on both D_W and θ_0. Combining these data with the $r(\infty)$ results, which address the limits that can be placed on θ_0, we see that the local chromophore environment can indeed place some motional restrictions on D_W. We know from the hindered rotor model that

$$r(\infty) = r(0)\left\langle P_2(\cos\theta)\right\rangle^2 \tag{3.2}$$

and we can extract the quantities $r(\infty)$ and $r(0)$ from the experimental data (Figure 3.4). It is thus possible to extract information on θ. If we assume that $\theta \approx \theta_0$ at long times, we can use these data to provide information on both D_W and the intrinsic disorder in the films (Table 3.3).

Before considering the interesting trends shown in Table 3.3, we need to be specific about the meanings of the quantities θ and D_W. The entries marked " - " in

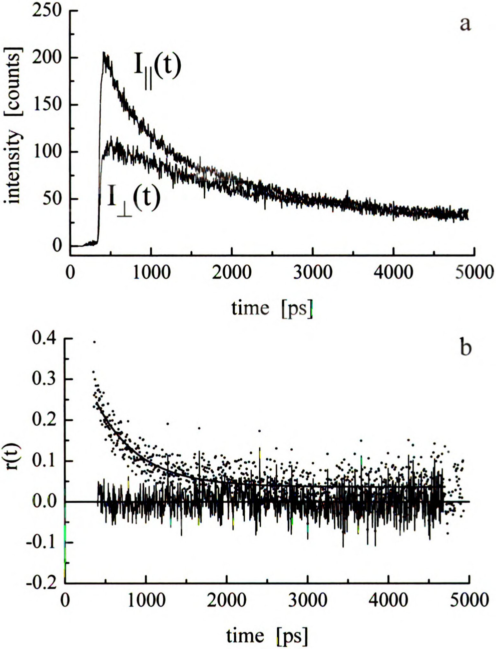

Figure 3.4 (a) Time resolved emission intensities for emission polarizations parallel and perpendicular to the (vertical) excitation polarization for P8 + diluent bound to silica and immersed in 1-pentanol. (b) Induced orientational anisotropy function constructed from data shown in (a). The fit to the data and residuals are also shown.

Table 3.3 Results calculated for hindered rotor model based on experimental $r(0)$, $r(\infty)$ and τ_{HR} data.

medium		monolayer composition			
		P8	P8 + diluent	P19	P19 + diluent
air	θ [deg.]	39 ± 9	19 ± 4	--	--
	D_W [MHz]	600 (+1160, -310)	180 (+150, -100)	--	--
water	θ [deg.]	18 ± 7	20 ± 17	--	--
	D_W [MHz]	360 (+630, -260)	--	--	--
pentanol	θ [deg.]	40 ± 3	38 ± 3	39 ± 3	--
	D_W [MHz]	310 (+60, -50)	240 ± 50	340 (+80, -70)	--
cyclohexane	θ [deg.]	33 ± 21	25 ± 4	--	--
	D_W [MHz]	1360 (+7500, -1250)	170 (+120, -70)	--	--

Table 3.3 correspond to the absence of detectable decay dynamics.[22] This limit represents the absence of free volume in which the chromophore can move ($D_W \rightarrow 0$), but does not provide direct information on the tilt angle of the pyrene. It is the value of $r(\infty)$ that is related to average tilt angle. The θ values in Table 3.3 are related to the free volume which the chromophore can access, and D_W is a measure of how rapidly the pyrene moiety is moving (rotating, wobbling) within that free volume.

We note from Table 3.3 that, in general, the P8 chromophores are characterized by much more motional freedom than the P19 chromophores. We attribute this freedom of motion for the shorter tethered pyrene moiety to the lower propensity of this shorter molecule for associating with its neighbors by means of H-bonding or van der Waals interactions. For P19, the greater length of the tethering chain could give rise to either stronger intermolecular van der Waals interactions if the molecules are in sufficiently close proximity, or the longer chains could allow for enough degrees of freedom to make chromophore π–π interactions more efficient. We believe this latter explanation is not operative because of the absence of significant excimer signal in the steady state emission data.

For the P8 chromophore, we observe that, while the cone angle θ is qualitatively similar for all interfaces immersed in solvent, the D_W terms are significantly slower in the monolayer containing aliphatic diluent molecules. This finding can be understood in the context of the diluent providing a viscous environment in which the chromophore groups move, and the relationship between local viscosity and motional relaxation time is well established.[24] For P8 monolayers without diluent, there are presumably fewer neighbor molecules to impede the motional relaxation of the pyrene group.

The P8 chromophore also exhibits a significant solvent dependence to its relaxation dynamics. These dynamics do not scale simply with solvent viscosity, and this finding provides insight into the nature of solvent-monolayer interactions. For P8 in air, we recover a value of D_W that is intermediate between water and cyclohexane. For P8 without diluent, the monolayer structure appears to be solvated efficiently by cyclohexane, presumably because of that solvent's ability to provide a nonpolar environment in which the pyrene can rotate. In air, the pyrene chromophore layer will either interact with its neighbors or the substrate, and such interactions would likely provide an environment which will impede the motion of the pyrene ring system more than the presence of a low viscosity nonpolar solvent. Water and pentanol solvent overlayers give rise to the lowest D_W values for the P8 monolayer. We speculate that the relatively polar solvents cause the nonpolar pyrene to interact most strongly with its neighbors or the substrate, in effect creating a reasonably viscous environment.

For the monolayers containing P8 + diluent, we observe some variation in θ but the values of D_W are solvent independent to within the experimental uncertainty. The implication of these data is clear that the diluent is providing an aliphatic environment in which the pyrene can reside and that in this environment the chromophore is substantially isolated from the influence of the solvent overlayers. We note also that the only P19 monolayer to exhibit measurable dynamics is the monolayer/pentanol system, and the results we extract are indistinguishable from the P8 data in pentanol. Based on this finding, it is also possible that the amphiphilic pentanol solvent provides essentially the same solvation environment for all of these monolayers, and the resulting dynamics turn out to be similar to the P8 + diluent dynamics because the effective viscosity of the diluent environment is similar to that of pentanol. This is admittedly a speculative explanation, but it is consistent with the experimental data. The absence of dynamics in the P19 + diluent monolayer immersed in pentanol is likely the result of the length of the aliphatic diluent precluding solvent access to the pyrene chromophore.

Conclusions

The broad picture that emerges from our emission data is that, for chromophores bound very close to the substrate surface, their environment could be expected to be relatively rigid because of covalent bonding and limited orientational degrees of freedom. This effect is compensated by the relatively smaller number of attractive interactions with neighboring molecules, and the net result is that we observe somewhat constrained molecular motion for P8, both by itself and with the addition of a diluent. The longer P19 molecule is characterized by less motion, consistent with the dominant influence of neighbor-neighbor intermolecular interactions. The exposure of these monolayers to solvents has a significant effect for P8 by itself, demonstrating the interplay between solvent and monolayer constituents, sometimes acting to solvate the monolayer constituents and at other times serving to force a molecular-scale phase separation at the interface. When P8 is surrounded by aliphatic diluent, we observe that the behavior of this chromophore is dominated by the diluent and influenced to a much lower extent by the presence of the solvent. We have speculated that the amphiphilic solvent pentanol can in fact solvate the P8 + diluent and P19 monolayers, and that the viscosity of the resulting monolayer environment is characterized by a viscosity that is on the same order as that of pentanol (> 3 cP). When these data are viewed in the context of the electrochemical information presented in the preceding paper, it is clear that any permeability of the monolayer is characterized by mesoscopic features and not by molecular-scale penetration of solution phase molecules. The comparative disorganization of the monolayers found with the electrochemical experiments is not inconsistent with the spectroscopic data. Our θ and D_W findings suggest that the amount of motional freedom available to the pyrene moiety depends on a number of structural factors but in all cases it is relatively limited. The basis for this limited freedom is likely the solvent-monolayer interactions forcing the monolayer into a comparatively tightly packed conformation. We are presently investigating the properties of these systems in greater detail to provide insight into what structural controls can be exerted to mediate interactions between monolayers and solvent overlayers.

Literature Cited

(1) Dominska, M.; Jackowska, K.; Krysinski, P.; Blanchard, G. J. *Journal of Physical Chemistry B* **2005**, *109*, 15812-15821.

(2) Major, J. S.; Blanchard, G. J. *Langmuir* **2002**, *18*, 6548-6553.

(3) Major, J. S.; Blanchard, G. J. *Langmuir* **2003**, *19*, 2267-2274.

(4) Chance, R. R.; Prock, A.; Silbey, R. *Advances in Chemical Physics* **1978**, *37*, 1-65.

(5) Mazur, M.; Blanchard, G. J. *Journal of Physical Chemistry B* **2004**, *108*, 1038-1045.

(6) Mazur, M.; Blanchard, G. J. *Journal of Physical Chemistry B* **2005**, *109*, 4076-4083.

(7) DeWitt, L.; Blanchard, G. J.; LeGoff, E.; Benz, M. E.; Liao, J. H.; Kanatzidis, M. G. *Journal of the American Chemical Society* **1993**, *115*, 12158-64.

(8) Dong, D. C.; Winnik, M. A. *Photochemistry and Photobiology* **1982**, *35*, 17-21.

(9) Dong, D. C.; Winnik, M. A. *Canadian Journal of Chemistry* **1984**, *62*, 2560-5.

(10) Carr, J. W.; Harris, J. M. *Analytical Chemistry* **1986**, *58*, 626-31.

(11) Carr, J. W.; Harris, J. M. *Journal of Chromatography* **1989**, *481*, 135-46.

(12) Bogar, R. G.; Thomas, J. C.; Callis, J. B. *Analytical Chemistry* **1984**, *56*, 1080-4.

(13) Wistus, E.; Mukhtar, E.; Almgren, M.; Lindquist, S. E. *Langmuir* **1992**, *8*, 1366-71.

(14) Liu, Y. S.; Ware, W. R. *Journal of Physical Chemistry* **1993**, *97*, 5980-6.

(15) Liu, Y. S.; de Mayo, P.; Ware, W. R. *Journal of Physical Chemistry* **1993**, *97*, 5987-94.

(16) Liu, Y. S.; de Mayo, P.; Ware, W. R. *Journal of Physical Chemistry* **1993**, *97*, 5995-6001.

(17) Karpovich, D. S.; Blanchard, G. J. *Journal of Physical Chemistry* **1995**, *99*, 3951-8.

(18) Tulock, J. J.; Blanchard, G. J. *Journal of Physical Chemistry A* **2000**, *104*, 8341-8346.

(19) Tulock, J. J.; Blanchard, G. J. *Journal of Physical Chemistry B* **2002**, *106*, 3568-3575.

(20) Krysinski, P.; Blanchard, G. J. *Langmuir* **2003**, *19*, 3875-3882.

(21) Kelepouris, L.; Krysinski, P.; Blanchard, G. J. *Journal of Physical Chemistry B* **2003**, *107*, 4100-4106.

(22) Karpovich, D. S.; Blanchard, G. J. *Langmuir* **1996**, *12*, 5522-5524.

(23) Lipari, G.; Szabo, A. *Biophysical Journal* **1980**, *30*, 489-506.

(24) Debye, P. *Polar Molecules*.

CHAPTER 4

INTERROGATING INTERFACIAL ORGANIZATION IN PLANAR BILAYER STRUCTURES

Introduction

The development of selective chemical and biological sensing devices has been a topic of extensive research interest because of their potential importance. Biologically active components such as transmembrane proteins, nucleic acids, and antibodies are used in biosensing devices due to their intrinsic ability to perform molecular or biological recognition functions. For a biosensing device, there must be a biologically active component that is connected in some manner to a transducer such that the chemical change associated with molecular recognition can be converted into a quantifiable signal. The sensing components must maintain their functional activity while attached to the transducer, a condition that can be difficult to achieve. Most biomolecules lose their biological activity when not in their native environment, and one widely attempted means of maintaining bioactivity is to create an environment on a transducer surface that mimics the native environment of the biomolecule.[1-7] Supported lipid bilayers are a commonly used chemical structure for this purpose,[8-10] but there remain many open questions relating to the design and fabrication of biomimetic bilayers owing to their fluidity and compositional complexity. We are interested in understanding the organization of model lipid and hybrid bilayer systems, with the goal of using this knowledge to make comparatively simple bilayer structures that are capable of supporting biomolecules in their active form(s).

The organization of lipids and proteins in biological lipid membranes was described as a fluid mosaic,[11] but more recent work point to a complex, heterogeneous structure. Any interfacial system we design to host transmembrane proteins or other biomolecules must be characterized by fluid and compositional properties similar to those of a cell wall, and the central issue is determining the critical bilayer properties required for this purpose. The most pressing issues in the investigation of supported bilayers are their fluidity (top vs. bottom leaflet) and how composition is related to both fluidity and structural heterogeneity. At heart is the construction of the compositionally simplest biomimetic bilayer capable of supporting biomolecules in their active forms, and understanding the relationship between bilayer composition and dynamics is our starting point. We have focused on interactions between the bilayer constituent molecules over nm length scales. The studies we report on here focus on the bilayers themselves, without the incorporation of proteins. Before we introduce biomolecules into the artificial lipid membranes for sensing purposes, we need to better understand the properties of the bilayer structure.

To aid in this examination, we want to start with a relatively well organized and compositionally simple system. It is important to have a membrane free of defects for the eventual electrochemical characterization of incorporated biomolecules. For chemical sensing applications, the matrix that serves as the host has to be sufficiently fluid to accommodate the presence of a biomolecule, and from a compositional standpoint, the bilayer has to have the requisite constituents to support the biomolecule(s) in their active form(s). These requirements place multiple constraints on the bilayer, and it is important to examine the organization of the bilayer bottom leaflet as well as the full bilayer. To examine these monolayers and bilayers, we have utilized several techniques to obtain information on the organization of the interface over a variety of length scales. Information that is averaged over macroscopic length scales, such as ellipsometric thickness, is very useful in terms of determining the extent of bilayer formation and organization of the bilayer as a whole. Contact angle measurements likewise provide information on the presence and, to some extent organization, of the bilayers, and infrared spectroscopic data provide useful information on the extent of order and crystallinity within the nonpolar regions of the bilayer. Probing the system electrochemically provides additional detail about the kinetics of electron transfer processes across the bilayer interface, and how it changes with the structure and organization of the interface. Probing this interface with redox active species present in the electrolyte solution yields information on the permeability of this interface to small ions. This information is especially important if we want to study selectively the signal from redox probes of interest or biomolecules located within the interior of an interface. Time-resolved fluorescence spectroscopy provides information on local organization of bilayer molecules surrounding the chromophores. Information from these techniques, taken collectively, provides a picture of the molecular scale organization of the bilayer constituents.

We have used tethered pyrene as a spectroscopic and electrochemical probe to examine the organization of selected biomimetic bilayer interfacial structures. Pyrene has been shown to be useful both for fluorescence dynamical experiments and for studies of electron transfer in interfacial systems. The steady state and time-resolved fluorescence behavior of pyrene is well understood, and the sensitivity of pyrene to the polarity of its local environment has been used widely to interrogate interfacial and bulk systems.[12-16] The electrochemical properties of tethered pyrene have been characterized in recent years as well.[17,18] Tethering this probe to the transducer surface at different distances can be used to study the redox reaction kinetics and thereby deduce the properties of the probe's local environment. These kinetic data point to limited access of the tethered probe to the overlayer and/or very slow electron transfer between the probe and the electrode. Fluorescence lifetime data are consistent with the kinetic results and indicate that the immediate environment of the tethered probe mediates the access of oxygen to the probe.

Experimental

Chemicals. 1-Pyrenedecanoic acid (≥ 98%), and arachidic acid (≥99%) were obtained from Fluka. 1-Pyrenehexadecanoic acid was obtained from Molecular Probes, Inc. 1,2-Dipalmitoyl-*sn*-glycero-3-phosphocholine (DPPC) (≥99%), 1-octadecanethiol (98%), perchloric acid (70%), sulfuric acid (99.999%), lithium perchlorate (99.99%), potassium ferrocyanide (II) trihydrate (99%), hexaammineruthenium (III) chloride (98%), and gold foil (99.99%) were obtained from Sigma-Aldrich. Chloroform (HPLC grade) was obtained from OmniSolv. Aqueous solutions and the aqueous subphase in Langmuir-Blodgett trough were prepared from Milli-Q water.

Gold and quartz substrate preparation. Gold coated silica substrates (200 nm of Au sputtered on 20 nm of Cr on Si wafers) were cleaned in a UV cleaner for 10 min and stored in Milli-Q water prior to modification. Gold foil and quartz substrates were cleaned in piranha solution for 20 min (3:1 concentrated H_2SO_4 : 30% H_2O_2). *Caution! Piranha solutions react violently with organic matter and should be handled with extreme care!* The clean substrates were then rinsed with Milli-Q water and dried under a stream of dry nitrogen. The gold foil was then cleaned electrochemically in 0.5 M H_2SO_4 (scan rate 100 mV/s, potential range from -300 to 1700 mV vs. Ag|AgCl reference electrode) until reproducible cyclic voltammograms were obtained. The gold foil was then rinsed with Milli-Q water and dried under nitrogen. The working area of the gold electrode was estimated from cyclic voltammetry using $[Ru(NH_3)_6]Cl_3$ as a redox probe.

Langmuir films. Langmuir films were obtained using a computer-controlled Langmuir-Blodgett trough (model 612D, NIMA Technology Ltd). The Langmuir films were obtained at room temperature (21 °C) on a water subphase. The first layer of the interface was transferred to the solid substrate using the Langmuir-Blodgett method,[19,20] where the hydrophilic substrate was initially immersed in the water subphase (Figure 4.1a) prior to the spreading of the Langmuir layer. A volume of 40 µL of 2 mg/mL solution of arachidic acid, octadecanethiol, and pyrenedecanoic or pyrenehexadecanoic acid (3:3:1 molar ratio) in chloroform was then spread on the water subphase and evaporation of the chloroform was complete after 10 min. The molecules on the subphase surface were compressed to the solid phase state (surface pressure 20 mN/m) and the substrate was then drawn vertically at constant pressure of 20 mN/m. The resulting monolayer was dried under nitrogen for at least 3 h. To transfer the second lipid leaflet onto the substrate, a volume of 40 µL of 2mg/mL DPPC solution in chloroform was spread onto the water subphase and the chloroform was allowed to evaporate for 10 min. The surface layer was next compressed to a surface pressure of 45 mN/m and the monolayer was transferred onto the substrate horizontally according to the method developed by Langmuir and Schaefer[21] (Figure 4.1b). The resulting bilayer was allowed to dry under nitrogen for at least 3 h.

Ellipsometry. Film thickness was measured using a multiwavelength ellipsometer (J. A. Woollam Co., Inc.) with a 75 W xenon lamp source. The electric field incidence angle is 75° with respect to the sample surface normal, and the refractive index of the film assumed to be 1.5. The measured thickness of the monolayer was 20 ± 4 Å (pyrenedecanoic acid), and 24 ± 5 Å (pyrenehexadecanoic acid). The thickness of the

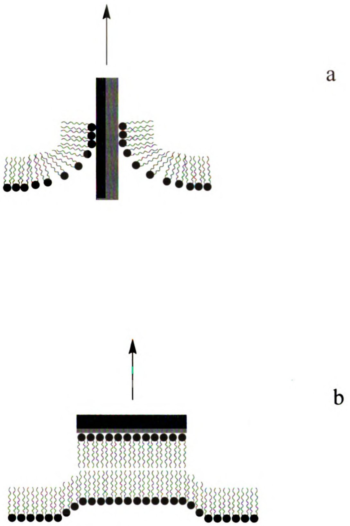

Figure 4.1 (a) Scheme of preparation of the Langmuir-Blodgett monolayer on hydrophilic substrate by withdrawing the substrate from the subphase. (b) Scheme of preparation of the bilayer using Langmuir-Schaefer method (horizontal touch).

bilayer was measured to be 57 ± 7 Å (pyrenedecanoic acid), and 68 ± 3 Å (pyrenehexadecanoic acid). A monolayer of DPPC on gold was measured to be 35 ± 2 Å. The uncertainties in the data presented are for at least three individual determinations.

FT-IR Spectroscopy. Reflectance FT-IR spectra of modified gold substrates were collected using an FT-IR spectrometer (Nicolet, Magna-IR 560) equipped with a Pike grazing angle (80°) attachment. The spectral resolution was set to 2 cm^{-1} for these measurements.

Contact Angle. Water contact angles were measured using a Video Contact Angle System 2000 (AST Products, Inc.). We obtained a contact angle of 94° ± 2° for a monolayer containing pyrenedecanoic acid, and 97° ± 1° for a monolayer containing pyrenehexadecanoic acid. For bilayer structures we recovered a contact angle of 48° ± 6°. We consider the chemical significance of these data below.

Electrochemistry. Electrochemical experiments were performed using a computer-controlled electrochemical analyzer (CH Instruments Model 650) operating with a three electrode cell. All potentials are referenced to Ag | AgCl | 3M KCl (-52 mV vs. SCE), used as the reference electrode. Platinum wire served as a counter electrode. Experiments were carried out in aqueous 0.1 M $HClO_4$. 1 mM $K_4[Fe(CN)_6]$, and $[Ru(NH_3)_6]Cl_3$ in 0.1 M $LiClO_4$ were used in studying the integrity of LB films.[22] A solution of 1 mM $[Ru(NH_3)_6]Cl_3$ in 0.1 M $LiClO_4$ was also used to estimate the working electrode surface area.

Time-Resolved Emission Measurements. A time-correlated single-photon counting (TCSPC) instrument was used to study the lifetime and anisotropy decay dynamics of tethered pyrene in monolayers and bilayers on quartz substrates. The experiments were carried out at room temperature and in the presence of atmospheric oxygen. This spectrometer has been described in detail elsewhere[23] and we recap its salient features here. The source laser is a mode-locked continuous wave Nd:YAG laser (Coherent Antares 76-S) that produces ~30 W average power at 1064 nm with 100 ps pulses at a repetition rate of ca. 76 MHz. The second harmonic of the output of this laser (~2W average power, 100 ps pulses, 76 MHz repetition rate) is used to excite a cavity-dumped dye laser (Coherent 702-2) operating at 640 nm using Rhodamine 6G dye (Kodak, Eastman Fine Chemicals). The dye laser produced 5 ps pulses with average power of ~100 mW at a 3.8 MHz repetition rate. The 320 nm light used to excite the sample is generated by frequency doubling the dye laser output using a Type I KDP SHG crystal. The average power of UV light on the sample is less than 1 mW. The fluorescence detector is a Hamamatsu R3809U microchannel plate PMT and the instrument response time is ca. 35 ps. The emission collection wavelength and polarization are computer controlled using National Instruments LabVIEW® v. 7.0 software.

Results and Discussion

The primary purpose of this work is to evaluate the organization of bilayer structures formed using Langmuir-Blodgett and Langmuir-Schaefer technology and to understand whether or not the organization of the bilayer itself can mediate the dynamics and electron transfer properties of species contained within these structures. In addition to addressing these issues, which are of potential importance to trans-membrane signaling and leakage processes, we are also concerned with utilizing these and similar structures as biomimetic systems, and as such it is important to understand the role of a probe species contained within the bilayer.

In this work we have used Langmuir-Blodgett and Langmuir-Schaefer methods to deposit planar lipid bilayers on gold and quartz substrates. We have chosen these substrates for their utility as electrodes for electrochemical experiments and as optically transparent supports for spectroscopic measurements, respectively. For these bilayers, the bottom leaflet was composed of arachidic acid, octadecanethiol, and either pyrenedecanoic (Py10) or pyrenehexadecanoic (Py16) acid, in a 3:3:1 molar ratio (Figure 4.2). The thiol was used to provide stable attachment of the layer to the gold electrode and it was also used for layers formed on quartz for the sake of compositional consistency. We have used different pyrene tether lengths to evaluate how the electrochemical and spectroscopic signals from the pyrene moiety vary with distance from the solid substrate. We expect the functional form of the pyrene tether length dependence to be different for the electrochemical and spectroscopic measurements, and we are also aware that the pyrene moiety can itself act as a perturbation to the layer structure. For all of our measurements, the top leaflet of the bilayer we deposit on our

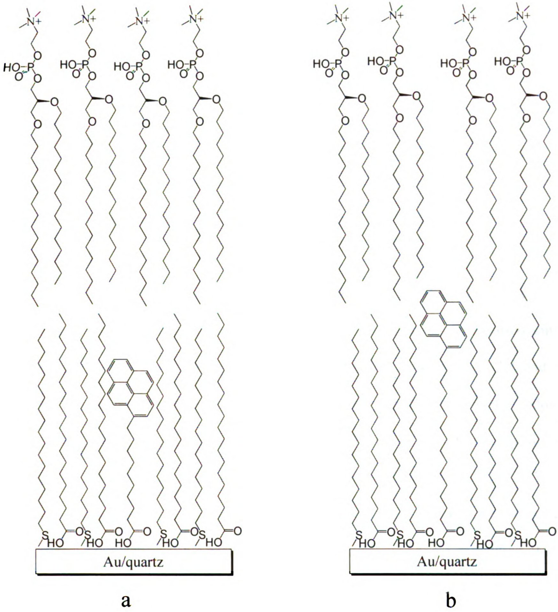

Figure 4.2 Scheme of bilayers containing tethered pyrene ((a) pyrenedecanoic acid, and (b) pyrenehexadecanoic acid) reported in this work. The structures identical are not intended to reflect the actual conformation of the interfacial constituents.

planar substrates was composed of the phospholipid DPPC with no additives.

Cyclic Voltammetry. We consider the electrochemical response of the tethered pyrene moiety first. The electrochemistry of this molecule has been reported elsewhere, and is well understood.[17,18] We show in Figure 4.3 the first three cycles in the cyclic voltammograms of tethered pyrene in monolayers and bilayers on gold. We assume here that thiols react with gold so that they stabilize the monolayer by virtue of their attachment to the substrate. For both pyrenedecanoic acid (Py10) and pyrenehexadecanoic acid (Py16), the first anodic scan reveals irreversible oxidation of the pyrene moiety at ca. 1 V, to form an unstable radical cation which, in a subsequent cathodic scan forms a more stable pyrenediol. The reversible peaks between 200 and 300 mV, seen in scans two and three, are associated with the pyrenedione/pyrenediol redox couple. The peaks, seen at 260 mV for both Py10 and Py16, shift toward more positive potentials with the addition of the DPPC lipid adlayer, producing maxima at 275 mV for Py10 and 290 mV for Py16. These shifts are analogous to those reported previously in the literature for different redox probes and have been attributed to a combination of local solvation effects on the redox species potential and the double layer effect, where the redox potential was shifted to more positive values due to a net charge separation between the redox species buried within a film and their charge-compensating ions present in the solution.[24,25] The pyrenedione/pyrenediol couple undergoes a $2e^-/2H^+$ reaction, requiring the presence of protons to proceed. The screening of the pyrenedione/pyrenediol by the DPPC overlayer limits proton access resulting in a positive shift of peak potential for bilayers compared to monolayers. The screening effect

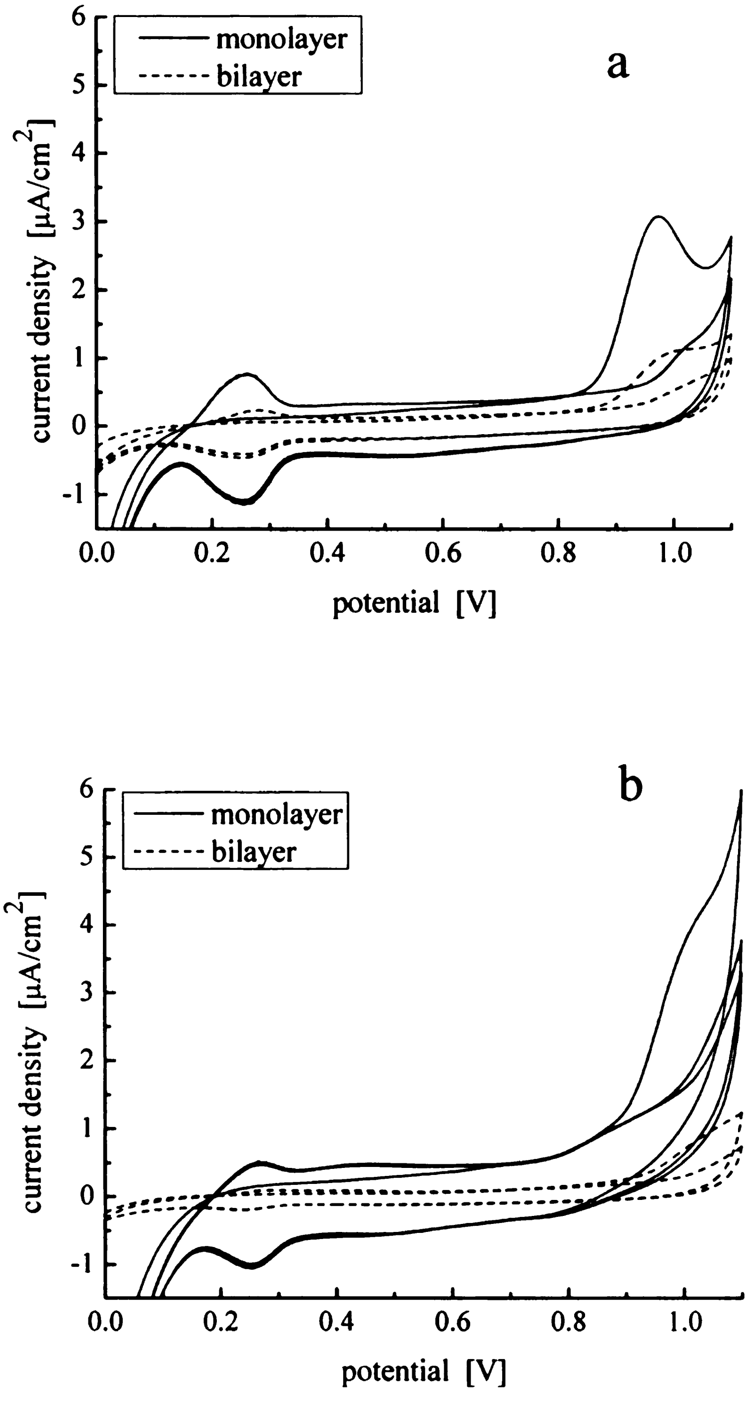

Figure 4.3 Cyclic voltammograms of (a) pyrenedecanoic acid and (b) pyrenehexadecanoic acid in monolayers and bilayers on gold in 0.1 M $HClO_4$. The scan rate is 20 mV/s.

can also be seen in the amount of pyrene moieties undergoing redox reaction. The loading density of pyrene derivatives is constant for both mono- and bilayers and can be estimated from the isotherms obtained during the Langmuir-Blodgett deposition. The surface area per molecule from the measured isotherms (data not shown) are ca. 20 $Å^2$ for arachidic acid, 22 $Å^2$ for octadecanethiol, 25 $Å^2$ for pyrenedecanoic acid, and 39 $Å^2$ for pyrene hexadecanoic acid. Based on this information we calculated the number of moles of pyrene derivatives per electrode area (assuming the transfer ratio is 1) to be 150 pmol/cm^2 for Py10 and 120 pmol/cm^2 for Py16. These values are significantly higher than the corresponding information on electrochemically active pyrene moieties extracted from cyclic voltammograms (Table 4.1) and we believe that this discrepancy can be interpreted in terms that the electrochemistry data report on the number of electrochemically active pyrene moieties rather than the total number present on the surface. The number of electroactive pyrene moieties contributing to the AC voltammetric signal (calculated from AC voltammograms at low AC frequencies) is three times that determined from CVs for monolayers, but in bilayers it is similar for both techniques. AC voltammetry shows that only about 10% of the pyrene moieties measured for the monolayer contribute to the AC voltammetric signal when the bilayer is present. Another, even more noticeable feature in the cyclic voltammograms presented in Figure 4.3 is a two to four-fold decrease in the capacitive current for bilayers relative to monolayers (20 to 8 μF/cm^2 for Py10, and 24 to 5 μF/cm^2 for Py16). This change in the capacitance is the result of an increase in film thickness and it can be understood in terms of a capacitor with increased distance between the capacitor plates,

Table 4.1 Redox properties from cyclic (CV) and AC voltammetry of tethered pyrene in mono- and bilayers.

	Γ_{CV} [pmol/cm^2]	Γ_{AC} [pmol/cm^2]	C_{AC} [μF/cm^2]	ε_{AC}	k_{et} [s^{-1}]
Py10-monolayer	9 ± 2	32 ± 3	2.8 ± 0.6	6.3 ± 1.2	283 ± 27
Py16-monolayer	7 ± 2	20 ± 8	2.8 ± 0.4	7.7 ± 1.0	262 ± 43
Py10-bilayer	6 ± 1	6 ± 1	0.3 ± 0.03	6.4 ± 0.2	434 ± 23
Py16-bilayer	8 ± 1	2 ± 1	0.8 ± 0.01	6.0 ± 0.1	142 ± 32

$$C = \frac{\varepsilon\varepsilon_0}{d} \tag{4.1}$$

where C is the specific capacitance, d is the distance between the capacitor plates, ε is the dielectric constant, and ε_0 is the permittivity of free space. The capacitive current values shown in Table 4.1 are extracted from AC voltammograms where the observed capacitance is the result of charging and discharging of a dielectric membrane only. In CV experiments there must be additional Faradaic components that perturb the system because the capacitance values extracted from CVs (data not shown) are higher than expected for this type of interface. Based on capacitance measured with electrochemical techniques and the film thickness measured with Ellipsometry (vide infra), we can also estimate the values for dielectric constants for different systems. The estimated values of dielectric constant for monolayers and bilayers are 6-8. These values are three to four times higher than dielectric constants of 2-3 commonly accepted for alkanethiol films. The reason for that may be the constrained motional freedom of the mono- and bilayer structures as well as the presence of small defects.

To obtain a selective voltammetric response from the pyrene moieties present in the surface-bound film, the monolayers and bilayers have to be relatively well organized and defect free. To evaluate the films for the presence of defects, we used two different redox probes: $K_4[Fe(CN)_6]$ and $[Ru(NH_3)_6]Cl_3$. We have chosen these two probes because they differ in the value of heterogeneous electron transfer rate constants (1.5 x 10^{-2} cm/s for $Fe(CN)_6^{4-}$ and 1.8 x 10^{-2} cm/s for $Ru(NH_3)_6^{3+}$).[22] For both redox probes,

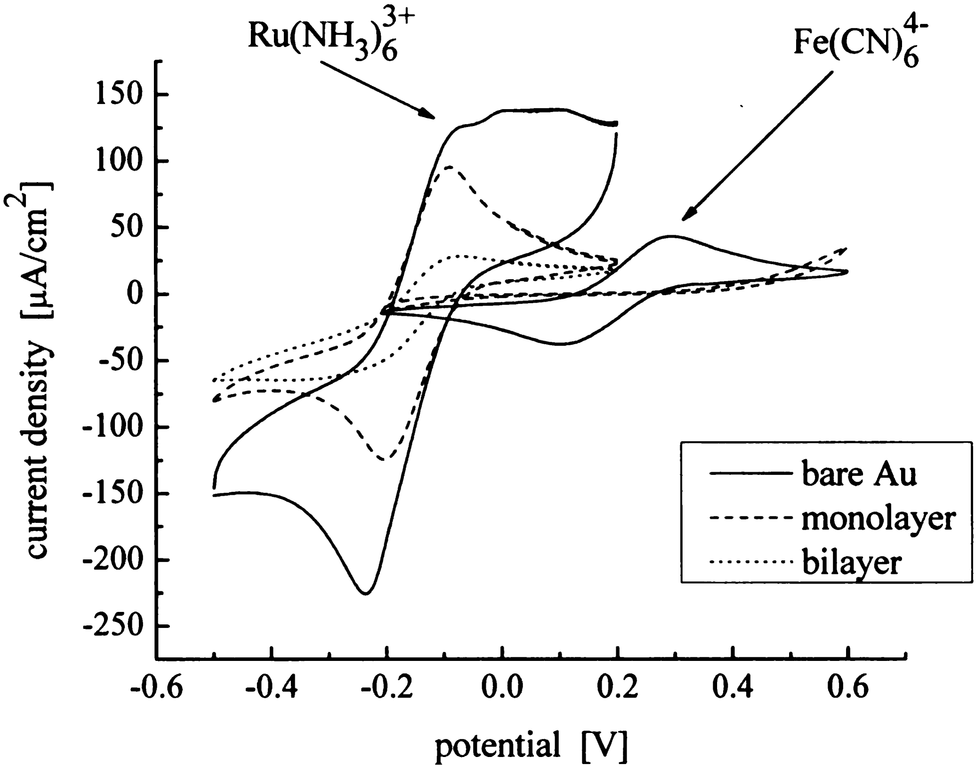

Figure 4.4 Cyclic voltammetry of pyrenehexadecanoic acid in a monolayer on gold in aqueous 1 mM $K_4[Fe(CN)_6]$ and in 1 mM $[Ru(NH_3)_6]Cl_3$ in 0.1 M $LiClO_4$. Sweep rate 100 mV/s.

the cyclic voltammograms were recorded at 100 mV/s scan rate. Cyclic voltammograms recorded for $[Fe(CN)_6]^{4-/3-}$ were characterized by an exponential shape typical for a defect-free film (Figure 4.4, potential window from -0.2 to 0.6V), while CVs recorded for $[Ru(NH_3)_6]^{3+/2+}$ exhibited well resolved peaks, indicative of the presence of defects (Figure 4.4, potential window from -0.5 to 0.2V). It has been reported elsewhere that because of the charge of these redox probes, the transfer of the $[Fe(CN)_6]^{4-}$ ion from aqueous solution to a low dielectric medium requires 80% more energy than the transfer of $[Ru(NH_3)_6]^{3+}$.[22] Since the transfer of the $[Fe(CN)_6]^{4-}$ ion trough the film was completely blocked, but the film was permeable to $[Ru(NH_3)_6]^{3+}$ ion, our films likely contain some relatively small defect sites.

FTIR Data. We are cognizant of the fact that the introduction of a fluorescence probe such as pyrene in a monolayer will give rise to disorder within the monolayer. This structural factor may contribute to the presence and detection of defects in our bilayer structures. In an attempt to evaluate the extent of organization of our L-B films on reflective substrates, we have used FT-IR spectroscopy. We use the CH_2 asymmetric and CH_2 symmetric stretches of the aliphatic chains in our bilayers as a gauge of organization (Figure 4.5). The band position for these vibrations depends on the organization of the medium. For an adlayer characterized by quasi-crystalline organization, the CH_2 stretches are seen to shift to lower energies than those seen for disordered or liquid-like films.[26-29] This effect is seen for a variety of interfacial

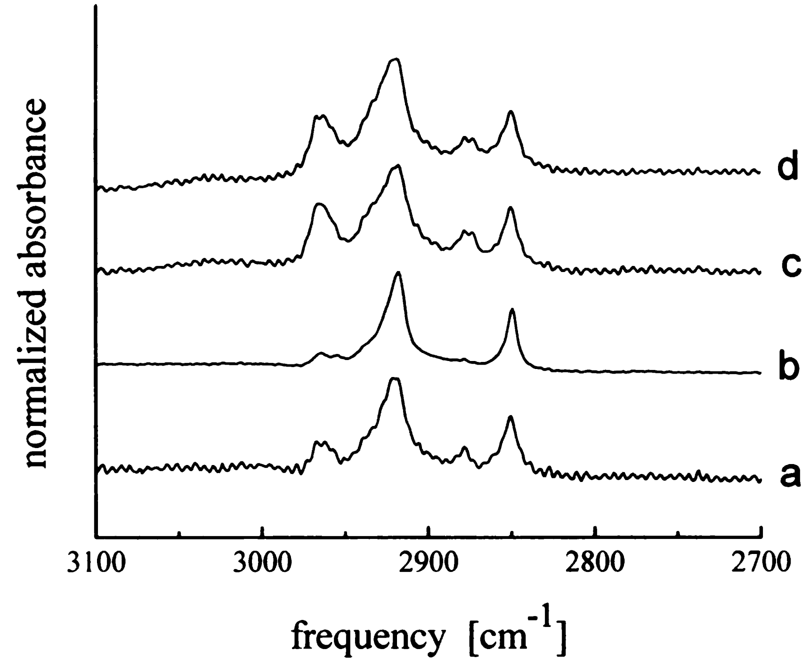

Figure 4.5 FTIR spectra of the monolayers and bilayers reported here: (a) pyrenedecanoic acid and (b) pyrenehexadecanoic acid in monolayers, (c) pyrenedecanoic acid and (d) pyrenehexadecanoic acid in bilayers. Spectral range presented here is 3100 - 2700 cm^{-1}.

Table 4.2 Peak positions for CH_2 stretching modes in crystalline and liquid states[a], and in monolayers and bilayers adsorbed on gold. [a]From reference 26

CH_2 stretch	band positions $[cm^{-1}]$					
	crystalline[a]	liquid[a]	Py10-monolayer	Py16-monolayer	Py10-bilayer	Py10-bilayer
asymmetric	2918	2924	2921	2918	2918	2919
symmetric	2851	2855	2850	2849	2850	2850

systems that contain aliphatic chains. For example, well ordered self-assembled alkanethiol monolayers on gold have CH_2 asymmetric and CH_2 symmetric stretch peaks at 2918 and 2851 cm^{-1}, respectively,[26] and the band positions for gel phase DPPC monolayers are 2920 cm^{-1} and 2851 cm^{-1} in the liquid condensed (LC) phase and 2925 cm^{-1} and 2854 cm^{-1} in the liquid expanded (LE) phase.[30] The CH_2 stretching bands shift to higher energies by ca. 5 cm^{-1} for disorganized monolayers. The FTIR data obtained for the bilayer systems we report here are given in Table 4.2. For both monolayers and bilayers containing tethered pyrene, the asymmetric CH_2 stretch is centered at 2920 cm^{-1} and CH_2 symmetric stretch is centered at 2850 cm^{-1}. These data are consistent with our films exhibiting significant order compared to a liquid-like system, but not quite the same level of organization seen for long-chain alkanethiol-gold monolayers. Our data are consistent with a DPPC layer in the LC phase,[30] suggesting that the extent of defects in these films is limited. However, pyrene moieties present in the bilayer may disrupt the crystalline bilayer structure on short length scales, as was seen in the redox probe diffusion experiments. Such "cracks" resulting from the presence of the probe may not be obvious on a macroscopic length scale.

Electron transfer across the interface. We expect, as noted above, that the kinetics of electron and proton transfer for pyrene derivatives in these films will depend on the details of film organization. We use AC voltammetry to study the kinetics associated with oxidation/reduction reaction(s) of tethered pyrene. We have acquired AC voltammograms over the frequency range of 1 Hz to 10 kHz. For these data, the peak current to background current ratio decreased with increasing AC frequency, in correspondence with the rate of electron transfer.[18] The data are modeled using a Randles equivalent circuit (Figure 4.6). Shown in Figure 4.7 are a series of AC voltammograms acquired at three different frequencies to illustrate the behavior of redox reaction of tethered pyrene with different tether lengths in our mono- and bilayer structures. It is the frequency-dependence of the data shown in Figure 4.7 that are modeled by the Randles equivalent circuit. To estimate the electron transfer rate constant from these data, we have used a model developed by Creager and Wooster.[31] In this model, the interfacial redox-active system on the electrode surface is represented by the impedance of a Randles equivalent circuit (Figure 4.6), where C_{DL} is the double layer capacitance, C_{AD} is the adsorption pseudocapacitance, R_{CT} is the charge transfer resistance, and R_{SOL} is the solution resistance.

The analysis involves plotting the AC peak current (i_{peak}) to background (baseline) current ($i_{\mathrm{background}}$) ratio versus the logarithm of AC frequency for a series of voltammograms recorded over a broad AC frequency range. These plots exhibit three distinct regions. At low frequencies $i_{\mathrm{peak}} / i_{\mathrm{background}}$ ratios approach a constant value that is related to the amount of tethered pyrene on the electrode surface. There is relatively little kinetic information in this region because the frequency is slower than the relevant redox process. The second region is at high frequencies where $i_{\mathrm{peak}} / i_{\mathrm{background}}$

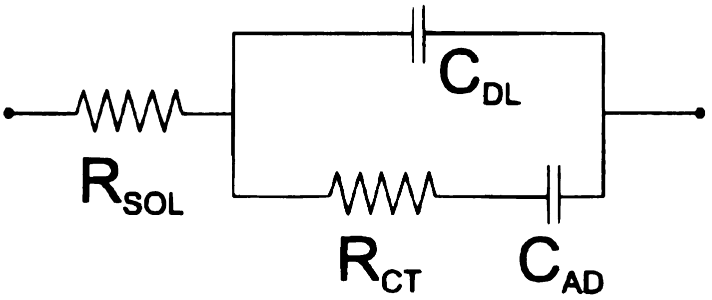

Figure 4.6 Schematic of equivalent circuit used to model the AC impedance data. R_{SOL} = solution resistance, R_{CT} = charge transfer resistance, C_{AD} = adsorption pseudocapacitance and C_{DL} = double layer capacitance.

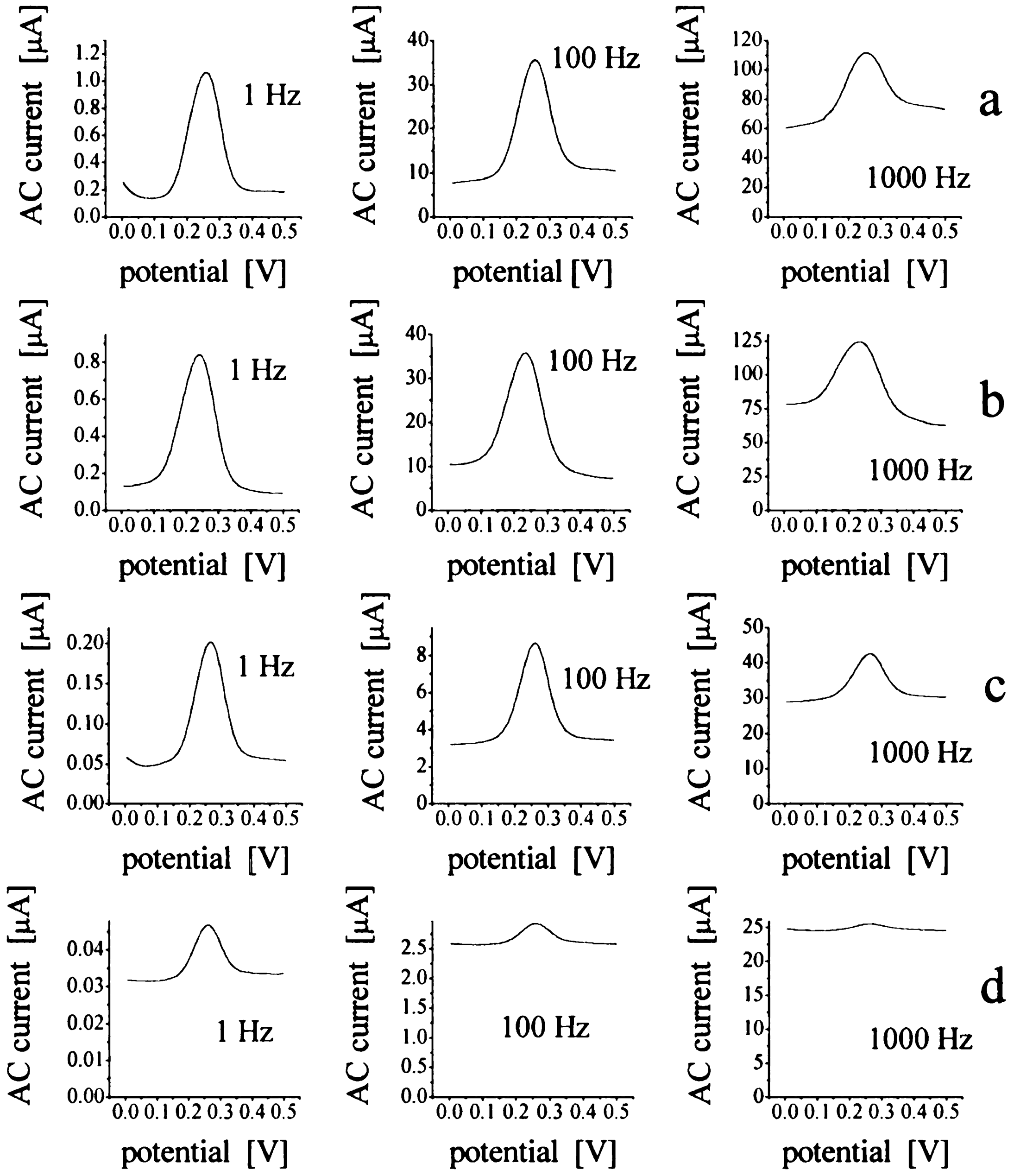

Figure 4.7 AC voltammograms recorded for pyrenedecanoic acid in a monolayer (a), pyrenehexadecanoic acid in a monolayer (b), pyrenedecanoic acid in a bilayer (c), pyrenehexadecanoic acid in a bilayer (d) in 0.1 M $HClO_4$. Frequencies shown: 1, 100, and 1000 Hz.

ratios approach unity because the redox reaction kinetics are much slower than the oscillation in the AC potential. The intermediate region is a transition between the low and high frequency limits where the $i_{\text{peak}} / i_{\text{background}}$ ratio depends sensitively on the AC frequency.[31-33] It is this region, where the AC frequency is of the same order as the electron-transfer rate constant (k_{et}) for the reaction.

We show in Figure 4.8 plots of $i_{\text{peak}} / i_{\text{background}}$ ratios vs. log(AC frequency) for a series of AC voltammograms recorded in the 1 Hz to 10 kHz range for tethered pyrene in mono- and bilayers. The average values obtained for at least three different samples are provided in Table 4.1. From the model, which assumes a single value for the electron transfer rate constant, we get a sigmoidal frequency dependence, and we see this functional form in Figure 4.8a-c. For Figure 4.8d, however, the absence of a clear low frequency plateau means that there are multiple electron transfer rate constants operating, and the lowest frequency ones are responsible for the plateau's absence. We interpret the calculated value of electron transfer rate constant from nonsigmoidal $i_{\text{peak}} / i_{\text{background}}$ curves as an average from multiple electroactive sites and/or rate constants. We note, additionally, that the recovered surface coverage values are not constant for our films (Table 4.1). We believe that these data report on the number of electrochemically active pyrene moieties rather than the total number present on the surface.

Because the relevant electrochemical reaction is a $2e^-/2H^+$ process, it is likely that

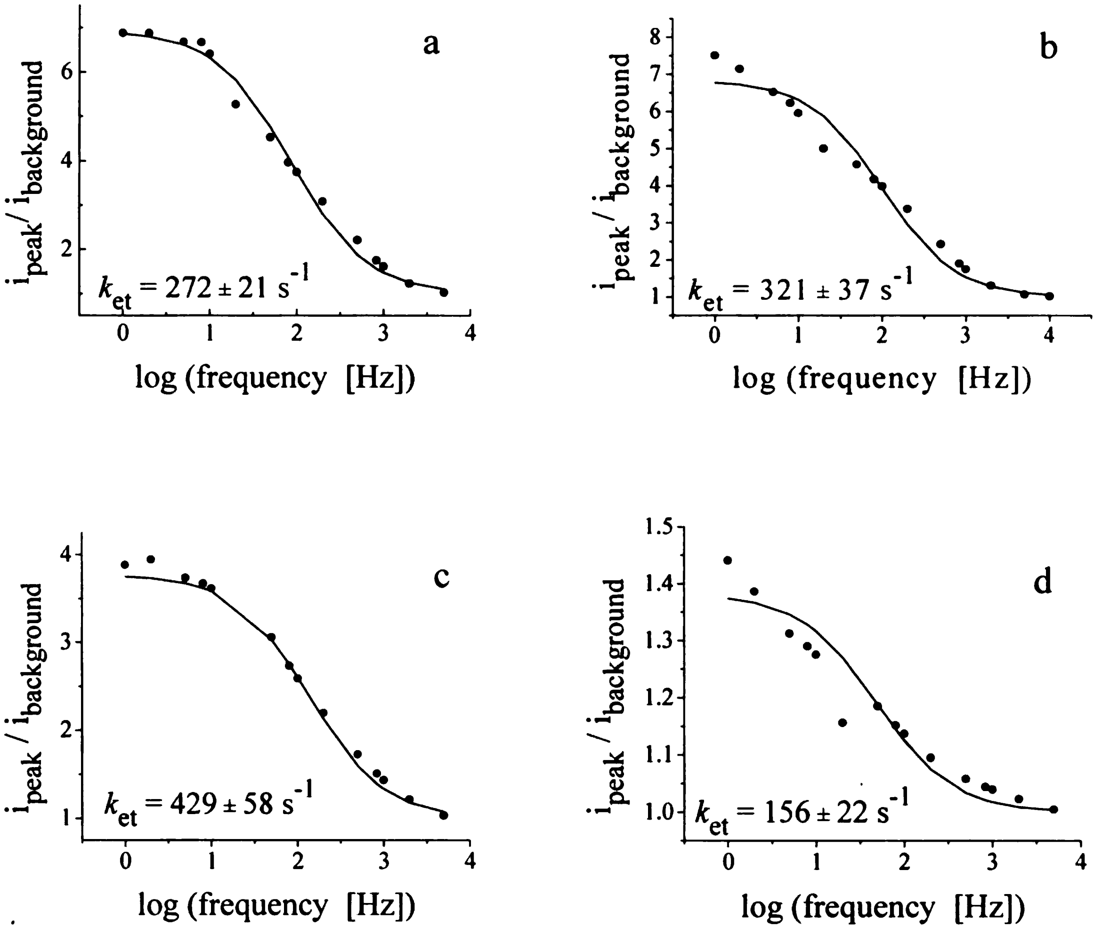

Figure 4.8 Plots of peak current/background current ratio vs. log (AC frequency) for pyrenedecanoic acid in a monolayer (a), pyrenehexadecanoic acid in a monolayer (b), pyrenedecanoic acid in a bilayer (c), pyrenehexadecanoic acid in a bilayer (d). The solid red lines represent the fit of the data (circles) to model developed by Creager's group.

the accessibility of the chromophores to protons mediates the recovered Γ values. For all of our monolayer and bilayer structures, the values obtained for electron transfer rate constants are quite small and are essentially the same, suggesting a similar environment for the electrochemically accessible tethered pyrene in all of these interfaces. One structural motif consistent with this finding is that the adlayer(s) sequester the pyrene moiety so that it has limited access to the aqueous overlayer. This type of organization is not without precedent. Finklea et al. have reported that burying the redox centers within the monolayer interior gives rise to small electron transfer rate constants, with values recovered similar to those we report here.[34] In that work, the slow electron transfer was from Ru (II/III) redox centers that were attached to a gold electrode. They interpreted the decreased apparent electron transfer rate constant for redox centers embedded in the outer portion of the monolayer relative to redox centers located in the electrolyte in terms of greater heterogeneity of environments around the redox centers. Sumner and Creager have studied "exposed" and "buried" ferrocene groups self-assembled on a gold electrode.[24] Their work has shown that the kinetics associated with ferrocene redox reactions were much more sluggish when ferrocene groups were buried within the monolayer interior than when the ferrocene groups were exposed to electrolyte. The values of electron transfer rate constants for a monolayer with buried ferrocene moieties were two orders of magnitude smaller than those obtained for the exposed ferrocene moieties. The kinetics associated with buried ferrocene oxidation/reduction were also independent of the tether length.

Based on previous studies of various redox probes located at different levels within aliphatic monolayers, we infer that the slow kinetics seen for the pyrene redox reaction in the systems we report here are the result of a shielding effect produced by the aliphatic chains. For monolayer films, this shielding occurs within the upper levels of the monolayer, since the pyrene tether is always shorter than the monolayer constituents and, for bilayers, additional shielding results from the deposition of the top lipid leaflet. The details of this shielding process are difficult to discern, since the relevant pyrene redox chemistry involves two protons and two electrons, and this environment could prove to hinder the transport of both these species. Marcus has presented the idea that ion-pairing interactions could affect the overall redox reaction kinetics.[35] He showed that for processes where electron transfer is coupled to the ion transport, the apparent electron transfer rate constant is related to both the electron transfer rate constant and the ion transfer constant. If electron transfer is fast and ion transport is slow, then ion transport will dominate the apparent rate constant for the reaction. It appears that, based on our data (Table 4.1), the comparatively slow rate constants for the pyrene diol/dione redox chemistry are limited by access of the redox couple to protons, and possibly by the electron transfer rate constant from the redox-active species to the electrode. The fact that the frequency-dependence of the AC voltammetry data produce a sigmoidal form that is modeled well by our equivalent circuit impedance analysis suggests that the distribution of environments in which the pyrene resides is comparatively narrow. A broad (energetic and/or geometric) distribution of local environments would give rise to a "linear", or nonsigmoidal form[36] in the plots shown in Figure 4.8. With this information in mind, we consider next the information we can extract from the fluorescence dynamics of these pyrene derivatives.

Fluorescence anisotropy. To interrogate the dynamics of tethered pyrene in our monolayer and bilayer structures, we have used time-resolved fluorescence spectroscopy. The most effective means for extracting molecular-scale motional information on this system is through fluorescence anisotropy measurements, where the sample is excited with a short, vertically polarized pulse of light, and polarized emission from the sample is collected at polarizations parallel and perpendicular to that of the excitation pulse (Figure 4.9a). The polarized emission transients are combined (Equation 4.2) to produce the induced orientational anisotropy function, r(t) (Figure 4.9b):

$$r(t) = \frac{I_{\parallel} - I_{\perp}}{I_{\parallel} + 2I_{\perp}} \tag{4.2}$$

For chromophores in an unconstrained environment (e.g. solution), the anisotropic orientational distribution photoselected by the excitation pulse can relax to a random orientational distribution. When the motion of the chromophore is restricted in some manner (e.g. tethering to a surface), the initial anisotropic distribution cannot orientationally re-randomize completely and r(t) does not decay to zero, as it would for a free chromophore. For such constrained systems, the hindered rotor model developed by Lipari and Szabo is useful.[37] In this model, the time course of the induced orientational anisotropy, r(t), is given by Equation 4.3:

$$r(t) = r(\infty) + \left(r(0) - r(\infty)\right)\exp\left(-t/\tau_{HR}\right) \tag{4.3}$$

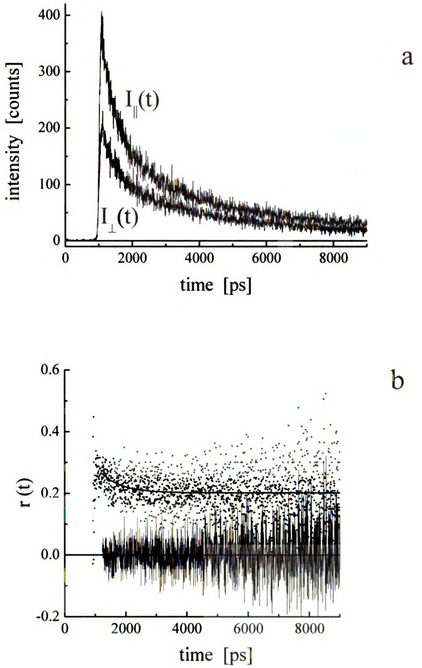

Figure 4.9 (a) Time-resolved emission intensities for polarization parallel and perpendicular to the excitation polarization for pyrenedecanoic acid in a lipid bilayer. (b) Orientational anisotropy function obtained from data shown in (a). The fit to the data is shown as the solid line and residuals are distributed around zero.

$$\sqrt{\frac{r(\infty)}{r(0)}} = 0.5 + \left(\cos\theta_0\left(1+\cos\theta_0\right)\right) \tag{4.4}$$

$$\tau_{HR} = \frac{7\theta_0^2}{24D_W} \tag{4.5}$$

The quantities $r(0)$ and $r(\infty)$ are initial and infinite-time anisotropies, which are measured experimentally. The initial anisotropy $r(0)$ is determined by the angle between the excited and emitting chromophore transition dipole moments. This model predicts that the anisotropy decays exponentially in time (Equation 4.3) as the chromophore orientational distribution rerandomizes to the extent possible. The infinite time anisotropy is related to the extent of motional restriction imposed on the chromophore by its immediate environment. The decay time constant τ_{HR} (Equation 4.5) is related to angular confinement of the chromophore, expressed in terms of a cone with semiangle θ_0 (Equation 4.4), and the "wobbling" diffusion coefficient D_W, which characterizes the motion of the chromophore about its tethering bond.

We show in Table 4.3 the quantities τ_{HR}, $r(0)$, and $r(\infty)$ obtained for tethered pyrene chromophores in our interfaces. From the $r(0)$ and $r(\infty)$data we extract θ_0 using Equation 4.4 and from the time dependence of $r(t)$ we determine D_W (Table 4.4). The θ_0 values shown in the Table 4.4 are related to the free volume accessible to tethered pyrene, and D_W values are related to the viscosity of the pyrene local environment. We note from these θ_0 data that, in general, tethered pyrene molecules reported here are

Table 4.3 Summary of time-resolved data for pyrenedecanoic and pyrenehexadecanoic acid in monolayers and bilayers.

Quantity	Py10-monolayer	Py16-monolayer	Py10-bilayer	Py16-bilayer
$\tau_{\mathrm{fl},1}$ (ps)	637 ± 10	441 ± 6	595 ± 23	671 ± 149
$\tau_{\mathrm{fl},2}$ (ps)	3550 ± 63	3278 ± 34	5089 ± 136	4943 ± 361
τ_{HR} (ps)	1498 ± 258	852 ± 350	271 ± 199	807 ± 243
$r(0)$	0.15 ± 0.01	0.22 ± 0.02	0.29 ± 0.03	0.22 ± 0.03
$r(\infty)$	0.07 ± 0.01	0.17 ± 0.01	0.21 ± 0.01	0.15 ± 0.03

Table 4.4 Results obtained for hindered rotor model based on experimental $r(\infty)$, $r(0)$, and τ_{HR} data.

Quantity	Py10-monolayer	Py16-monolayer	Py10-bilayer	Py16-bilayer
θ_0 (deg.)	39 ± 1	23 ± 3	27 ± 2	25 ± 2
D_W (MHz)	92 ± 12	62 ± 14	91 ± 12	74 ± 18

characterized by a relatively constrained environment, with θ_0 values ranging from 39° for Py10 in a monolayer to ca. 25° for the other systems studied. We account for these data as follows. The 39° value for the Py10-monolayer system indicates that there is significant motional restriction imposed on the chromophore even in the monolayer. For the Py10-bilayer, the presence of the overlayer serves to restrict the motional freedom of the underlayer, thereby restricting the motion of the chromophore further. In the case of the Py16-monolayer, the presence of the chromophore so close to the "top" of the interface allows for there to be relatively strong interchain interactions, which further constrains the available space into which the chromophore can motionally relax. For the Py16-bilayer, the same situation is seen as before, with the interactions between the adlayers producing a comparatively restricted environment. Owing to the extent of the orientational confinement already present in the monolayer, the addition of the overlayer changes this structure comparatively little. The values of θ_0 that we recover in all cases suggest that the pyrene chromophore is confined rather tightly in the surface layer(s), a result that is entirely consistent with the comparatively small values of k_{et} that we have recovered. We attribute these small values of k_{et} mostly to the limited access of H^+ to the pyrene dione species in the adlayer. The efficiency of the electron transfer between the pyrene diol/dione and the electrode surface may additionally depend on the distance of the redox moieties from the electrode surface.

We consider next the values of the wobbling diffusion constant that we recover from our experimental data. We note that this quantity is very close to the same for all systems, with there being an apparent slight differentiation between the Py10 and Py16 chromophores. This slight difference in D_W for these two chromophores does not correlate with the variations in θ_0, and likely represents a difference in motional freedom for the two chromophores that is somehow related primarily to the tether length. In both cases, the values of ca. 80 MHz that we recover for our layers suggests a viscosity on the order of 40 cP, if we assume that the Debye-Stokes-Einstein (DSE) relationship[38,39] holds for this system. Regardless of whether or not the DSE relationship is quantitatively correct, it points to the adlayer in which the chromophore resides as being a comparatively rigid and confining environment. This qualitative description is consistent with the nature of the adlayer in which the pyrene chromophore is tethered. Specifically, there are a number of Au-thiol attachment points, and while these points may be able to translate to a limited extent, their motion is impeded by the existence of the arachidic acid in the layer.

Fluorescence lifetime. We note that the fluorescence lifetime data for tethered pyrene in mono- and bilayers is consistent with that which we have seen elsewhere.[16,40] For surface-bound pyrene species, a two-component exponential decay (Figure 4.10) is typically observed. The mechanistic reasons for this decay functionality remain to be determined fully, but it is possible that these data represent a distribution of lifetimes rather than simply two discrete components. It is well known that pyrene fluorescence is quenched efficiently by oxygen, and we have not performed any deoxygenation on our samples. This is the reason for the comparatively short lifetimes we measure for this chromophore. The most prominent feature in these data is the difference in τ_2 values between monolayers and bilayers. The longer of the two fluorescence time constants for the tethered pyrene derivatives in our bilayer structures is consistently longer than it is in the monolayer structures. We postulate that this difference is related to the accessibility of oxygen to the chromophore, which should be reduced in the bilayer.

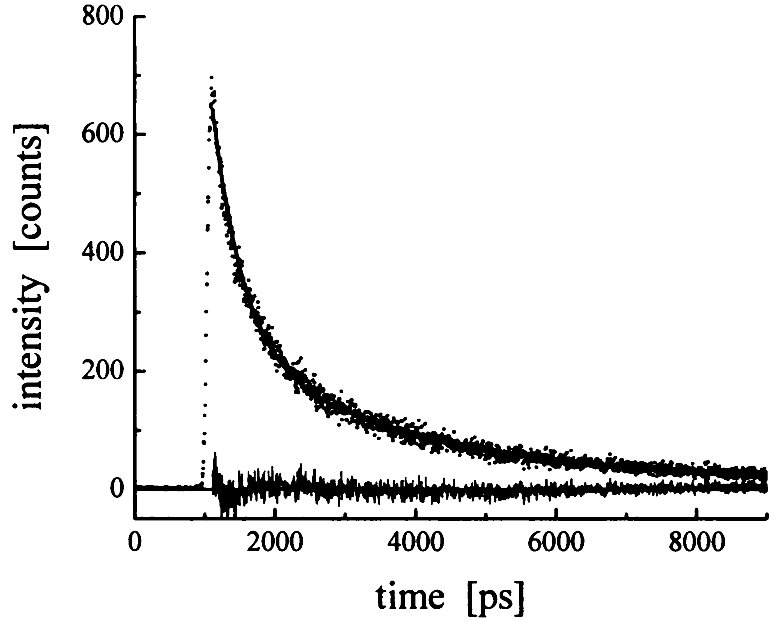

Figure 4.10 Fluorescence lifetime data for pyrenehexadecanoic acid in a monolayer on quartz. These are representative for all the lifetime data obtained for the systems reported in this paper. The fits to all the data are presented in Table 3. Residuals show the agreement of the fit to a double exponential decay function.

Conclusions

There are several important parameters that have to be considered when designing biosensing devices. Biomolecules such as transmembrane proteins require specially designed matrices that mimic the natural environment of the transmembrane protein. Transmembrane proteins span the biological membrane in such a way that the hydrophobic region(s) reside in the interior of the lipid bilayer, while hydrophilic portions of the protein are located in aqueous compartments present on both sides of the lipid membrane. An important aspect of the construction of supported biomimetic systems is the incorporation of "reporter" molecules that are capable of interrogating the bilayer local organization. For information from such molecules to be useful, they must be localized at predetermined locations within the bilayer structure, and one way to achieve this goal is to tether the probe molecule to the supporting interface. In this paper we have focused on the organization of a bilayer structure absent protein incorporation. Our model system was a bilayer comprised of a bottom leaflet of fatty acids and fatty acid analogues and a top leaflet of phospholipids. Some of the fatty acid analogues were pyrene derivatives that we use to probe the organization and electron-transfer characteristics of the fatty acid monolayer and lipid-capped bilayer. We have shown that electron transfer from tethered pyrene buried within the mono- and bilayers is relatively slow and almost independent of the length of the tether connecting pyrene to the electrode surface. These data suggest that the bilayer is organized sufficiently well to prevent ready access of the tethered chromophore to the electrode surface. Consistent with this level of organization is the sequestration of the probe away from the aqueous overlayer and access to protons. Time-resolved fluorescence anisotropy decay measurements indicate that the tethered pyrene resides in a relatively constrained environment, as detected by the small volume accessible for the chromophore to rotate within, and the slow rate of motion. These data suggest subtle differences in mono- and bilayer organization that are expected based on the capping properties of the lipid overlayer. The information we have gained from this work provides a foundation for investigating phospholipid bilayer structures with variable amounts of tethering connections to their supporting substrate. We anticipate these studies to yield a rational approach to the creation of simple biomimetic structures capable of supporting selected transmembrane proteins in their active forms.

Literature Cited

(1) Ataka, K.; Giess, F.; Knoll, W.; Naumann, R.; Haber-Pohlmeier, S.; Richter, B.; Heberle, J. *Journal of the American Chemical Society* **2004**, *126*, 16199-16206.

(2) Giess, F.; Friedrich, M. G.; Heberle, J.; Naumann, R. L.; Knoll, W. *Biophysical Journal* **2004**, *87*, 3213-3220.

(3) Kiessling, V.; Tamm, L. K. *Biophysical Journal* **2003**, *84*, 408-418.

(4) Majewski, J.; Wong, J. Y.; Park, C. K.; Seitz, M.; Israelachvili, J. N.; Smith, G. S. *Biophysical Journal* **1998**, *75*, 2363-2367.

(5) Merzlyakov, M.; Li, E.; Gitsov, I.; Hristova, K. *Langmuir* **2006**, *22*, 10145-10151.

(6) Tien, H. T.; Ottova, A. L. *Electrochimica Acta* **1998**, *43*, 3587-3610.

(7) Wagner, M. L.; Tamm, L. K. *Biophysical Journal* **2000**, *79*, 1400-1414.

(8) Tanaka, M.; Sackmann, E. *Nature (London, United Kingdom)* **2005**, *437*, 656-663.

(9) Tanaka, M.; Sackmann, E. *Physica Status Solidi A: Applications and Materials Science* **2006**, *203*, 3452-3462.

(10) Chan, Y.-H. M.; Boxer, S. G. *Curr. Current Opinion in Chemical Biology* **2007**, *11*, 581-587.

(11) Singer, S. J.; Nicolson, G. L. *Science (Washington, DC, United States)* **1972**, *175*, 720-31.

(12) Dong, D. C.; Winnik, M. A. *Photochemistry and Photobiology* **1982**, *35*, 17-21.

(13) Kalyanasundaram, K.; Thomas, J. K. *Journal of the American Chemical Society* **1977**, *99*, 2039-44.

(14) Karpovich, D. S.; Blanchard, G. J. *Langmuir* **1996**, *12*, 5522-5524.

(15) Mazur, M.; Blanchard, G. J. *Journal of Physical Chemistry B* **2005**, *109*, 4076-4083.

(16) Dominska, M.; Krysinski, P.; Blanchard, G. J. *Journal of Physical Chemistry B* **2005**, *109*, 15822-15827.

(17) Mazur, M.; Blanchard, G. J. *Journal of Physical Chemistry B* **2004**, *108*, 1038-1045.

(18) Dominska, M.; Jackowska, K.; Krysinski, P.; Blanchard, G. J. *Journal of Physical Chemistry B* **2005**, *109*, 15812-15821.

(19) Blodgett, K. B. *Journal of the American Chemical Society* **1934**, *56*, 495.

(20) Blodgett, K. B.; Langmuir, I. *Physical Review* **1937**, *51*, 964-82.

(21) Langmuir, I.; Schaefer, V. J. *Journal of the American Chemical Society* **1938**, *60*, 1351-60.

(22) Krysinski, P.; Brzostowska-Smolska, M. *Journal of Electroanalytical Chemistry* **1997**, *424*, 61-67.

(23) DeWitt, L.; Blanchard, G. J.; LeGoff, E.; Benz, M. E.; Liao, J. H.; Kanatzidis, M. G. *Journal of the American Chemical Society* **1993**, *115*, 12158-64.

(24) Sumner, J. J.; Creager, S. E. *Journal of Physical Chemistry B* **2001**, *105*, 8739-8745.

(25) Twardowski, M.; Nuzzo, R. G. *Langmuir* **2003**, *19*, 9781-9791.

(26) Porter, M. D.; Bright, T. B.; Allara, D. L.; Chidsey, C. E. D. *Journal of the American Chemical Society* **1987**, *109*, 3559-68.

(27) Allara, D. L.; Nuzzo, R. G. *Langmuir* **1985**, *1*, 45-52.

(28) Laibinis, P. E.; Whitesides, G. M.; Allara, D. L.; Tao, Y. T.; Parikh, A. N.; Nuzzo, R. G. *Journal of the American Chemical Society* **1991**, *113*, 7152-67.

(29) Persson, H. H. J.; Caseri, W. R.; Suter, U. W. *Langmuir* **2001**, *17*, 3643-3650.

(30) Mitchell, M. L.; Dluhy, R. A*Journal of the American Chemical Society* **1988**, *110*, 712-18.

(31) Creager, S. E.; Wooster, T. T. *Analytical Chemistry* **1998**, *70*, 4257-4263.

(32) Creager, S.; Yu, C. J.; Bamdad, C.; O'Connor, S.; MacLean, T.; Lam, E.; Chong, Y.; Olsen, G. T.; Luo, J.; Gozin, M.; Kayyem, J. F. *Journal of the American Chemical Society* **1999**, *121*, 1059-1064.

(33) Weber, K.; Hockett, L.; Creager, S. *J. Journal of Physical Chemistry B* **1997**, *101*, 8286-8291.

(34) Finklea, H. O.; Liu, L.; Ravenscroft, M. S.; Punturi, S. *Journal of Physical Chemistry* **1996**, *100*, 18852-18858.

(35) Marcus, R. A. *Journal of Physical Chemistry B* **1998**, *102*, 10071-10077.

(36) Li, J.; Schuler, K.; Creager, S. E. *Journal of the Electrochemical Society* **2000**, *147*, 4584-4588.

(37) Lipari, G.; Szabo, A. *Biophysical Journal* **1980**, *30*, 489-506.

(38) Debye, P. *Polar Molecules*.

(39) Perrin, F. *Journal de Physique et le Radium* **1934**, *5*, 497-511.

(40) Mazur, M.; Blanchard, G. J. *Bioelectrochemistry* **2005**, *66*, 89-94.

CHAPTER 5

CONSTITUENT-DEPENDENT LIPOSOME STRUCTURE AND ORGANIZATION

Introduction

In the bio-sensing community there is a great deal of effort focused on the development of biomimetic interfaces on planar substrates for the purpose of supporting transmembrane proteins in their active form(s). There are many issues that need to be considered in the creation of a functional biomimetic interface, and among them is the ability to attach the biomimetic interface to a transducer (*e.g.* electrode, spectroscopic window). The biomimetic interface is a lipid bilayer-based structure, and a key property of lipid bilayers is their fluidity. Indeed, the structural heterogeneity and fluidity of lipid bilayers are prerequisites for the incorporation of transmembrane proteins. Most biomolecules lose their biological activity when removed from their native environment, and one approach to maintaining their bioactivity is to create a local environment on a transducer surface that mimics the native environment of the biomolecule. Because transmembrane proteins in their native environment experience an aqueous medium on both sides of the bilayer, it will be important to create analogous organization on the surface of any viable biosensor. To construct such an interface on a gold (electrode) surface, we have designed and synthesized a lipid molecule conjugated with a short polyethylene glycol (PEG) chain terminated with a thiol functionality. Our goal in creating such a molecule is to form vesicles enriched with this modified lipid so that vesicle fusion on a gold substrate would produce a stable supported bilayer structure that retains some fluidity in the bottom (attached) leaflet. Our findings are that the addition of our modified thio-PEG containing lipid serves to do more than simply enhance binding to an Au surface. The presence of the thio-PEG lipid produces changes in the morphology of the solution phase lipid structures, which serve to alter the ability of the lipid adlayer to bind to the Au interface. It is these changes in liposome morphology and local organization that we are concerned with in this work.

The notion that the bilayer constituents can give rise to changes in the morphology of the liposomes is not new. There is a body of literature that points to the effect of micelle-forming lipids, such as those containing PEG functionalities, driving the conversion of spherical lipid bilayers into small micelles. Hristova *et al.* suggested that the main reason for liposome transformation into a micelle is the shape of the PEG-lipid molecule and that the steric barrier to liposome formation resulting from the presence of a head group-bound polymer chain determines the maximum amount of PEG-lipid that can be incorporated into a spherical bilayer.[1] Phase separation and aggregation of PEG-lipid/phospholipid mixtures has been investigated in several different ways. The influence of polymer length on the point of bilayer saturation with PEG-lipids has been explored, revealing that the gel phase of the lipid bilayer is maintained with up to 8-10% of PEG-lipids present, where the PEG polymer lengths range from 350 to 5000 Da, and that above 10%, the lipid bilayer organization is dependent on PEG chain length.[2-4] Shorter PEG chains and intermediate concentrations of longer PEG chain-containing lipids have been used to mediate the formation of integrated bilayers, while high concentrations of longer PEG-containing lipids were shown to form micelles.[2-4] The most efficient incorporation of PEG-lipids into liposomes has been shown to take place when the PEG polymer chain matches the length of a lipid acyl chain.[4]

The conversion of a vesicle into a micelle has been also examined for various lipid acyl chain lengths.[1,5,6] In that work it was found that micelles formed more readily with lipids possessing long acyl chains. Rovira-Bru *et al.* used molecular mean field theory to calculate the optimal size and structure of spontaneously formed liposomes composed of lipid/PEG-lipid mixtures.[7] According to their predictions, the compositional asymmetry between the two lipid leaflets in a vesicle is much larger for a vesicle containing PEG-lipids than for a vesicle composed of unmodified lipids, and that the size of the liposome influences the extent of asymmetry, with smaller liposomes producing more asymmetric lipid distributions. These authors also indicated that there is a strong tendency for the PEG head group functionality to locate on the outer surface of the vesicle, thereby placing limits on the loading density of PEG-modified lipids for which vesicles are stable. Also, according to their calculations, a very small polymer loading excess causes the small micelles to become the most energetically favorable structure. There is evidence in the literature suggesting PEG-modified lipids have a significant influence on the structure of lipid aggregates. PEG-modified lipids have been shown to induce "open" bilayer disc or micellar disc structures, with exposed bilayer edges, when introduced into vesicles in concentrations lower than that at which mixed spherical micelles start to form.[5,8] The formation of disc-like and open bilayer fragments has been seen during solubilization of liposomes by a number of surfactants.[9-12]

However, disc or bilayer fragments are not stable in solution and tend to close on themselves to form lipid vesicles. In addition to forming self-closing structures, the amelioration of exposed edges and consequent stabilization of discs and bilayer fragments can be achieved by incorporation of molecules into the bilayer that are capable of shielding the open edges.[13-15] PEG-lipids with a bulky, hydrophilic polymer chain attached to the lipid headgroup can easily accommodate to highly curved lipid monolayer (or bilayer) regions that are present at the edges of discoidal micelles. The presence of the bulky polymer at the edge of the disc can prevent closure of bilayer fragments or fusion of discoids. PEG-lipid concentrations higher than 10 mol% in lipid assemblies trigger a transition from a lamellar phase to a micellar phase, which proceeds through the intermediate state of a discoidal bilayer.

To gain insight into the organization and dynamics of molecules comprising mixed lipid aggregates, we have prepared small liposomes containing controlled amounts of thio-PEG lipid and a small amount of either pyrene labeled DPPC or perylene as optical probe molecules. The maximum diameter of the aggregates we produced was controlled by the pore size of the polycarbonate membrane used in the extrusion process. We have used time-resolved spectroscopy to measure the fluorescence lifetime and anisotropy decay behavior of perylene as a function of liposome composition to understand how the local environment of the probe changes with the addition of thio-PEG lipids. This chromophore is a hydrophobic polycyclic aromatic hydrocarbon (PAH), for which there is significant knowledge of its spectroscopy and dynamics.[16-19] We have also examined the steady state and time-resolved spectroscopic response of pyrene-tethered DPPC incorporated into our liposomes.[20-22] Fluorescence lifetime data indicate that the immediate environment of tethered pyrene changes with the addition of thio-PEG lipids. The fluorescence lifetime of the chromophore is sensitive to the presence of O_2, and the addition of thio-PEG lipid to the lipid assemblies allows O_2 in solution more access to the chromophore, resulting in the quenching of pyrene fluorescence. The dynamics of tethered chromophore also change with the addition of PEG-lipid to the liposomes, while the dynamics of perylene remain constant. This finding indicates that the presence of the PEG head group has a limited influence on the lipid acyl chain region.

Experimental Section

Chemicals. 1,2-Dipalmitoyl-*sn*-glycero-3-phosphocholine (DPPC) (≥99%), 1-Palmitoyl-2-(pyrene-1-yl)decanoyl-*sn*-glycero-3-phosphocholine (Py-DPPC) (≥95%), 1,2-dipalmitoyl-*sn*-glycero-3-phosphoethanolamine (DPPE), *O*-(2-Carboxyethyl)-*O*′-(2-mercaptoethyl) heptaethylene glycol (thio-PEG), *N*-(3-Dimethylaminopropyl)-*N*′-ethylcarbodiimide hydrochloride, pyrene (99%), perylene (≥99%) were purchased from Sigma-Aldrich. Chloroform (HPLC grade) was purchased from OmniSolv.

Thio-PEG lipid synthesis, purification and characterization. Thio-PEG conjugated DPPE lipid (thio-PEG-DPPE) was synthesized consistent with the procedure described by Krysinski *et al.*[23,24] A solution of DPPE (100 mg, 0.14 mmol) and thio-PEG (66 mg, 0.14 mmol) in chloroform was stirred under nitrogen. To this solution a drop of triethylamine was added to deprotonate the lipid amine group. Next EDC (30 mg, 0.14 mmol) in chloroform was added dropwise to the reaction mixture with continuous stirring. The reaction solution was stirred at room temperature for 24 h. The product was purified using silica gel column chromatography (Silica gel from Spectrum, 6-16 mesh; chloroform/methanol/water 20/5/1 v/v/v eluent) and analyzed by mass spectrometry (Waters QTOF Ultima with electrospray ionization). The yield of this reaction was 77% after purification.

Vesicle preparation. DPPC, thio-PEG-DPPE, and either Py-DPPC (0.5 mol %), pyrene or perylene (0.1 mol %) were mixed in chloroform in appropriate proportions. Chloroform was then evaporated and Milli-Q water (Millipore purification system, Bedford, MA) was added to produce a 1.4 mM lipid solution. Each mixture was processed three times through a freeze-thaw-vortex cycle to ensure complete lipid and fluorescent probe mixing. In every cycle the solution was frozen by immersion in $N_2(l)$ for 5 min, thawed in 55 °C water bath for 5 min and vortexed for 1 min. After the three freeze-thaw-vortex cycles, the solution was extruded eleven times through a polycarbonate membrane with 100 nm pore diameter (Avanti Polar Lipids Inc., Alabaster, AL). Extrusions were performed above the DPPC transition temperature (41°C, NIST Lipid Thermotropic Phase Transition Database).

Transmission Electron Microscopy (TEM) Imaging. Liposome samples were stained with 1 % uranyl acetate. A 5 μL drop of stained liposome solution was placed on a Formvar copper grid (200 mesh) and incubated for several minutes. The excess solution was removed with filter paper. The microscope used is 100 CX JEOL instrument (Japan) operating at 100 kV.

Steady-State Emission Spectroscopy. Excitation and emission spectra were acquired using a Spex Fluorolog 3 spectrometer. The excitation wavelength was 325 nm for pyrene and Py-DPPC containing samples and 415 nm for samples containing perylene. Both excitation and emission monochromator slits were set to 1 nm band-pass.

Time-Resolved Emission Measurements. A time-correlated single photon counting (TCSPC) system was used to acquire time-domain polarized fluorescence intensity decays. The source laser is mode-locked CW $Nd:YVO_4$ laser (Spectra Physics Vanguard) that produces 2.5 W average power at 355 and 2.5 W average power at 532 nm with 13 ps pulses at 12.5 ns intervals. The 532 nm output of this laser is used to excite a cavity-dumped dye laser (Coherent 702-2) operating at 640 nm using Kiton Red

620 dye (Kodak Eastman Fine Chemicals). The dye laser produces 5 ps pulses with ~200 mW average power at a 4 MHz repetition rate. A Type I KDP SHG crystal is used to frequency double the dye laser output and produce 320 nm pulses to excite pyrene-containing samples. The average power of the 325 nm light at the sample is less than 1 mW. For the samples containing perylene as a probe, the 355 nm output of the Nd:YVO_4 laser is used to excite a cavity-dumped dye laser (Coherent 702-2) operating at ca. 430 nm with Stilbene 420 dye (Exciton). This dye laser produces 5 ps pulses with ~100 mW average power at a 4 MHz repetition rate. Polarized emission from the sample was collected using a 40x reflecting microscope objective, and routed to two detection channels. The collection wavelength was set using subtractive double monochromators (Spectral Products CM112) and detected using microchannel plate photomultipliers (Hamamatsu R3809U-50). The two signal channels were routed to a Becker & Hickl SPC-132 dual channel module containing the time-correlation electronics (constant fraction discriminators, time-to-amplitude converters, multichannel analyzers). The reference signal was collected using a photodiode (Becker & Hickl PHD-400-N) and routed through a Becker & Hickl DEL-350 programmable delay module to the reference inputs of the SPC-132 electronics. The hardware was controlled using a National Instruments LabVIEW® program written in-house. The instrument response function for this system is typically ca. 30 ps.

Results and Discussion

The primary purpose of this work is to better understand the effect of thio-PEG lipids on the organization and dynamics of molecules comprising liposomes and micelles. As noted above, the presence of thio-PEG lipid has a substantial effect on the shape of lipid aggregates, with a progression of structures from liposomes at low thio-PEG lipid concentrations to discs and/or micelles at high thio-PEG lipid concentrations. In the work we present here, we interrogate the nonpolar region of vesicles, intermediate structures in transition from lamellar to micellar phases, and micelles, to elucidate the molecular-scale consequences of adding PEG-containing lipids to lipid structures. We have used thiol-terminated PEG-lipids because we are also interested in fusion of liposomes to planar substrates and the thiol terminal functionality provides the required affinity for a gold substrate.

Before considering the dynamics of the probe molecules in detail, it is instructive to examine pictorially the changes in lipid organization with the addition of thio-PEG-DPPE. Representative TEM images acquired for lipid structures composed of a range of DPPC/thio-PEG-DPPE molar ratios are shown in Figure 5.1. The images show the transition from spherical unilamellar vesicles for low thio-PEG-DPPE concentrations (< 10 mol %) to small spherical micelles at high thio-PEG-DPPE concentrations (> 50 mol %), with an intermediate state of discoidal lipid assembly. Similar results were presented by Johnsson and Edwards who characterized their PEG-lipid containing aggregates with cryo-transmission electron microscopy and dynamic light scattering.[8] Using these techniques for comparable systems with longer polymer chains, they found out the onset

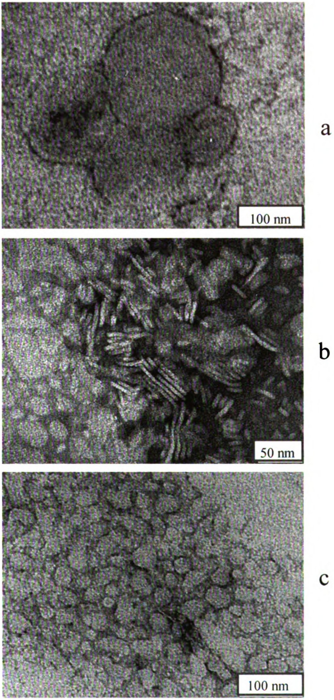

Figure 5.1 TEM images of liposomes containing 2 mol % (a), 50 mol % (b) and 100 mol % of thio-PEG-DPPE.

chain used in our study is much shorter than the polymers investigated by Johnsson and Edwards, and this factor may account for the presence of stable vesicles at thio-PEG-DPPE levels up to 10 mol %. We observe discoidal lipid assemblies (Figure 5.1, center) for thio-PEG-DPPE concentrations between 20 and 50 mol %. Small spherical micelle formation becomes more evident at thio-PEG-DPPE concentrations above 50 mol %. It is clear that the presence of thio-PEG-DPPE has a significant influence of the mesoscopic morphological properties of the lipid assemblies. The reasons for these structural changes are likely complex, mediated by both steric and solvation effects, and a key question is how these changes in nanoscale organization influence molecular scale organization. We use spectroscopic means to evaluate this issue.

We have used fluorescent probes to study molecular-scale dynamics in lipid assemblies with shapes influenced by thio-PEG-DPPE over a range of modified lipid concentrations. For these studies, we have incorporated a small, constant amount pyrene-modified DPPC into lipid structures to interrogate local organization. The steady-state absorption and emission spectroscopy of pyrene is well established and understood, and can provide some insight. One of the most important properties of this chromophore is its ability to sense the polarity of its local environment through the ratio of first (~372 nm) and third (~383 nm) vibronic bands.[25-27] The pyrene I/III emission band ratio varies from 0.6 for nonpolar solvents such as hexane to 1.9 for polar solvents such as water. This effect is known to be the result of vibronic coupling in the pyrene molecule, where the local solvent dielectric response serves to mix contributions to vibronic coupling between two orthogonal electronic states.[27] Substituents to the pyrene ring structure break the symmetry of the chromophore and can influence the details of vibronic coupling differently than is the case for the symmetric chromophore. For this reason, tethered pyrene has been reported to exhibit a somewhat decreased sensitivity to environmental polarity.[22,28] Emission from pyrene labeled DPPC in vesicles and micelles containing controlled amounts of thio-PEG-DPPE does not exhibit substantial changes to the I/III band ratio (Figure 5.2a). The I/III band ratio recorded for these systems is ~2.5 and is independent of thio-PEG lipid concentration. This value for the I/III band ratio exceeds the limits seen for a range of solvents using the unsubstituted pyrene chromophore.[26] We attribute the form of these data to the presence of the substituent on the pyrene ring system, and it appears that there is limited information available from this tethered chromophore, save from the fact that this band ratio is likely consistent with a very nonpolar environment, consistent with expectations. To elucidate the actual polarity of the probed environment, we measured fluorescence emission of (un-tethered) pyrene in the analogous lipid systems. The pyrene I/III emission band ratios for our lipid structures are ca. 1.0 - 1.1 over the range of thio-PEG-lipid concentrations used (Figure 5.2b). This band ratio value corresponds to intermediate polarity on the *py* scale, suggesting an environment similar to solvents such as *n*-butanol or *n*-propanol. Another interesting feature seen for both pyrene-labeled DPPC and free pyrene emission is the appearance of an excimer emission band at low and intermediate thio-PEG-lipid concentrations (Figure 5.3). More excimers were formed when the free probe was used, but for both bodies of data, the excimer intensity *decreased* at high thio-PEG-DPPE concentrations. This finding suggests that the chromophores are solvated more effectively by the lipid acyl chain environment or are partially partitioned into PEG-containing domains at high thio-PEG-DPPE concentrations. Dilution of the probe,

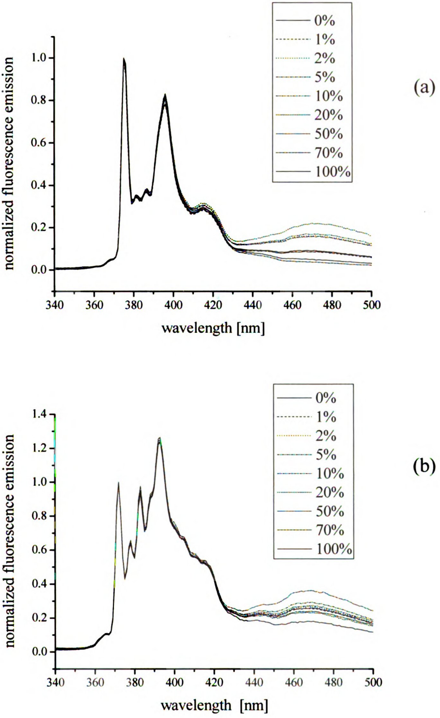

Figure 5.2 Steady-state fluorescence of: pyrene-labeled DPPC (a) and pyrene (b) in liposomes and micelles containing various concentrations of thio-PEG-lipid. Spectra normalized to emission peak I (472 nm).

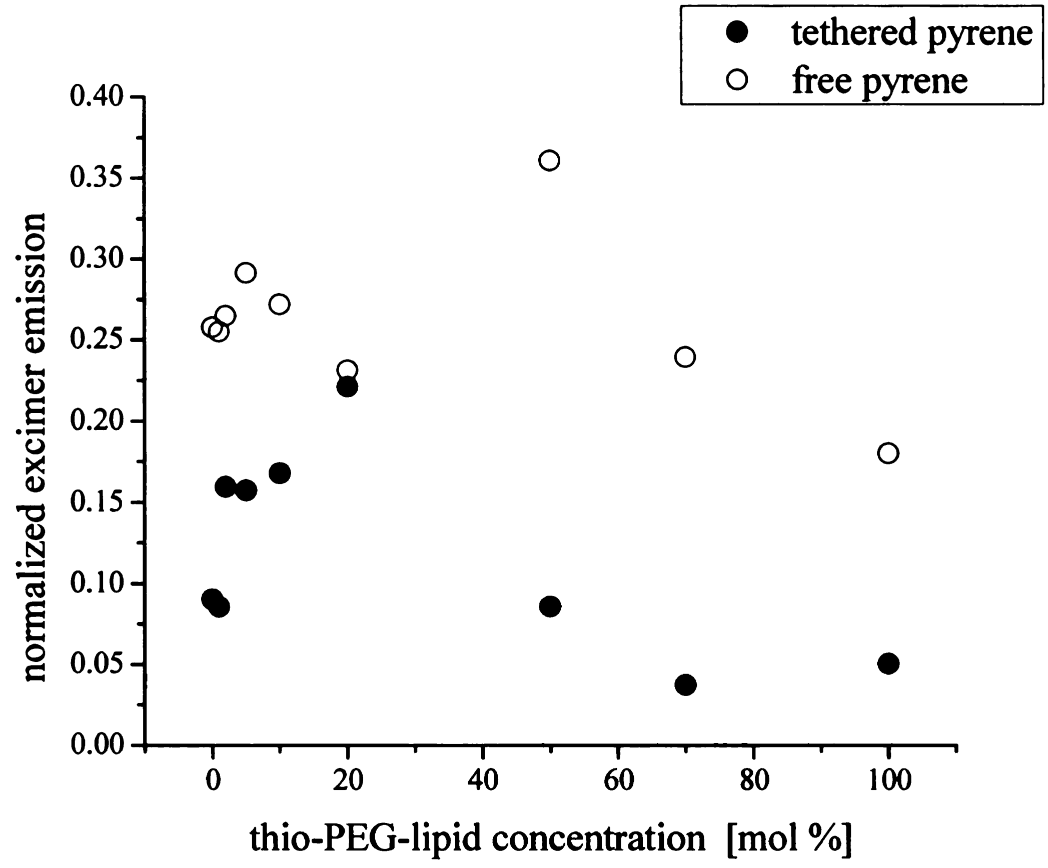

Figure 5.3 Excimer emission intensities plotted versus the amount of thio-PEG-lipid in the liposomes. Intensities are normalized to emission peak I (472 nm).

whether it resides inside the micelle or in the PEG-containing headgroup region, may be influenced by the presence and density of the bulky polymer in the lipid headgroup.

The steady state emission data for pyrene provide some insight into the chromophore local environment, but do not yield any significant information on how that environment changes with the addition of thio-PEG-DPPE. Time-domain emission measurements can provide complementary information and it is these data we consider next. Fluorescence lifetime data obtained for pyrene labeled DPPC point to two-component exponential decay (Figure 5.4) which has been seen previously for tethered pyrene derivatives.[21,29] The two-component lifetime can be understood in the context of the tethered chromophores residing in a range of environments. The fluorescence lifetime data for all the systems we have studied here are listed in the Table 5.1. Both fluorescence lifetime components decrease significantly for thio-PEG-DPPE concentrations above 10 mol %. The shorter fluorescence lifetimes are consistent with increased access of dissolved O_2 to the chromophore when it is incorporated in micellar structures relative to its incorporation in liposomes. These lifetime data, considered together with the I/III emission band ratio data for tethered and free pyrene imply that the chromophore resides in a dielectric gradient, and the most likely region for this to occur for a lipid structure is in a region that spans the acyl chain and headgroup functionalities. The quenching of fluorescence by O_2 in micellar systems suggests a possible dilation of the lipid headgroup region due to the presence of the thio-PEG terminal functionalities.

To gauge the dynamics of tethered pyrene in lipid vesicles, micelles, and transitional structures, we measured fluorescence anisotropy decay. For this measurement, the sample is excited with short, vertically polarized light pulse, producing

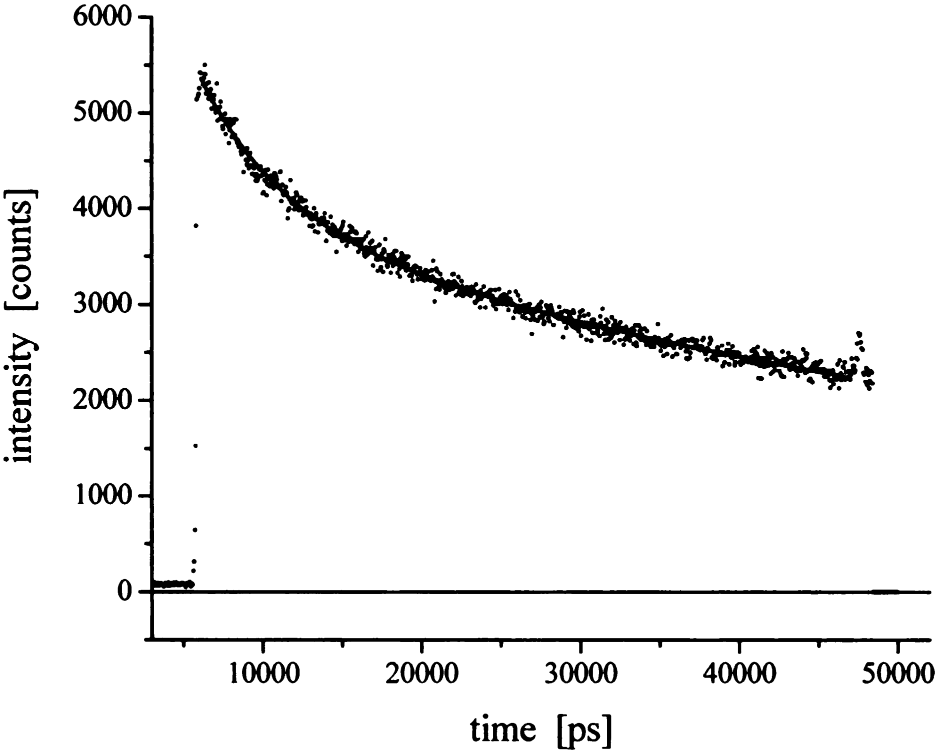

Figure 5.4 Fluorescence lifetime data for pyrene labeled DPPC in DPPC vesicles (0 mol % of thio-PEG-lipid) in water. This is representative for all the lifetime data obtained for the systems reported in this work. The fits to all the data are presented in the Table 1. Residuals (centered around zero) show the agreement of the fit to a double exponential decay function.

Table 5.1 Summary of time-resolved fluorescence data for pyrene labeled DPPC in all the systems reported in this paper. The percentage corresponds to mol % of thio-PEG-DPPE in the particular system.

quantity	0%	1%	2%	5%	10%	20%	50%	70%	100%
$\tau_{fl,1}$ [ps]	5789 ± 179	6482 ± 675	6678 ± 345	6787 ± 238	6811 ± 506	6182 ± 778	5419 ± 233	4716 ± 24	5310 ± 294
$\tau_{fl,2}$ [ps]	78026 ± 511	91340 ± 2692	76029 ± 1762	76923 ± 2114	69299 ±2218	57188 ± 3513	58462 ± 2620	53307 ± 594	67063 ± 1325
τ_{HR} [ps]	6781 ± 719	8415 ± 1636	7954 ± 940	8027 ± 414	7285 ± 789	5733 ± 242	5705 ± 192	4250 ± 178	3480 ± 144
$r(0)$	0.12 ± 0.02	0.12 ± 0.01	0.11 ± 0.01	0.11 ± 0.01	0.12 ± 0.01	0.11 ± 0.01	0.12 ± 0.01	0.15 ± 0.01	0.14 ± 0.01
$r(\infty)$	0.07 ± 0.02	0.07 ± 0.01	0.07 ± 0.01	0.06 ± 0.01	0.06 ± 0.01	0.04 ± 0.01	0.03 ± 0.01	0.02 ± 0.01	0.02 ± 0.01

a polarized emission transient from the sample. The polarized emission transient is collected at polarizations parallel and perpendicular to the excitation pulse (Figure 5.5a). The polarized emission intensities ($I_{\parallel}$ and $I_{\perp}$) are then combined (Equation 5.1) to yield the induced orientational anisotropy function, *r*(t) (Figure 5.5b):

$$r(t) = \frac{I_{\parallel}(t) - I_{\perp}(t)}{I_{\parallel}(t) + 2I_{\perp}(t)} \tag{5.1}$$

For chromophores in an unrestricted environment such as solution, the initial anisotropic orientational distribution can relax to a random orientational distribution following excitation. When the motion of the chromophore is restricted, however, (*e.g.* by attachment to a lipid membrane), the initial photo-selected anisotropic distribution cannot relax to a fully random orientational distribution. For chromophores in a restricted environment, the orientational anisotropy at times long after excitation does not decay to zero. The motion of the chromophore in a constrained environment can be expressed using a hindered rotor model developed by Lipari and Szabo.[30] In this model the orientational anisotropy decays with time as the chromophore orientational distribution re-randomizes to the extent possible (Equation 5.2):

$$r(t) = r(\infty) + \left(r(0) - r(\infty)\right)\exp\left(-t/\tau_{HR}\right) \tag{5.2}$$

$$\sqrt{\frac{r(\infty)}{r(0)}} = 0.5 \times \left(\cos\theta_0(1 + \cos\theta_0)\right) \tag{5.3}$$

$$\tau_{HR} = \frac{7\theta_0^2}{24D_W} \tag{5.4}$$

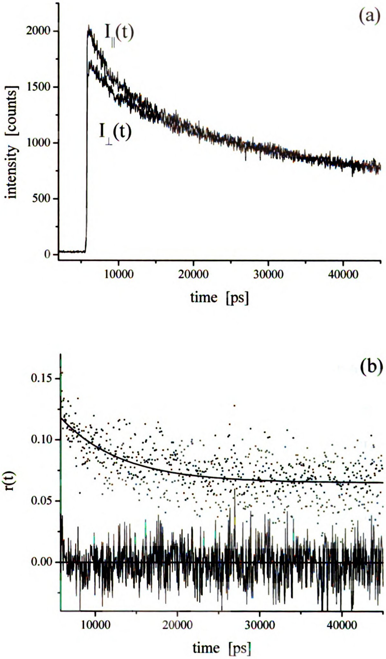

Figure 5.5 (a) Time-resolved emission intensities for polarization parallel ($I_{\|}(t)$) and perpendicular ($I_{\perp}(t)$) to the excitation polarization for pyrene labeled DPPC in DPPC vesicles (0 mol % thio-PEG-lipid) in water. (b) Orientational anisotropy function obtained from data shown in (a). The fit to the data is shown as a solid line and residuals are distributed around zero.

where $r(0)$ and $r(\infty)$ are initial and infinite time anisotropies, respectively. The zero-time anisotropy depends on the angle between the excited and emitting transition dipole moments of the chromophore. The infinite time anisotropy is associated with the degree of motional restriction imposed on the chromophore by its immediate environment (Equation 5.3). The decay time constant τ_{HR} is related to the semi-angle of the cone, θ_0, within which the chromophore is constrained, and is related to the "wobbling" diffusion coefficient, D_W, which describes the motion of the chromophore about its tethering bond (Equation 5.4).

We show in Table 5.1 the quantities $r(0)$, $r(\infty)$, and τ_{HR} obtained for tethered pyrene in lipid aggregates as a function of thio-PEG-DPPE concentration. From the quantities $r(0)$ and $r(\infty)$ we can calculate the angular confinement of the chromophore, θ_0, using Equation 5.3. D_W values, which are indicative of chromophore local freedom, can be extracted from Equation 5.4. The θ_0 values are associated with the organization of the molecules in the lipid bilayer or in the micelle. These values are shown as a function of thio-PEG-DPPE concentration in Figure 5.6, revealing a change in the organization of lipid assembly upon addition of thio-PEG-DPPE. We note from this plot that low concentrations (up to 10 mol %) of thio-PEG-DPPE in the liposomes do not have a large effect on the organization of the molecules in the lipid bilayer. At low concentrations of thio-PEG-DPPE, θ_0 values range from 30° to 38°, indicating a relatively confining environment. As the concentration of thio-PEG-DPPE increases, there is progressively

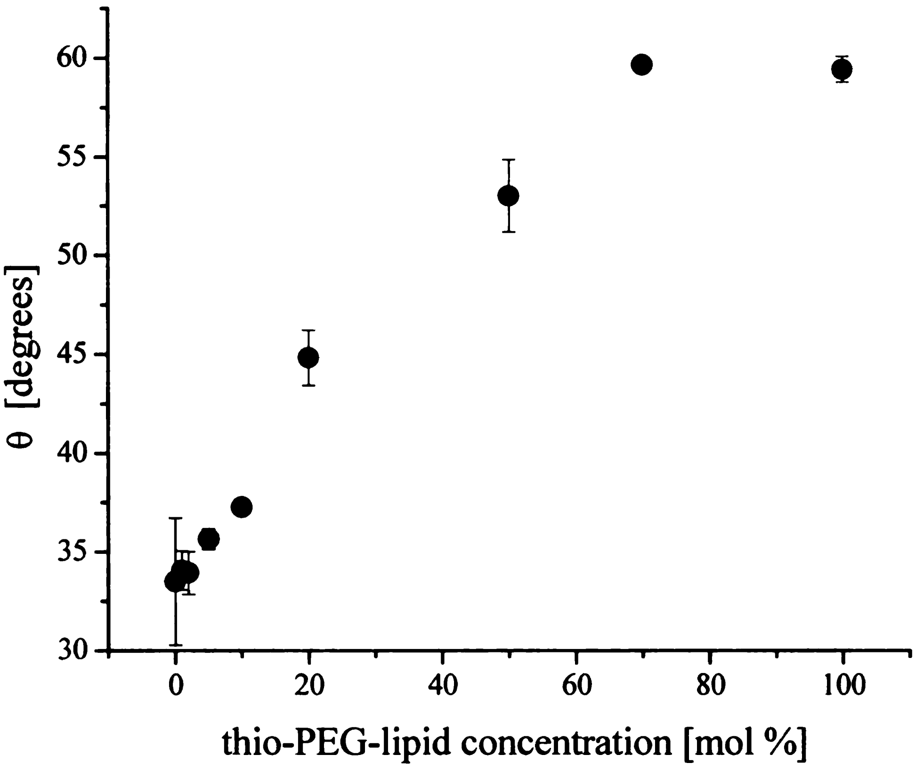

Figure 5.6 Angular confinement of pyrene labeled DPPC represented as θ_0 versus the concentration of thio-PEG-DPPE in the studied systems.

disorder, as shown by the increase in cone angle accessible to tethered pyrene. The maximum level of disorder is reached at thio-PEG-DPPE concentrations as high as 70 mol %, where θ_0 reaches 60° and remains at this level for pure thio-PEG-DPPE micelles. Examining D_W as a function of thio-PEG-DPPE concentration (Figure 5.7) shows that the lamellar phase, present at low thio-PEG-DPPE concentrations, does not produce significant changes in D_W, and the transition from lamellar to micellar phase above 10 mol % thio-PEG-DPPE, where D_W increases with thio-PEG-DPPE concentration. This increase in D_W values with thio-PEG-DPPE concentration corresponds physically to a decrease in the viscosity of the chromophore local environment. For liposomes with thio-PEG-DPPE below 10 mol %, the 15 MHz value of D_W suggests a relatively viscous environment. With increasing thio-PEG-DPPE concentration, the chromophore environment becomes significantly less viscous for tethered pyrene, with D_W increasing to 90 MHz for micelles composed of 100 mol % thio-PEG-lipid; a factor of six change in D_W. The variations in local freedom of motion reflected by changes in D_W correlate well with changes in θ_0, likely corresponding to an organizational change in the headgroup region as a consequence of the presence of the polymer chain terminal groups.

We have also used the anisotropy decay dynamics of perylene to interrogate the lipid acyl chain region(s) of our lipid assemblies. We recover single component fluorescence lifetimes for this chromophore, indicating that perylene resides in a homogenous environment. In contrast to the pyrene fluorescence lifetime data, the perylene fluorescence lifetime changes only slightly (~500 ps) with changes in the thio-PEG-DPPE concentration (Figure 5.8). This finding could be the result of two factors; the comparative insensitivity of the perylene fluorescence quantum yield to the presence

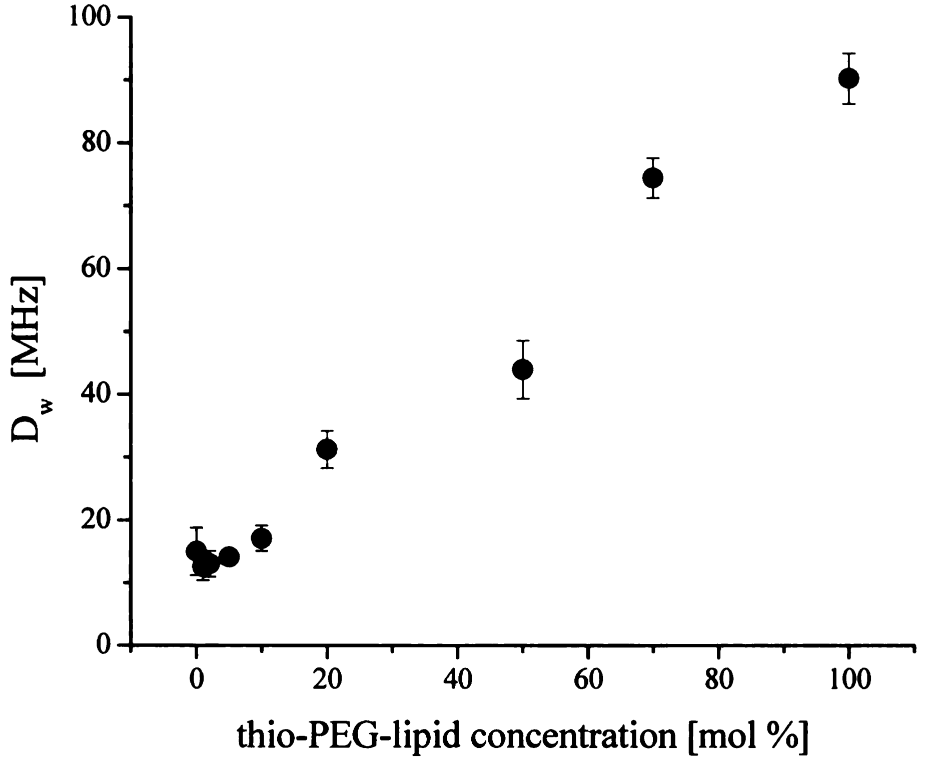

Figure 5.7 “Wobbling” diffusion coefficient (D_W) plotted versus the concentration of thio-PEG-lipid in the lipid aggregates.

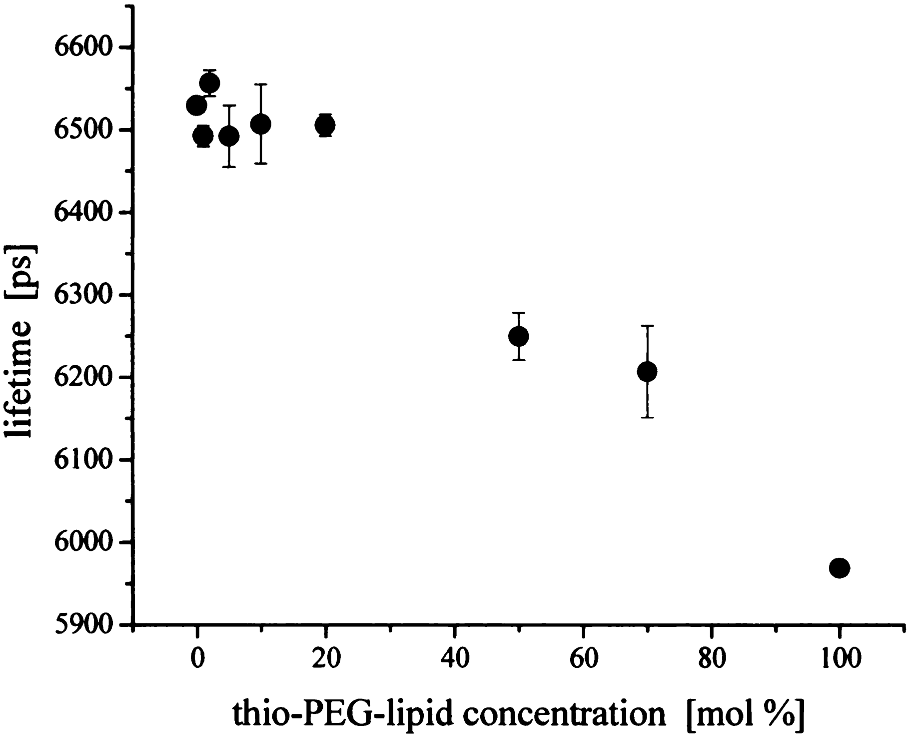

Figure 5.8 Fluorescence lifetime of perylene as a function of thio-PEG-DPPE concentration in the lipid aggregates.

of oxygen, and the likelihood that, regardless of thio-PEG-DPPE concentration, perylene resides in an environment that is comparatively well isolated from the terminal PEG moieties.

The reorientation dynamics of perylene are well understood in a variety of environments.[17-19] Perylene can reorient either as a prolate rotor or an oblate rotor. The rotor shape of this chromophore can be deduced from the functional form of the orientational anisotropy decay. A single exponential anisotropy decay indicates that perylene reorients as a prolate rotor ($D_x > D_y = D_z$) and a double exponential anisotropy decay points to oblate rotor reorientation ($D_z > D_x = D_y$). We observe two-component exponential anisotropy decays for all lipid aggregates reported here (Figure 5.9), indicating perylene reorients as an oblate rotor. For an oblate rotor the induced orientational anisotropy function, *r*(t), is given by:

$$r(t) = 0.1\exp\left(-\left(2D_x + 4D_z\right)t\right) + 0.3\exp\left(-6D_x t\right) \tag{5.5}$$

Where the terms D_i are the Cartesian components of the rotational diffusion constant. Reorientation times obtained from double exponential anisotropy decays are related to Cartesian components of rotational diffusion coefficients:[31]

$$\tau_1 = \frac{1}{6D_x} \tag{5.6}$$

$$\tau_2 = \frac{1}{2D_x + 4D_z} \tag{5.7}$$

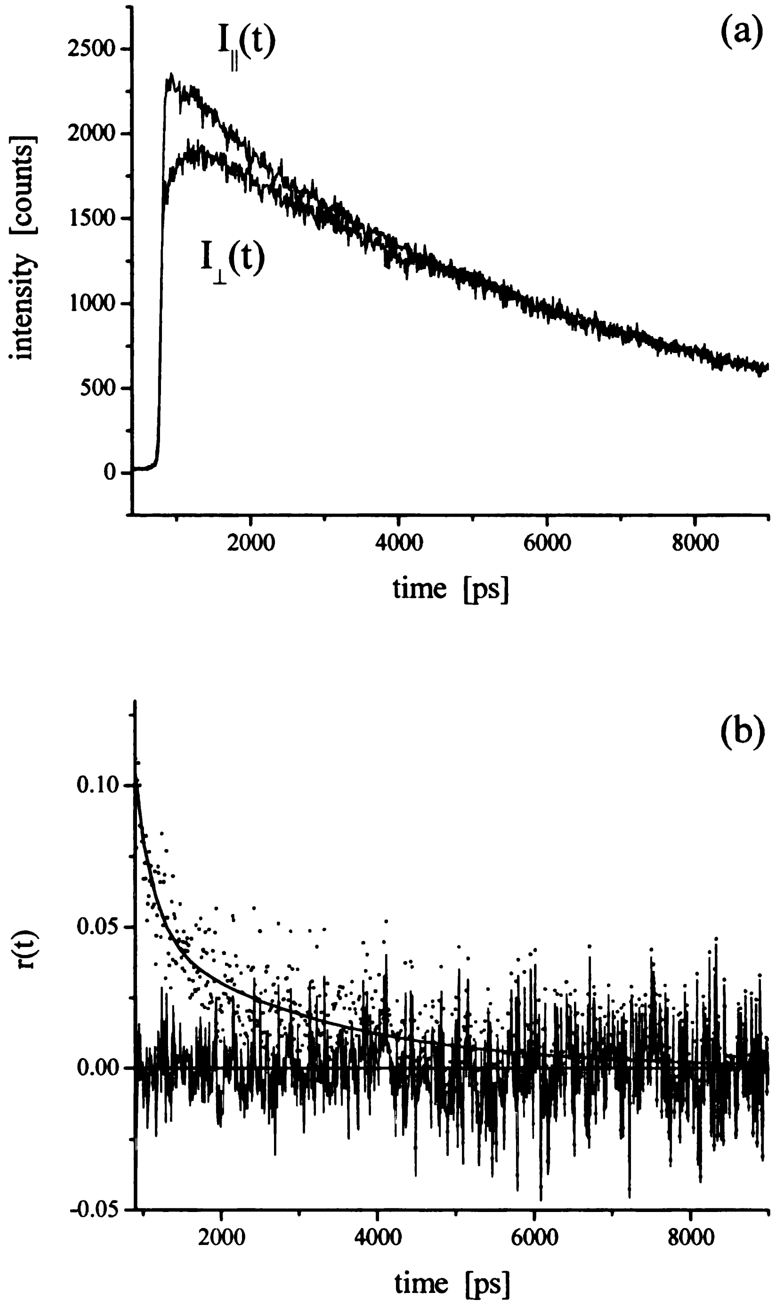

Figure 5.9 (a) Time-resolved emission intensities for polarization parallel ($I_{||}(t)$) and perpendicular ($I_\perp(t)$) to the excitation polarization for perylene in DPPC vesicles (0 mol % thio-PEG-lipid) in water. (b) Orientational anisotropy function obtained from data shown in (a). The fit to the data is shown as a solid line and residuals are distributed around zero.

The shorter time constants recovered from the perylene anisotropy decay data are shown as a function of the concentration of thio-PEG-DPPE (Figure 5.10). These data are largely independent of the amount of polymer-bound lipids present in the lipid assemblies. The time constants are comparatively short (ca. 350 ps) relative to perylene reorientation constants reported for liposomes of similar size but comprised of a shorter lipid (ca. 1000 ps for perylene in DMPC).[19] For DMPC vesicles larger than ca. 1 μm in diameter, perylene exhibited a 400 ps reorientation time. In another report, reorientation time constants on the order of 200 and 270 ps were measured for perylene reorienting in decanoate vesicles and micelles, respectively.[17] Our data indicate that perylene reorientation times on the order of 350 ps for DPPC vesicles and micelles can be attributed to the type of the phospholipid head group and to the length of the lipid acyl chain.

The Cartesian components (D_x, D_z) of the rotational diffusion coefficient D (Figure 5.11a) and their ratios D_z/D_x (Figure 5.11b) (~15) remain largely unchanged with variations in the concentration of thio-PEG-DPPE in the lipid assemblies. The lack of significant change in the diffusion coefficient components suggests a constancy of the environment probed by perylene. Based on calculated Cartesian components of the rotational diffusion coefficient we can estimate the viscosity of the immediate environment of perylene. The most appropriate model for this estimation is the modified Debye-Stokes-Einstein relation:

$$\frac{1}{6D} = \frac{\eta V f}{k_B T S} \tag{5.8}$$

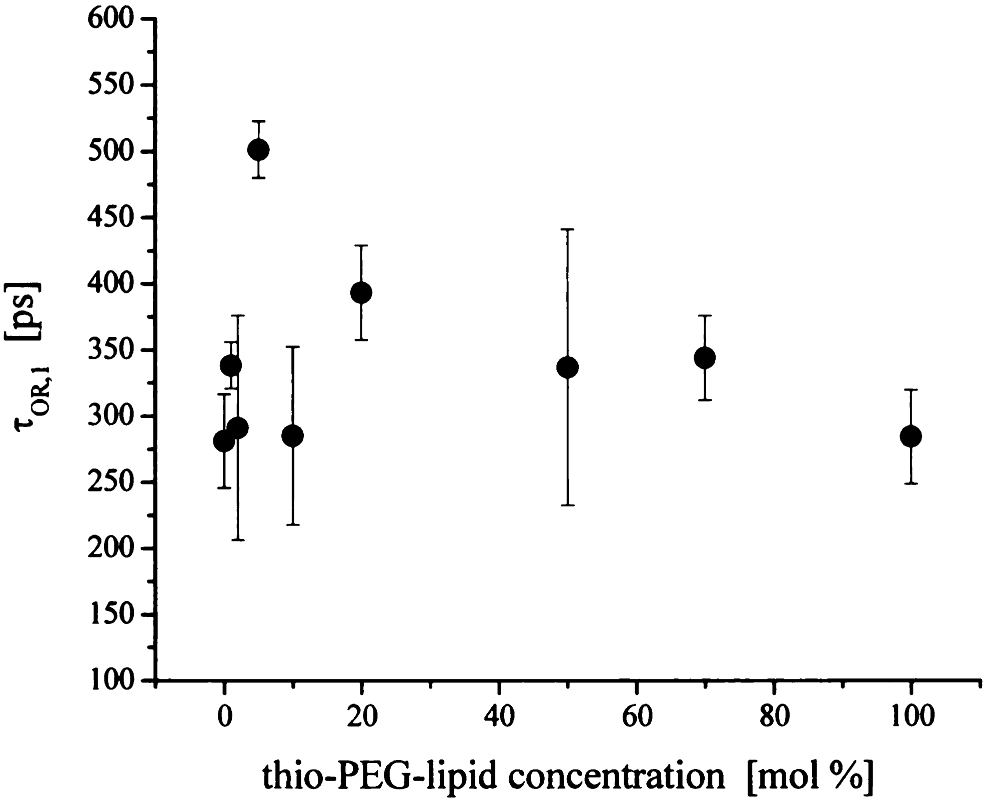

Figure 5.10 Reorientation time constants $\tau_{OR,1}$ obtained for perylene as a function of thio-PEG-DPPE concentration in the lipid aggregates.

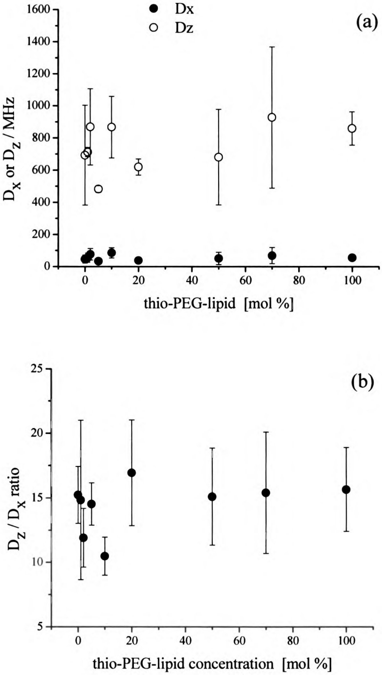

Figure 5.11 Cartesian components of diffusion coefficient (a), D_x and D_z, and their ratio (b), D_z / D_x, obtained for perylene in lipid aggregates plotted as a function of thio-PEG-DPPE concentration in the lipid structures.

where η is the viscosity of the medium, V is the hydrodynamic volume of the chromophore, T is the temperature, k_B is the Boltzmann constant, f is associated with frictional interactions between chromophore and the medium,[32] and S is a factor related to the shape of the chromophore.[33] The average viscosity calculated for all the samples is on the order of 4.5 cP assuming S = 0.7 and $f = 1$,[16] a value consistent with results for this chromophore in large DMPC vesicles.[18,19] We recognize that the model used for the estimation of viscosity is intended for use in bulk solutions, and its utility for fluid lipid systems is questionable. While it may be tempting to compare these data directly to results for perylene in *n*-alkane solvents, we refrain from making this comparison because of the intrinsic confinement of the acyl chains of phospholipids. Such a structural limitation is sufficient to preclude direct comparison to reorientation data for perylene in bulk solvents.

Conclusions

The long-term goal of this work is to construct a robust, biomimetic interface. The potential applications of such an interface are significant both in terms of numbers and specific type. The work we present here deals with changes in the lipid bilayer organization when other lipids that are not structurally identical are present. Owing to the complexity of biological membranes, it is important to evaluate structural and organizational changes in model systems as a function of composition. We have synthesized a lipid conjugated with a hydrophilic polymer in its headgroup. The specific purpose of this structurally modified lipid is to provide anchor points to Au surfaces, thereby producing a chemically robust bilayer. The intended role of the hydrophilic polyethylene glycol polymer is to accommodate the hydrophilic portion of transmembrane protein between the lipid bilayer and the transducer surface.

Deposition of our mixed composition lipid structures was to be accomplished by lipid fusion of mixed lipid vesicles on a gold surface would be the simplest way to build a supported lipid bilayer on transducer surface. The failure to produce surface-attached lipid bilayer structures led to the need to understand the solution phase lipid assemblies that were presented to the interface. TEM images of the liposomes composed of mixed lipids revealed a dependence of the liposome structure on the concentration of modified lipids in the lipid assembly (Figure 5.1). We have interrogated the dynamics of chromophores contained in these lipid assemblies and our findings indicate that, in general, the addition of thio-PEG-DPPE to DPPC lipid assemblies gives rise to changes in organization that are most prominent in the region of the lipid head group and the adjacent PEG-containing region. Reorientation dynamics of perylene show that the organization of the lipid bilayer acyl chain region is affected to a limited extent by changes in the microscopic morphology of the lipid assemblies. Our data point to the importance of lipid assembly morphology in determining the manner in which the assemblies interact with interfaces, and at the same time provide some insight into how changes in molecular scale organization depend on composition for such systems. We anticipate that the results presented in this paper will ultimately allow for the construction of stable, supported planar lipid bilayer structures with adjustable molecular-scale organization and dynamics.

Literature Cited

(1) Hristova, K.; Kenworthy, A.; McIntosh, T. J. *Macromolecules* **1995**, *28*, 7693-9.

(2) Belsito, S.; Bartucci, R.; Montesano, G.; Marsh, D.; Sportelli, L. *Biophysical Journal* **2000**, *78*, 1420-1430.

(3) Kenworthy, A. K.; Simon, S. A.; McIntosh, T. J. *Biophysical Journal* **1995**, *68*, 1903-20.

(4) Leal, C.; Roegnvaldsson, S.; Fossheim, S.; Nilssen, E. A.; Topgaard, D. *Journal of Colloid and Interface Science* **2008**, *325*, 485-493.

(5) Edwards, K.; Johnsson, M.; Karlsson, G.; Silvander, M. *Biophysical Journal* **1997**, *73*, 258-266.

(6) Belsito, S.; Bartucci, R.; Sportelli, L. *Biophysical Chemistry* **2001**, *93*, 11-22.

(7) Rovira-Bru, M.; Thompson, D. H.; Szleifer, I. *Biophysical Journal* **2002**, *83*, 2419-2439.

(8) Johnsson, M.; Edwards, K. *Biophysical Journal* **2003**, *85*, 3839-3847.

(9) Edwards, K.; Almgren, M.; Bellare, J.; Brown, W. *Langmuir* **1989**, *5*, 473-8.

(10) Silvander, M.; Karlsson, G.; Edwards, K. *Journal of Colloid and Interface Science* **1996**, *179*, 104-13.

(11) Vinson, P. K.; Talmon, Y.; Walter, A. *Biophysical Journal* **1989**, *56*, 669-81.

(12) Walter, A.; Vinson, P. K.; Kaplun, A.; Talmon, Y. *Biophysical Journal* **1991**, *60*, 1315-25.

(13) Edwards, K.; Almgren, M. *Langmuir* **1992**, *8*, 824-32.

(14) Fromherz, P. *Chemical Physics Letters* **1983**, *94*, 259-66.

(15) Lasic, D. D. *Biochimica et Biophysica Acta, Biomembranes* **1982**, *692*, 501-2.

(16) Jiang, Y.; Blanchard, G. J. *Journal of Physical Chemistry* **1994**, *98*, 6436-40.

(17) Stevenson, S. A.; Blanchard, G. J. *Journal of Physical Chemistry B* **2006**, *110*, 13005-13010.

(18) Koan, M. M.; Blanchard, G. J. *Journal of Physical Chemistry B* **2006**, *110*, 16584-16590.

(19) Lapinski, M. M.; Blanchard, G. J. *Chemistry and Physics of Lipids* **2008,** *153,* 130-137.

(20) Karpovich, D. S.; Blanchard, G. J. *Langmuir* **1996,** *12,* 5522-5524.

(21) Dominska, M.; Krysinski, P.; Blanchard, G. J. *Langmuir* **2008,** *24,* 8785-8793.

(22) Mazur, M.; Krysinski, P.; Blanchard, G. J. *Langmuir* **2005,** *21,* 8802-8808.

(23) Krysinski, P.; Zebrowska, A.; Michota, A.; Bukowska, J.; Becucci, L.; Moncelli, M. R. *Langmuir* **2001,** *17,* 3852-3857.

(24) Krysinski, P.; Zebrowska, A.; Palys, B.; Lotowski, Z. *Journal of the Electrochemical Society* **2002,** *149,* E189-E194.

(25) Kalyanasundaram, K.; Thomas, J. K. *Journal of the American Chemical Society* **1977,** *99,* 2039-44.

(26) Dong, D. C.; Winnik, M. A. *Canadian Journal of Chemistry* **1984,** *62,* 2560-5.

(27) Karpovich, D. S.; Blanchard, G. J. *J. Phys. Chem.* **1995,** *99,* 3951-8.

(28) Tulock, J. J.; Blanchard, G. J. *Journal of Physical Chemistry A* **2000,** *104,* 8341-8346.

(29) Ding, L.; Fang, Y.; Blanchard, G. J. *Langmuir* **2007,** *23,* 11042-11050.

(30) Lipari, G.; Szabo, A. *Biophysical journal* **1980,** *30,* 489-506.

(31) Chuang, T. J.; Eisenthal, K. B. *Journal of Chemical Physics* **1972,** *57,* 5094-7.

(32) Hu, C.-M.; Zwanzig, R. *Journal of Chemical Physics* **1974,** *60,* 4354-7.

(33) Perrin, F. *Journal de Physique et le Radium* **1936,** *7,* 1-11.

CHAPTER 6

CONCLUSIONS

The long-term goal of this work is to construct supported lipid bilayers which are capable of accommodating transmembrane proteins and maintaining their biological activity and examine their properties. There are several important parameters that have to be considered when designing such an interface on solid substrates. One of the requirements is that the lipid bilayer must be in a sufficiently fluid state to allow diffusion of the incorporated proteins. Another requirement is that both sides of the lipid membrane must be surrounded by aqueous compartments in order to accommodate hydrophilic portions of the inserted proteins. In our work we have focused on the organization of a bilayer structure absent protein incorporation. An important aspect of the construction and interrogation of the supported biomimetic systems is the incorporation of "reporter" molecules that are capable of probing the local environment of an interface. For information from these reporter molecules to be useful, they must be localized at predetermined locations within the biomimetic structure. One way to accomplish this goal is to tether the probe molecule to the supporting interface.

We have designed a series of self-assembled monolayers (SAMs) containing pyrene covalently bound to the gold, indium-doped tin oxide (ITO) or silica surfaces. Electrochemical investigations show that tethered pyrene itself does not form well organized and insulating SAMs, but rather enjoys significant molecular freedom. The evaluation of electron transfer kinetics in Chapter 2 reveals that the monolayers on gold are better organized than those formed on ITO. The charge transfer kinetics particularly on gold also show that codeposition of tethered pyrene with aliphatic adsorbates improves the organization of SAM by imposing some structural confinement on tethered pyrene. However, even the two component SAMs are not sufficiently compact to mediate the energetics of pyrene redox chemistry. Time-resolved fluorescence anisotropy decay data on the structural confinement, organization, and motional freedom of tethered pyrene within these monolayers are presented in Chapter 3. These data show that chromophores bound very close to the substrate surface are characterized by molecular motion that is constrained to only a limited extent even when aliphatic coadsorbates are present. We attribute this effect to a relatively small number of attractive interactions with neighboring molecules. The chromophores tethered further away from the substrate exhibit more hindered motion, consistent with influence from neighbor-neighbor intramolecular interactions.

We have also used Langmuir-Blodgett (LB) and Langmuir-Schaefer (LS) methods to construct planar lipid membranes on gold and silica substrates. Our model system in Chapter 4 was a bilayer comprised of a bottom leaflet of fatty acids and fatty acid analogues and a top leaflet of phospholipids. Some of the fatty acid analogues used in this work were labeled with pyrene. We employed this tethered chromophore to probe the organization and electron transfer characteristics of the monolayer and bilayer. Electrochemical data identify a relatively slow and almost distance-independent electron transfer from tethered pyrene to the electrode surface. These data point to relatively well organized monolayers and bilayers. Time-resolved fluorescence anisotropy decay measurements indicate that the tethered pyrene resides in a moderately constrained environment, as detected by the small volume accessible for the chromophore to rotate within, and the slow rate of motion. These experimental results suggest subtle differences between monolayer and bilayer organization that are expected based on capping properties of the lipid overlayer.

To provide a hydrophilic compartment for accommodation of the hydrophilic portion of a transmembrane protein, we have synthesized a lipid conjugated with a short thiol-terminated polyethylene glycol (PEG) chain in its headgroup. The specific purpose of this thiolated lipid was to provide anchor points to Au surfaces, thereby producing a chemically robust bilayer. Deposition of a lipid bilayer with a hydrophilic cushion between the bilayer and solid substrate was to be accomplished by vesicle fusion on a gold surface. However, the failure to produce surface-attached lipid bilayer structures led to the need to understand the solution phase lipid assemblies that were presented to the interface. Chapter 5 deals with a dependence of the liposome structure on the concentration of modified lipids in the lipid assembly. We have interrogated the dynamics of chromophores contained in these lipid assemblies and our findings indicate that, in general, the addition of thio-PEG-lipid to phospholipid assemblies gives rise to changes in organization that are most prominent in the region of the lipid head group and the adjacent PEG-containing region. The organization of the lipid bilayer acyl chain region has been shown to be affected to a limited extent by changes in the microscopic morphology of the lipid assemblies.

In general, the information we gained from this work provides a foundation for investigating supported lipid bilayer structures. Solution phase lipid aggregate data point to the importance of lipid assembly morphology in determining the manner in which the assemblies interact with solid substrates, and at the same time provide some insight into how changes in molecular scale organization depend on composition for such systems. We anticipate that the results we have presented here will ultimately allow for the construction of stable, supported planar lipid bilayer structures with adjustable molecular-scale organization and dynamics.